

POLITECNICO DI TORINO

**Corso di Laurea Magistrale
in Mechatronic Engineering**

Tesi di Laurea Magistrale

**Realisation
of a plane pendulum test rig**



Relatori

Prof. Alessandro Vigliani

Prof. Elvio Bonisoli

Ing. Simone Venturini

Candidato

Aiken Johnson Escudero

A.A.2020/21

Index

Index.....	2
Abstract.....	4
1. Introduction.....	5
1.1 Motivation.....	5
1.2 Objectives.....	5
2.3 Conclusions.....	6
2. System modifications.....	7
2.1 Correction of pulley eccentricity.....	7
2.2 Increasing torsional stiffness of travelling rail.....	8
2.3 Electrical housing box and wiring.....	9
2.4 Pendulum design and fabrication.....	12
2.5 Conclusions.....	17
3. Position and speed estimation of incremental encoder.....	18
3.1 Function of incremental encoder.....	18
3.2 Frequency-based speed estimation.....	19
3.3 Period-based estimation.....	20
3.4 Estimation by moving average.....	21
3.5 Relative errors of methods.....	22
3.6 Real-time implementation.....	23
3.7 Conclusions.....	25
4. System equations and state space.....	26
4.1 Pendulum and carriage.....	26
4.2 BLDC motor.....	30
4.3 State space equations.....	32
4.4 Motor parameter estimation.....	37
4.5 Pendulum damping estimation.....	48
4.6 Model validation.....	50
4.7 Conclusions.....	59
5. Controller.....	60
5.1 LQR controller.....	60
5.2 Controller tuning and performance.....	60
5.3 Conclusions.....	66
6. Real-time control.....	68
6.1 Systems hierarchy map.....	68
6.2 Kinematic relations and position reconstruction.....	69
6.3 Zeroing.....	69
6.4 Soft limits and saturation.....	71
6.5 VeriStand® environment and user GUI.....	73
6.6 Conclusions.....	75
7. Conclusions.....	76
Appendix A - Drawings.....	77
A.1 – Pulley column stabiliser.....	78
A.2 - Assembly-level for the electrical box.....	79
A.3 - Baseboard for mounting components.....	80
A.4 – Cover for electrical box.....	81
A.5 – Plane pendulum assembly drawing.....	82
A.6 – Pendulum rod drawing.....	83
A.7 – Lead mass drawing.....	84

A.8 – Pendulum axle drawing..... 85

Reference 86

Abstract

This thesis is the realization of a test rig for studying the free and controlled dynamics of a plane pendulum actuated by a two-axis cart. The control targets are regulation of the simple pendulum, stabilisation of the inverse pendulum, and servo behaviour of the cart. System dynamics are modelled through an experimentally verified nonlinear model, linearized to develop an LQR controller. Sensor data is processed into information about the system states and limit definition of the cart position. The controller is implemented through real-time software and a user interface is developed to dictate cart behaviours.

1. Introduction

1.1 Motivation

Control of a plane pendulum is a classic entry into intuitive stable and unstable dynamics of a simple system. Beyond offering a visual and didactic demonstration of stabilisation and the effects of control on frequency and damping, nonlinearity in the pendulum solution emphasizes the costs and benefits of linearization in control strategies. Linearized pendulum models generally offer simpler control laws with large error outside the small-angle region. Complexity of the plane pendulum system can be easily increased by targeting switching between stable and unstable equilibrium through so-called swing-up procedures which must pass through significantly nonlinear regions and angular domain shifts. Further complexity comes from adapting the plane pendulum to a spherical pendulum in three dimensions, prompting decisions about the control approach, such as chosen coordinate system and division of the spherical pendulum into two simultaneous plane pendulum problems. The three-dimensional pendulum in its stable simple configuration or the unstable inverted pendulum have corollaries in real-world systems, especially ones related to balance such as human equilibrium, self-righting vehicles, and ship weight distribution.

For study of the pendulum, a didactic test rig is valuable if it can configure for the plane pendulum and its stable and unstable subsets as well as intermediate maneuverers, and likewise for its spherical counterpart. Previously work has been done to design a two-axis framework capable of hosting a cart-driven planar or spherical pendulum. The planar pendulum has been projected and sized and is now to be realised as an electromechanical control system in real-time.

1.2 Objectives

The object of the thesis is to develop and prove the working real-time control of the rigid plane pendulum in two-axis H-bridge actuation. The pendulum is fixed to a cart which is actuated by a belt transmission system driven by two motors which combine to either two-axis motion or nominally planar behaviour. Realisation of the pendulum test bank reaches four domains: operations on the mechanical and electrical plant, establishing the systems sensors and signal processing, model development and controller design, and real-time digital implementation of the control system and background processes.

In the first step, the transmission system is to be altered to reduce transmission losses. Wiring is required between the sensors and actuators and data acquisition ports. Sensor signals must be filtered and processed to robustly reconstruct the system states and operating limits. A real-time controller should be instituted to command control actions based on the measured states. Limits and safety procedures should operate reliably in the background. Cumulatively the targeted result is proven control of the cart-actuated planar pendulum system.

There are four subdomains to this control:

- regulation of the simple planar pendulum;
- regulation and servo behaviour of the two-axis cart for simple pendulum;
- stabilisation and regulation of the inverted planar pendulum;
- regulation and servo behaviour of the two-axis cart for inverted pendulum.

Optimality is not a stringent requirement; rather than performance-driven control requirements, the didactic rig has loose time-domain specification aimed to demonstrate the dynamic effects of control on the pendulum system. Simplicity of the controller is however prized; a control law which

can be explained without excessive background is didactically preferable to an opaque controller and is generally more realisable without specialised real-time equipment.

2.3 Conclusions

With control of the planar pendulum proven, noted as the first step in complexity of the basic pendulum system, there should clarify a path to increasing the capability of the pendulum test bank. The next planar pendulum step is transition between stable and unstable configurations, whether through a controller or programmed actuation. Further on the horizon can be an augmented configuration for the three dimensional pendulum.

2. System modifications

Mechanical transmission losses are an obstacle to function of the test bank because they limit the control capacity of the motors, particularly critical when the inverse pendulum must be stabilised, and losses due to eccentricities can cause unpredictable, unmodelled dynamics. In the belt-driven H-bridge of the test bank, there are six idlers and belt-cart contact points that cause mechanical losses. The in-line column idlers have eccentric rotations which combine with slackness of the belt to introduce erratic dynamics. A solution is needed to reduce idler eccentricity and diminish the effect of belt elasticity. The H-bridge has another challenge in the stiffness of the moving rail, which is susceptible to twisting out of square; the torsional stiffness of this rail should be increased. In addition, the system sensors and actuators must be wired and the wiring contained in housing. A planar pendulum must also be fabricated that conforms to the mechanical properties projected when sizing the test bank and motors.

2.1 Correction of pulley eccentricity

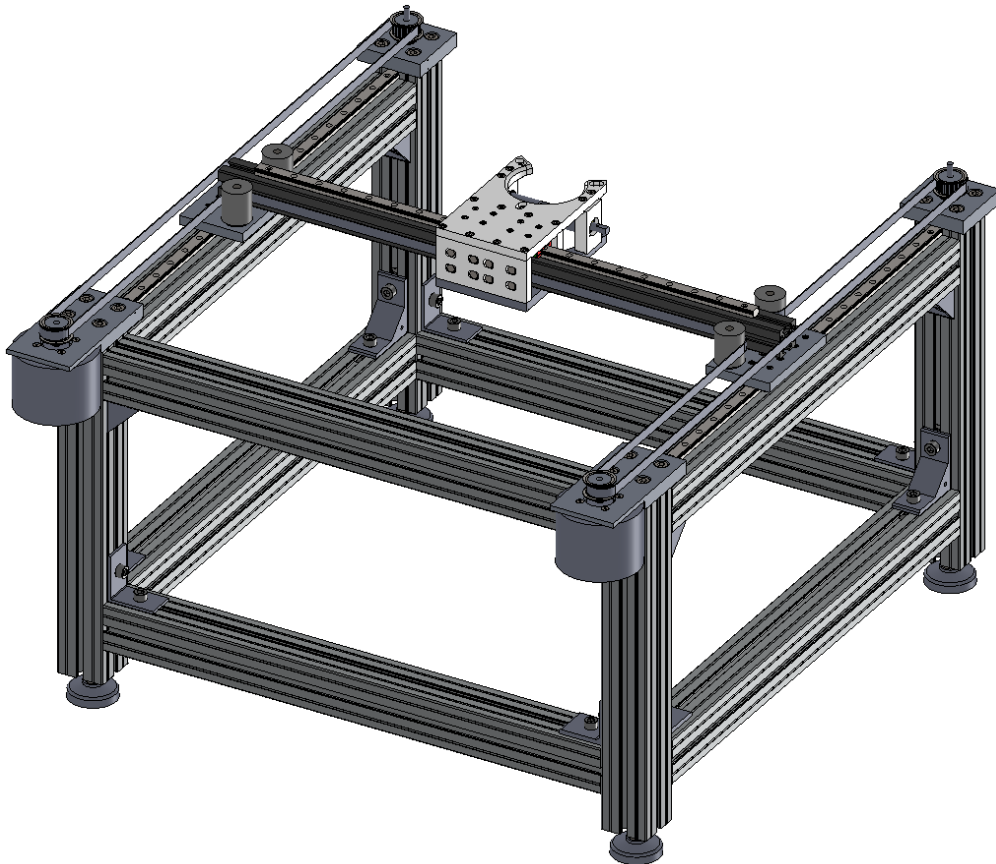


Figure 2.1.1 – Beginning configuration of the test bank.

The pulleys on the towers opposite the motors have eccentricities in rotation from loading by the belt. Being supported only by a bearing from below, the pulleys act as cantilever beams when under tension by the belt (Figure 2.1.2) which causes a rotating off-axis angle of the pulley. The deformation angle is enough to increase attrition in the bearing and produce possible seizing: a combination of belt run irregularity and sticking.

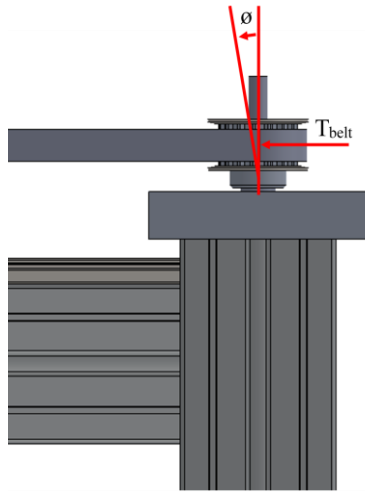


Figure 2.1.2 – Cantilever beam loading of pulley.

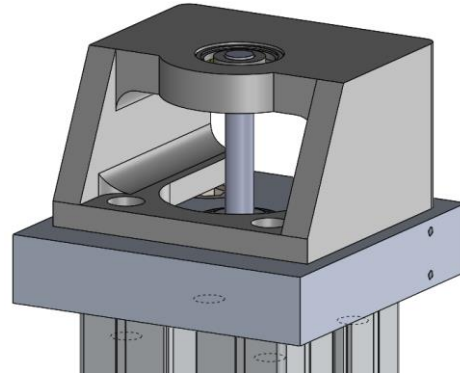


Figure 2.1.3 – Pulley axle support.

To correct the angular deflection, an added frame supports the pulley axle from the top, changing the loading condition. Using a printed support with an inserted bearing (Figure 2.1.3), the axle is kept on-axis and the rotating eccentricity is reduced, though not eliminated. In the figure, the pulley is hidden for clarity.

2.2 Increasing torsional stiffness of travelling rail

The pendulum carriage is mounted to the test bank frame by a rail which has a linear degree of freedom along the X axis. On either end of the rail are two seating plates, fixed to two linear bearings each. Because the rail is mounted to the plate through one fastener on each side, the torsional stiffness of the rail and plate is low. In operation, the rail can twist and is no longer square to the frame, which has three principal consequences. It firstly impedes significantly the motion of the rail along the bearings and causes sticking. It also causes a discrepancy in the cart contact of the limit switches, which are used for zeroing and cart position identification. This limits the operating envelope of the cart and reduces the position estimation of the cart, important states in control.

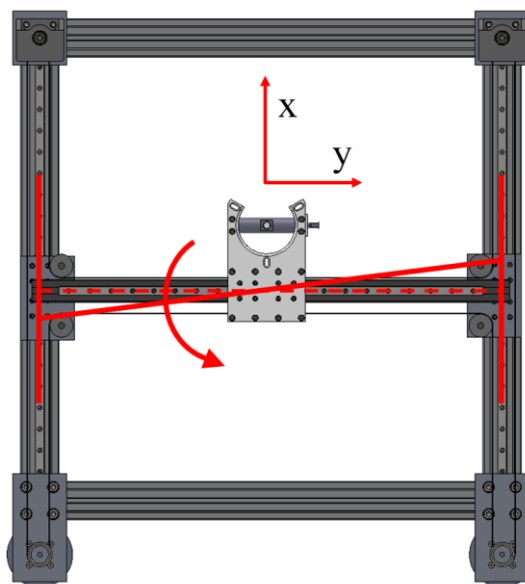


Figure 2.2.1 – Twisting out of square of the travelling rail.

There are several possibilities to remedy this acceptance, but they are constrained by a lack of workable space on the seating plates, and the need to reduce the weight of mobile components. A preferred solution minimizes reworking of the existing parts and respects the constraints. A second fastener is added on the mounting plate to give either end of the rail two-point alignment. The solution is ephemeral because it uses the slotting system of the aluminium frame, which can shift and must be tightened periodically, but the torsional stiffness is greatly improved (Figure 2.2.2).

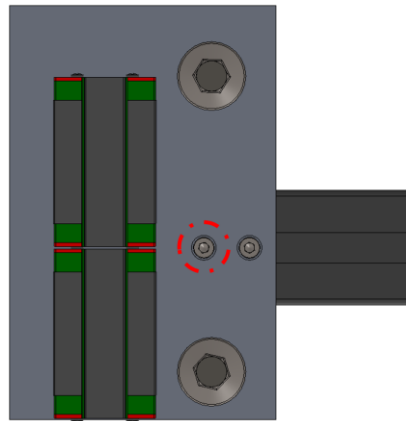


Figure 2.2.2 – Additional fastener on cross-rail base plate.

2.3 Electrical housing box and wiring

The wiring for the pendulum test banks is connects the actuators (motors and drivers) and sensors (incremental encoders and limit switches) to the data acquisition (DAQ) terminal. An electrical box is created for routing the wiring and containing the drivers and DAQ boards. This isolates the components and adds safety features with an emergency shut-off switch and an enable switch for the motors.

In the electrical box (Figure 2.3.1) are housed the motor drivers, the PXI (modular measurement and control platform) connector boards, and the respective wiring connections. The box cover is hinged to facilitate working on the interior. It is mounted directly to the test rig frame by cap screws, which allow changing the height of the box using the T-slotted aluminium framing. The principal consideration is keeping the box out of the path of the pendulum in motion.

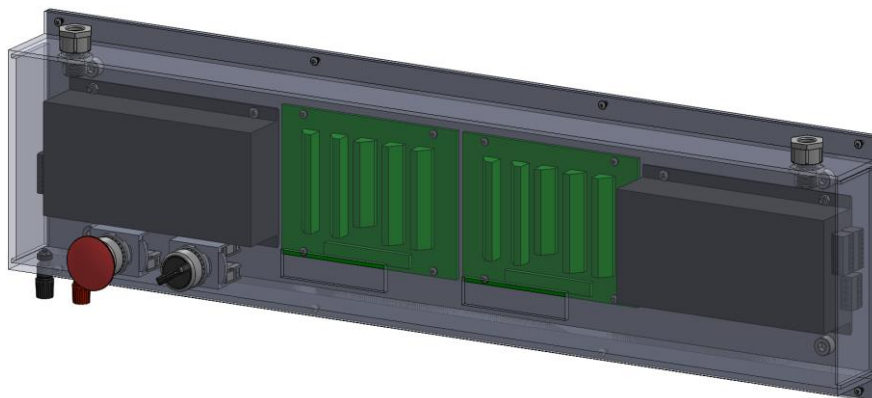


Figure 2.3.1 –Test rig electrical box.

An emergency shut-off switch connects the auxiliary power (24 V, 8 A) to the motor drivers so the motors can be turned off directly at any time. A second switch connects the driver *enable* ports which allows the motors to be disabled while still powered. This is important because the encoders are circuited with the motor drivers; there needs to be a voltage supplied to the drivers even while the motors are not powered so that the position of the motors can still be measured. The electrical box is designed to keep the electrical systems of the motors separate, so the wiring for each motor is confined to half of the box (Figure 2.3.2); then the pendulum position encoder and limit switches are wired where available with the second motor-driver pair.

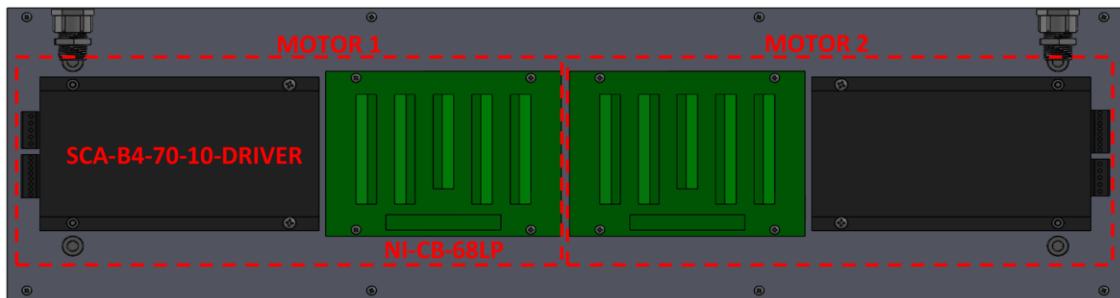


Figure 2.3.2 – Layout of the electrical box.

In Figure 2.3.3 is the system wiring diagram. A primary concern when wiring the motors is to electrically isolate the drivers from each other because when the two motor encoders and drivers have a common ground and connection board, there is potential for signal resonance. In practice, this results in the DAQ reading non-real encoder signals and falsely recreating a change in position.

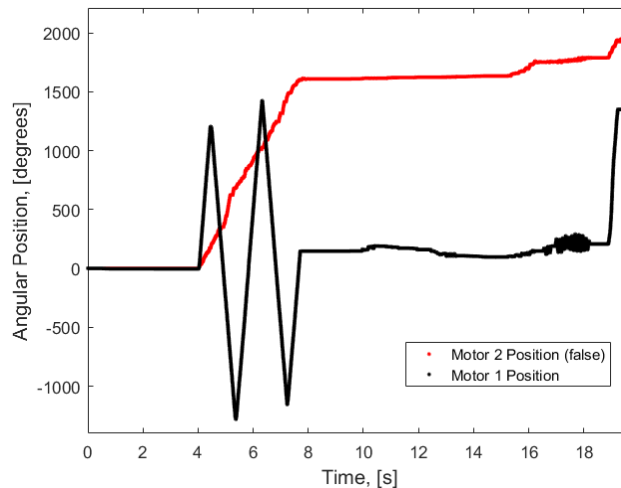


Figure 2.3.4 – Measured motor position runaway from electrical reflection.

This resonance phenomenon is seen in Figure 2.3.4, where the encoder signals are being routed through the same DAQ board. Motor 1 is performing a manoeuvre and motor 2 is actually stationary. However, the encoder signals from motor 1 resonate and appear in the encoder wires for motor 2, showing unpredictable and large variations in position which do not represent the actual motor behaviour. The inciting activity for the erroneous behaviour is clearly encoder signal activity of motor 1. This is likely due to compromised isolation in either the DAQ board or the motor drivers. In order to prevent this behaviour, the motor, encoder, and driver set for motors 1 and 2 are kept on separate DAQ boards and sent to different PXI ports.

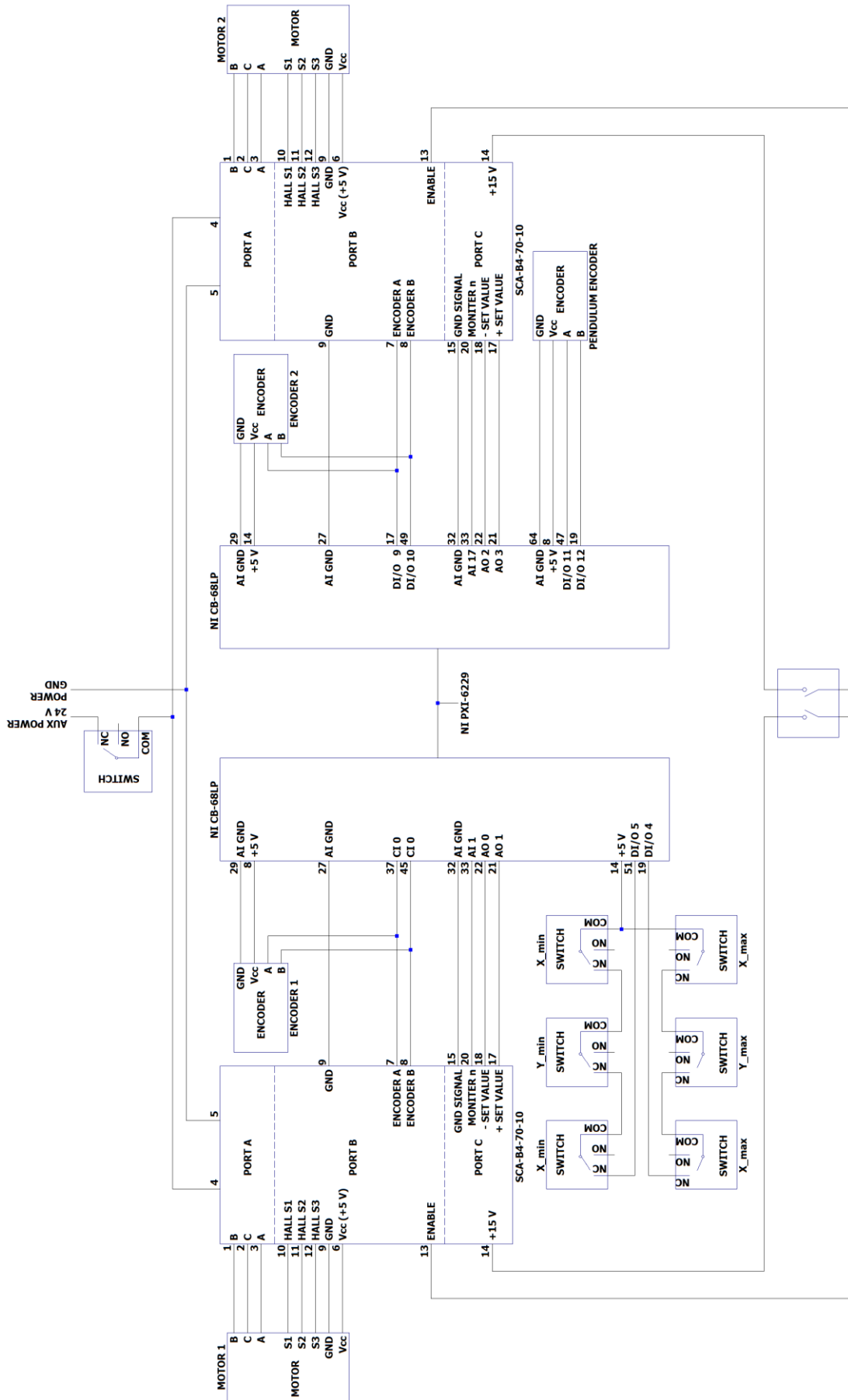


Figure 2.3.4 – Wiring diagram of pendulum test bank system.

Each motor, encoder, and driver set is paired with one of the two ports on the NI PXI-6229 DAQ, due also to the limited analogue output pins which are needed in driving the motors. The encoder signal outputs A and B (see chapter 3) are routed through pins on the DAQ specific to counters such as the quadrature signals from the incremental encoders.

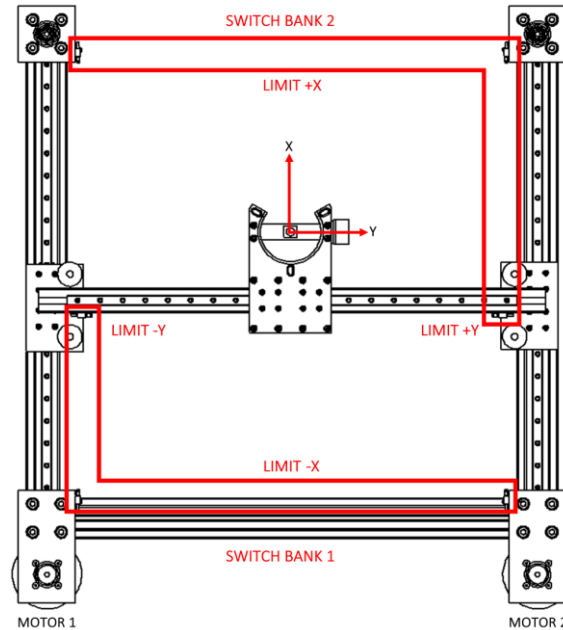


Figure 2.3.5 – Separation of limit switch circuits.

Lastly, limit switches for locating and centring the pendulum carriage are organised in two circuits to use fewer digital pins on the DAQ. If one switch in a bank is triggered, the signal for that respective circuit is broken. Each bank represents opposite limits of the XY plane that the carriage moves in: X_{\min} and Y_{\min} against X_{\max} and Y_{\max} . This division reduces ambiguity and allows for a simple diagonal carriage movement to unblock a triggered switch when overstepping limit bounds (see chapter 6).

2.4 Pendulum design and fabrication

A planar pendulum is constructed to adhere to the properties projected by the thesis work [1][2], listed in Table 2.4.1. It is based on a threaded PVC rod, added lead mass, and stainless-steel fasteners. The pendulum axle, which had been previously machined in stainless steel, has been modified to a printed plastic version of less mass in order to meet the design targets. The pendulum is designed to provide the mass and length (to centre of mass) characteristics prescribed when sizing the motors. Matching these characteristics is critical because the motors and test bank run length were designed to perform operations on a pendulum of these specifications, and a pendulum of greater mass and inertia would not assure performance.

Table 2.4.1 – Target properties of pendulum.

Characteristic	Property	Value
Pendulum	m_p , mass [g]	74.8
	l_p , distance fulcrum to center of mass [mm]	90.0
	J_p , mass moment of inertia (with axle) [kg m ²]	5.3e-4

The designed pendulum (Figure 2.4.1 and Figure 2.4.2) is comprised of a threaded solid PVC rod fastened by M8x1.25 nuts at either end. The free end of the rod passes through a hole in a lead mass, used to shift the centre of mass of the assembly away from the fulcrum, and a printed PLA axle that connects the pendulum to the carriage and encoder. Part drawings are provided in Appendix A. This leaves the possibility of alternate plane pendulums by replacing the existing rod with one differently configured.

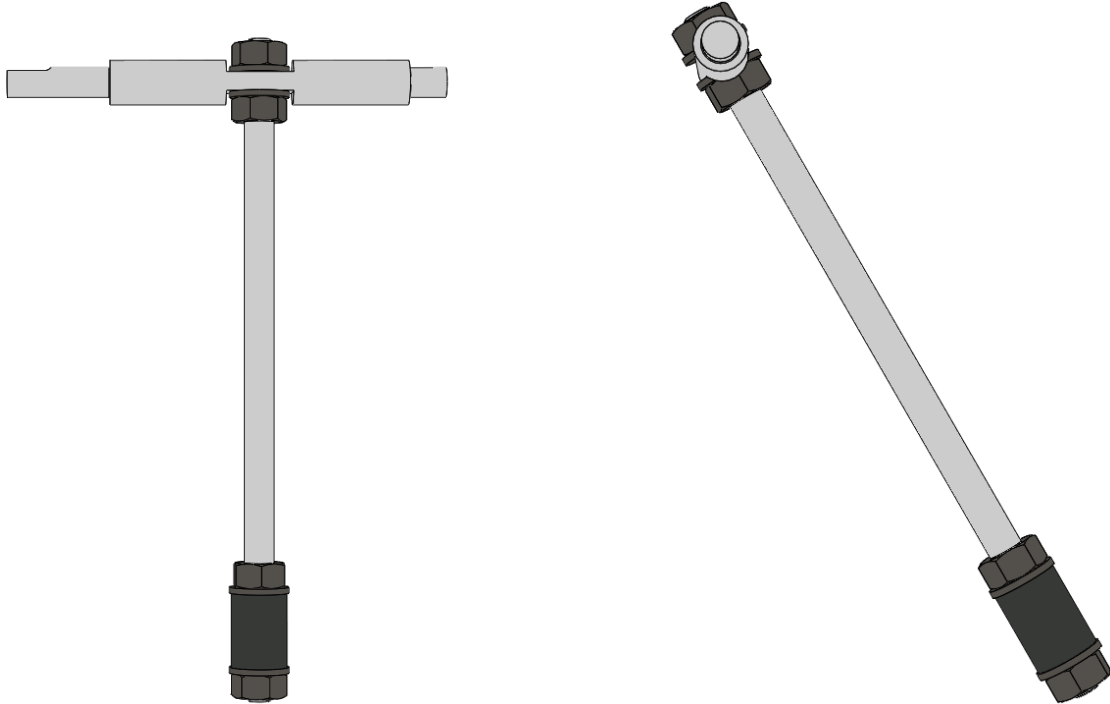


Figure 2.4.1 – Proposed pendulum front view. Figure 2.4.2 – Proposed pendulum lateral view.

The section view in Figure 2.4.3 details the threaded components and how they intersect.



Figure 2.4.3 – Proposed pendulum, section view.

The lengths of the plastic rod and size of the lead mass are designed to specification using a basic algorithm. It takes a set of possible lengths for the plastic rod (the maximum allowable length is 200 mm due to physical constraints of the test bank) and in every case determines the size of the lead mass that reaches the target total mass. Then the composite centre of mass is calculated with eq. (2.1) by assuming the lumped mass of each component, and the chosen solution is that with the distance to the centre of mass closest to the target. Figure 2.4.4 is a schematic of the lumped masses and their distance from the fulcrum (zero point) and the resulting total centre of mass, l_p . The total mass m_p is the sum of all component masses.

$$l_p = \frac{\sum m_i l_i}{m_p} \tag{2.1}$$

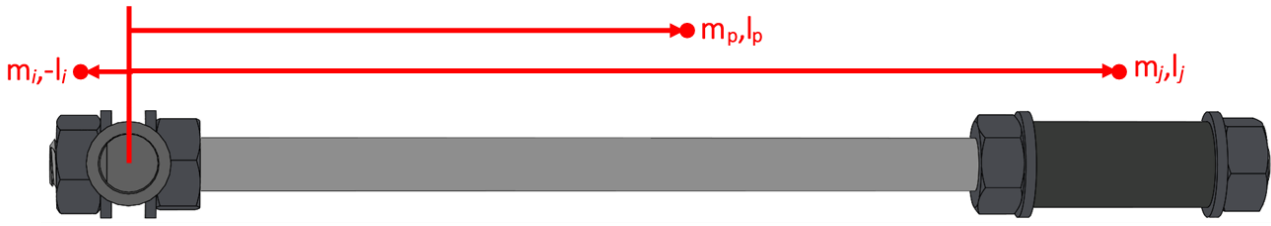


Figure 2.4.4 – Description of pendulum masses and distances from fulcrum.

Figure 2.4.5 presents the results of the algorithm, where the intersection of the target centre of mass distance and the calculated composite distance, highlighted at the blue points gives the solution case for the length of the threaded rod and how much mass should be added. This algorithm can also be adapted to design pendulums of different target properties.

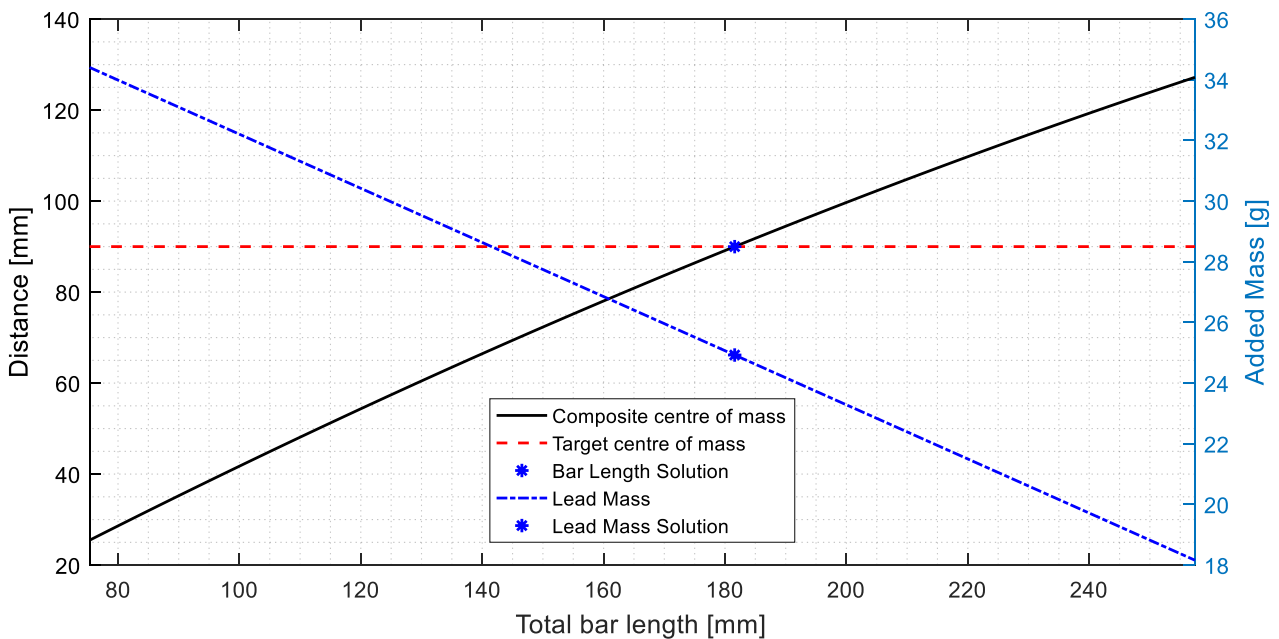


Figure 2.4.5 – Pendulum sizing solution.

Because it is important for the pendulum properties (mass, moment of inertia, centre of mass) to be close to the target, it is valuable to know how they can differ due to variances during fabrication and assembly. There are five cutting operations when fabricating the pendulum, where each cut is given an assumed tolerance of ± 1 mm. The parameter which is most important to not exceed the target is the moment of inertia, because a too-large inertia can challenge the sizing of the motors and the controllability of the pendulum. This is also the parameter which varies the least by the dimensional uncertainty. The pendulum mass and centre of mass distance, which in the system model influence the stiffness of the system and therefore its frequency, are less critical.

Numerical values of the solution are listed for the components in Table 2.4.2. The fabricated components are weighed and compared to the design mass prescribed by the sizing algorithm. The greatest variation in mass comes from the added lead mass, which is modelled as a bored cylinder of constant cross section, while the actual lead blank used to make the piece has some porosity and variation. The total mass is within the bounds predicted by uncertainty analysis, varying from the target by 3.4%. This is an acceptable condition.

Table 2.4.2 – Pendulum components and masses.

Component (Quantity)	Material	Design Mass (g)	Fabricated Mass (g)
Pendulum axle (1)	Printed PLA	10.14	10.12
8 mm threaded rod (1)	PVC	14.48	14.67
Lead mass with through hole (1)	Lead	24.91	23.73
M8x1.25 Hex nut (4)	Stainless steel	4.73	4.73
M8 Washer (4)	Stainless steel	1.63	1.63
Total Mass:		74.97	72.40

The properties of this proposed pendulum relevant to modelling of the pendulum are compared to the target properties given by the design, re-listed in Table 2.4.3. The centre of mass distance, found by suspending the pendulum and finding its vertical intersect, varies from the design value by 1.5%, which is also acceptable. The mass moment of inertia is estimated from the pendulum free response; since all of the pendulum parameters are known except the damping and the inertia, the inertia can be estimated with the natural frequency of the free response (see the damping estimation in chapter 4).

Table 2.4.3 – Properties of proposed pendulum.

Property	Target Value	Design Value	Fabricated Value
m_p , mass [g]	74.80	74.97	72.40
l_p , distance fulcrum to center of mass [mm]	90.00	89.96	91.5
J_p , mass moment of inertia (with axle) [kg m ²]	5.4e-4	3.7e-4	6.65e-5

Because the pendulum is to be controlled as part of a larger system, the flexural natural frequency of the pendulum is estimated to avoid resonance during control. Either end of the pendulum is locally clamped, by the axle or by the added lead mass, which means the primary concern is the exposed shaft between these flexing during rotation at a frequency near resonance. The modes are studied using frequency analysis in SolidWorks[®]. For use in the study, the pendulum is simplified (Figure 2.4.6) by removing the threads in the model and simplifying contacts and meshing. This is an acceptable modification because the threaded contacts occur at the local clamping points where little flexing take place.

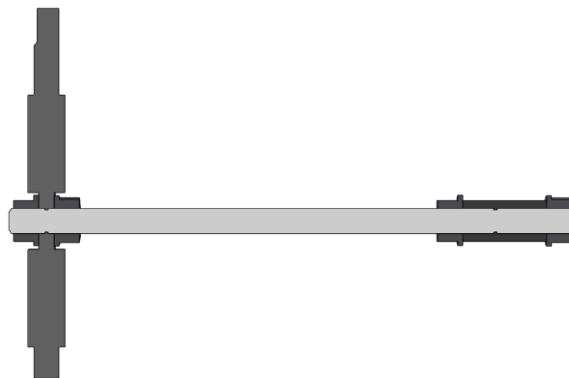


Figure 2.4.6 – Simplified pendulum, section view.

On the model are applied the constraints by the contact of the rolling bearings, and a frequency study is performed on the free, unforced system. The results for the first in-plane flexural mode with

magnified deflection are shown in Figure 2.4.7 and Figure 2.4.8, with red indicating the area of greatest deflection, blue being the least.

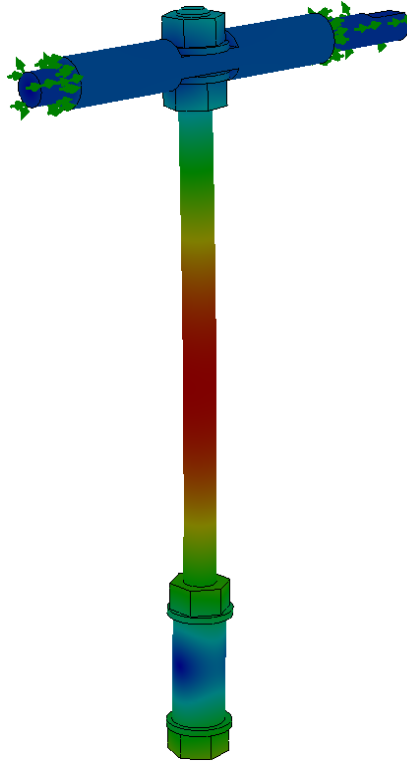


Figure 2.4.7 – Pendulum frequency study, isometric view.



Figure 2.4.8 – Pendulum frequency study, side view.

The results support the intuition that the flexion occurs along the free shaft between the ends. Because the shaft is rigid PVC, the concern is that it could have a flexural mode at a low frequency that might occur in the controlled system. The first frequencies studied are listed in Table 2.4.4.

Table 2.4.4 – First frequencies of the studied pendulum.

	Description	Frequency (rad/s)	Frequency (Hz)
Mode	Rotation about axle, 1 st	6.14	0.98
	Transverse flexural, 1 st	99.48	15.83
	In-plane flexural, 1 st	917.5	146.0

The frequency of rotation about the axle is related to the period of the free pendulum, which is less relevant to the controlled system. The first transverse flexural mode is the flexion transverse to the plane of rotation; this is not a greatly significant in the plane pendulum case because it assumes minimal motion out of plane. As such the important frequency is the in-plane flexural mode, where the first modal frequency is at 917.5 rad/s. This is outside of any control frequency that the system

is likely to operate at, but it is regardless made an objective to avoid designing a control system where a frequency of the pendulum angle is near this natural frequency.

2.5 Conclusions

Lastly, the belt is tightened by a toothed plate in the cart to reduce slack. With the mechanical changes, the passage of the belt becomes much smoother and less disruptive. Reducing these resistances and losses are paramount because the control of the carriage (and therefore the pendulum) depends on a defined, known moment seen by the motors and a consistent delivery of motion. Even with the improvements, the transmission is still affected by losses, particularly with Y-axis motion, with augmented resistive couples caused by eccentricities, sticking of the bearings, and accumulation of attrition in the idlers. These inclusions are difficult to model and consequently reduce the accuracy and capacity of the control action. Similarly, if the belt is slack or it runs inconsistently, the delivery of the control action is not predictable or consistent with the calculated control action. Cumulative erratic behaviours can cause cumulative error estimation with the sensors, eventually leading to misplacement of the cart or pendulum. Higher losses for motion in the Y-axis become a design obstacle for sensing and control because of the encoder type. After these modifications and with the installation of wiring, limit switches, the electrical box, and the pendulum, the updated test bank is given in Figure 2.5.1.

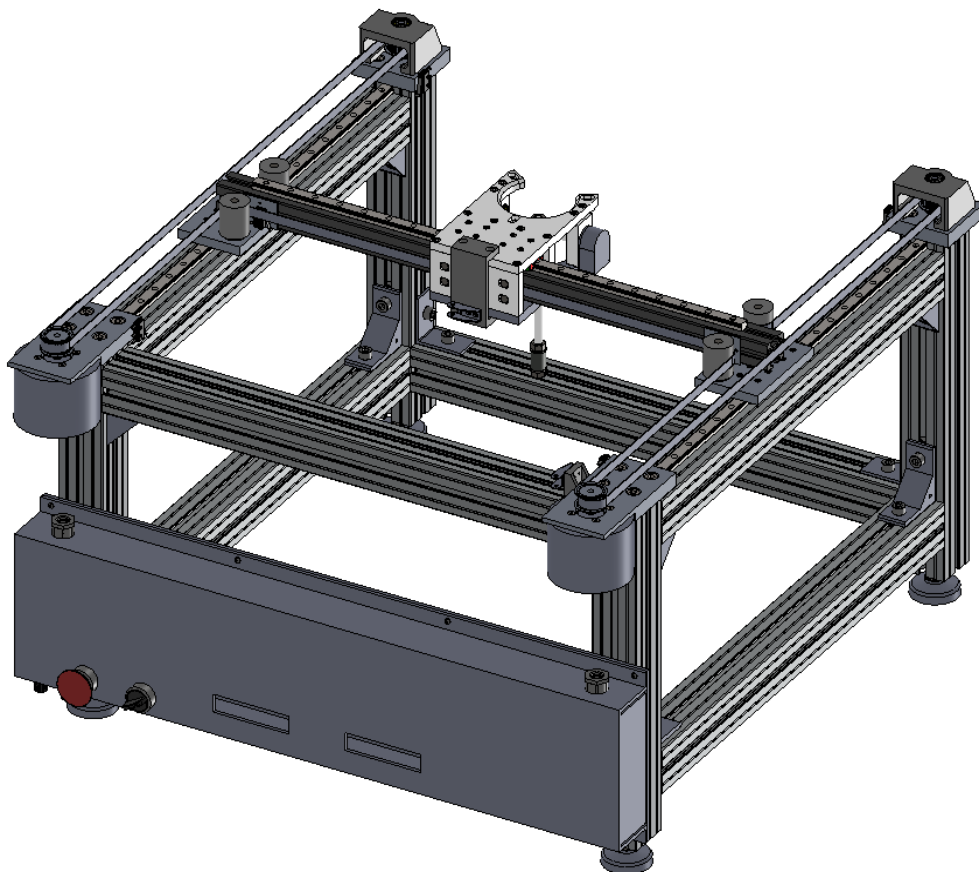


Figure 2.5.1 – Updated pendulum test bank.

3. Position and speed estimation of incremental encoder

Primary signal sensing in the pendulum test bank is performed with HEDL-5640-A13 incremental encoders with a maximum speed of 30000 rpm. Reconstructing angular position with these encoders is the primary sensing of the system because it enables the estimation of motor speed and cart position (and therefore the linear speed and position of the cart); the same encoder is used to reconstruct angular position and speed of the pendulum. There is a key accuracy issue with the estimation of angular speed from the encoder signals which makes achieving a robust speed estimator essential for the correct function of the system.

3.1 Function of incremental encoder

The incremental encoder used operates on two concentric coded disks and an LED which shines through them (Figure 3.1.1). The disks are codewheels that produce a digital I/O cycle by obscuring or passing the LED. In one full rotation of the encoder, the HEDL-5640-A13 has 500 digital I/O cycles. The two codewheels are offset so that their output signals (signals A and B) are in quadrature, at a difference of 90 electrical degrees (Figure 3.1.2) [3].

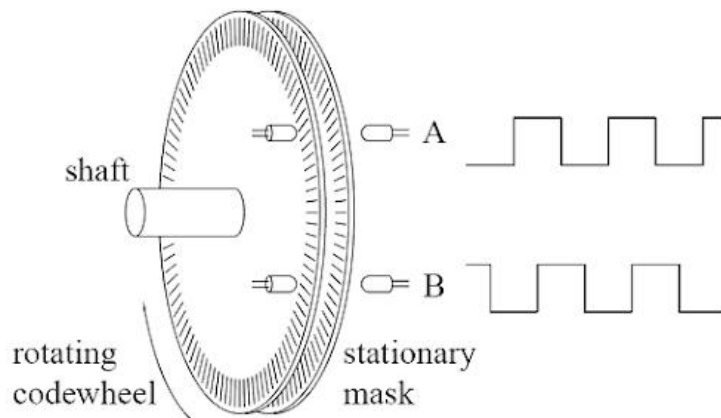


Figure 3.1.1 – Incremental encoder signal production.

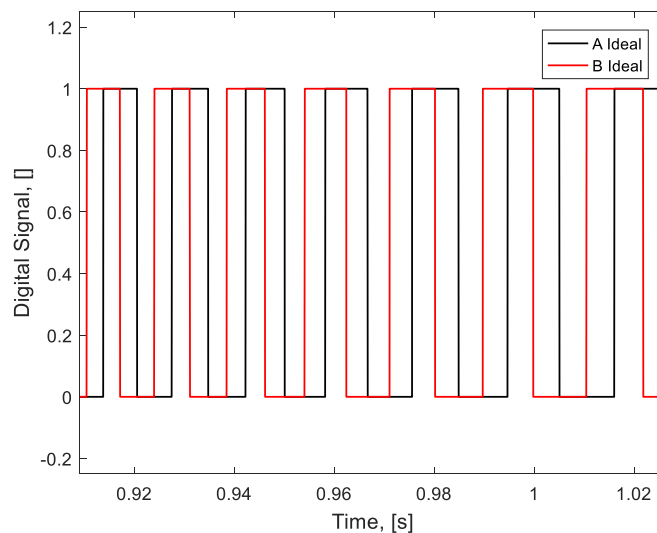


Figure 3.1.2 – Quadrature of signals A and B.

From the A and B signals and their offset, a four-phase incremental change in angular position of the encoder shaft can be determined, as can the direction of rotation from the order of the phases. When sampling the A and B signals, there is a pulse width error of ± 5 electrical degrees inherent to the HEDL-5640-A13 encoder. The encoders are sampled in digital time, which leads to a discrete time, discrete amplitude signal. This error couple affects the encoder quadrature, but more importantly the timing of the signals contains errors, which alter their frequency [4]. Figure 3.1.3 shows a typical pulse width error of the encoder signal (A only) when compared to the ideal. These errors are compounded because the position reconstruction compares two such signals, A and B. In practice, this large electrical window is robust and the position estimation is reliable, requiring no further filtering, but the variation in frequency has a large impact on the speed estimation. Importantly these variations are non-periodic and sample time dependent, which poses an obstacle to filtering.

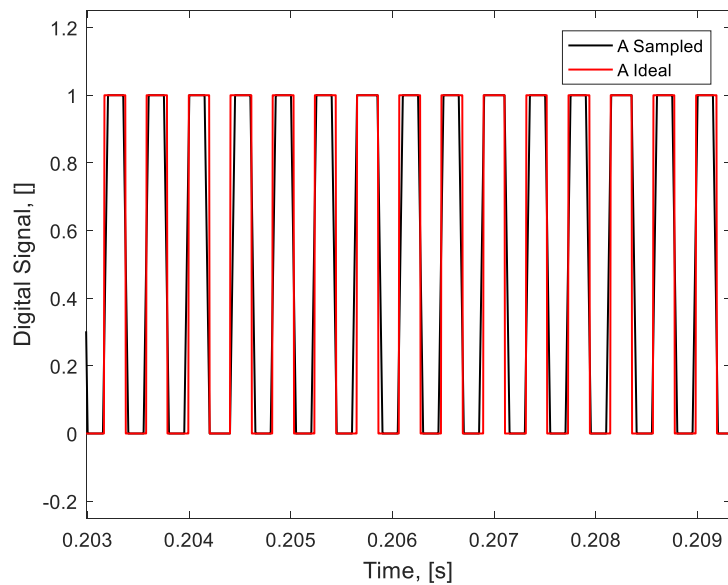


Figure 3.1.3 – Pulse-width error in sampled encoder signal A.

3.2 Frequency-based speed estimation

The basic speed estimation from the incremental encoder is a frequency-based method, the simple digital derivative. For every incremental change in encoder position (denoted as a *pulse*), the difference in position from the prior impulse is divided by the change in time between the two (eq. (3.1)). Because of quantization error inherent to the discrete-amplitude, discrete-time position data, the resulting speed estimation has significant error at higher speeds owing to frequency syncing error between the sampling and encoder angular speed. This estimation is shown with an example angular speed profile (Figure 3.2.1 and Figure 3.2.2) consistent with the frequency and magnitude of projected control actions applied with the pendulum control – that is, simulating the kind of speed profiles that will be seen in the test bank.

$$\frac{d\theta}{dt} = \frac{\theta_2 - \theta_1}{t_2 - t_1} \quad (3.1)$$

The operating range of angular speeds is 0 to 500 rpm, which is the maximum projected motor angular speed projected for control action of the test rig. The sampling of the encoder is taken as 20 kHz, which matches the projected acquisition rate of the DAQ used with the test rig. The period-based speed estimate is compared in Figure 3.3.3.

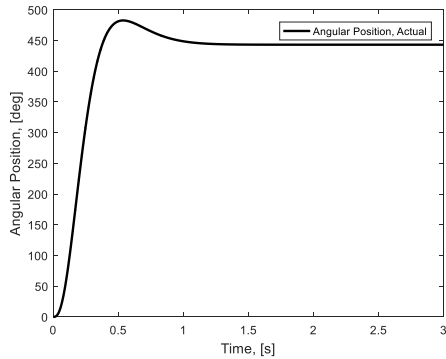


Figure 3.2.1 – Sampled position profile.

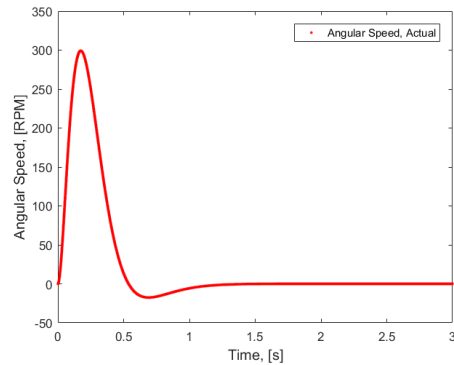


Figure 3.2.2 – Actual speed profile.

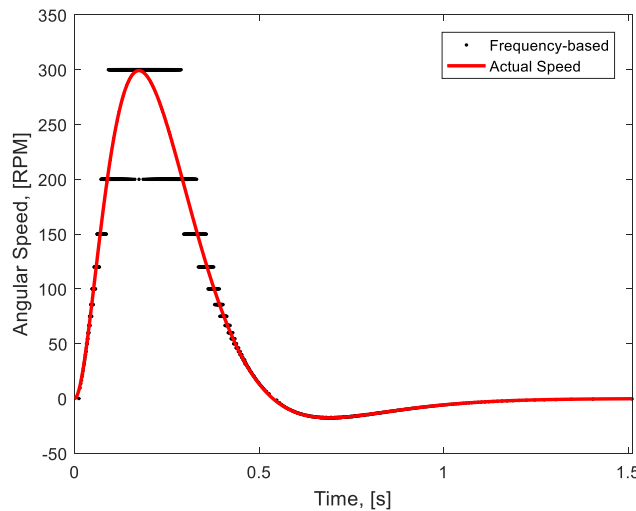


Figure 3.2.3 – Frequency-based speed estimation.

At higher angular speeds, the frequency-based estimation is incapable of tracking the actual speed with any resolution. The effect of a discrete-time and magnitude signal is clear in the digitization of speed values. Tracking at low speeds is better. This is because the quantization error appears most significantly in time and is inversely proportional to the speed. For high angular speeds and short differential time, the error is magnified when inverting the time difference; at lower speeds with longer time periods, the error has less impact.

3.3 Period-based estimation

A method is needed to capture the behaviour at higher angular speeds. A counterpart method to frequency-based estimation is period-based estimation, which sets a defined time window and counts the number of *pulses* in that window to again compute the change in position over change in time [2]. This method, shown in eq. (3.2), is modified slightly to be more responsive so that a set number of *pulses* are counted, and the difference in time is between the first and last *pulse* counted.

$$\frac{d\theta}{dt} = \frac{\theta_i - \theta_{i-110}}{t_i - t_{i-110}} \quad (3.2)$$

Figure 3.3.1 gives the tracking for a speed estimation where the window is 110 *pulses*.

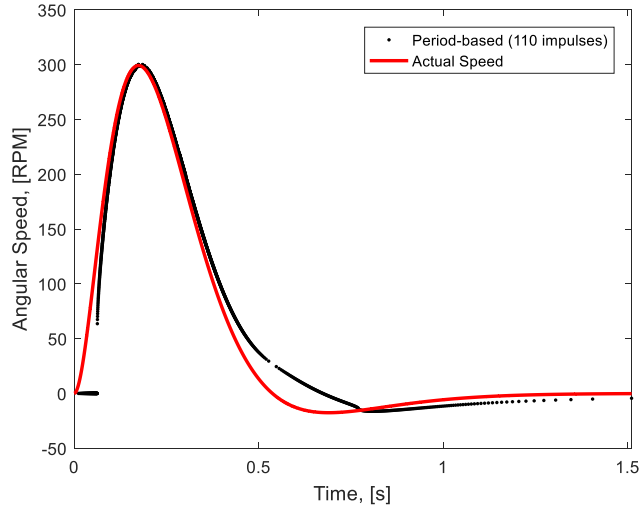


Figure 3.3.1 – Period-based speed estimation (memory of last 110 *pulses*).

The improvement at higher angular speeds can be seen, with the understanding that increasing the memory of *pulses* moderately increases tracking at higher speeds. However, there are two anomalies at lower speeds. This first is an error when the angular speed changes sign due to the memory lagging the change from positive-to-negative speed (or vice versa). Second, there is a drift at the beginning of acquisition while there are less than 110 *pulses* of data; the method cannot calculate properly in this region.

3.4 Estimation by moving average

To capture behaviour at both higher and lower angular speeds, both period-based and frequency-based estimation are used in combination with a selection logic [5]: frequency-based estimation at low speeds and period-based at high. Beyond that basic switch, the memory of previous impulses makes use of variable window lengths (set by k in eq. (3.3)) at different speeds so to better track each speed region, resulting in a moving average with a floating window.

$$\frac{d\theta}{dt} = \frac{\theta_i - \theta_{i-k}}{t_i - t_{i-k}} \quad (3.3)$$

If the minimum window is 2 *pulses* (effectively period-based estimation) and the maximum window used here is 120 *pulses*, it is noted that for medium-to-higher angular speeds (ex., the range of 15 to 500 rpm), not all speeds track better with the full window of 120 *pulses*. It is desirable to reduce the window for mid-range angular speeds, depending on the magnitude of the speed (frequency of the encoder signal). For this, a lookup table is used, dividing the operating range (0 to 500 rpm) into sections, each with a target window of between 2 and 120 *pulses*. Based on the last estimated speed, the table selects the appropriate length of the buffer to use.

In the lookup table, these sections and their corresponding buffer length are calibrated by estimating the speed with various *pulse* windows and finding the speed regions of minimum error. For

instance, the speed is estimated using a window of 40 *pulses*, and the speeds at which the estimate error is minimum (nominally less than 5 %) are the corresponding speeds in the lookup table. Lastly, to correct the drift observed at the beginning of acquisition (since the floating window could request a quantity of *pulses* which have not yet been acquired), a condition defaults to use the maximum memory available when the requested window is larger than what is available.

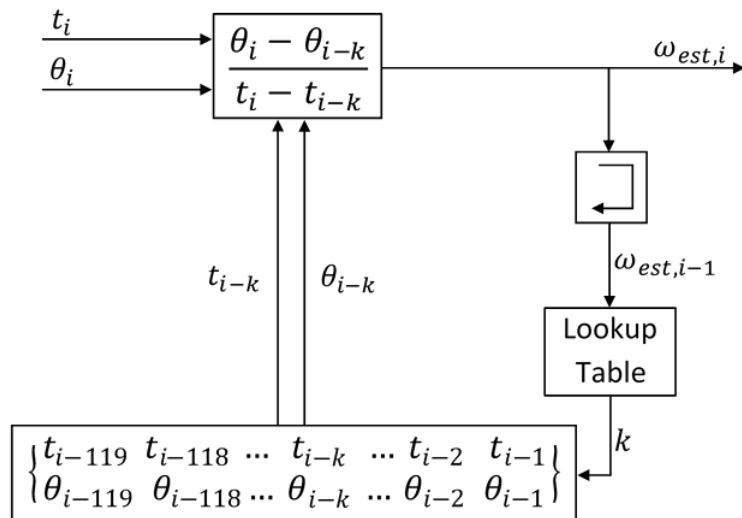


Figure 3.4.1 – Hybrid speed estimation with frequency-and-period estimation.

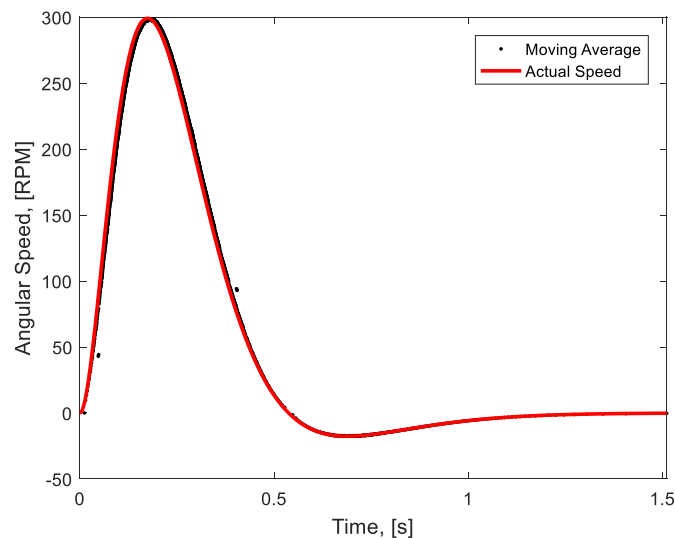


Figure 3.4.2 – Angular speed estimate with moving average and floating window.

The method provides the desired combination of tracking in low, mid, and high-speed ranges. It has a minor phase delay, which is expected as the algorithm can be interpreted as a type of derivative filter. The estimator’s performance is assessed by the relative error compared to the actual speed profile.

3.5 Relative errors of methods

The relative error for each of the provided methods is calculated (Figure 3.5.1, Figure 3.5.2, and Figure 3.5.3).

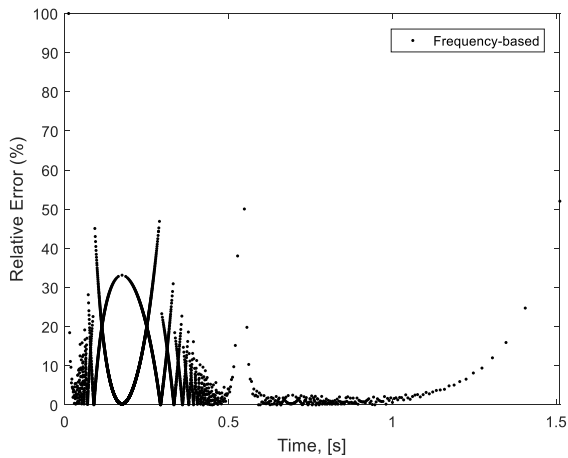


Figure 3.5.1 – Relative error, frequency-based.

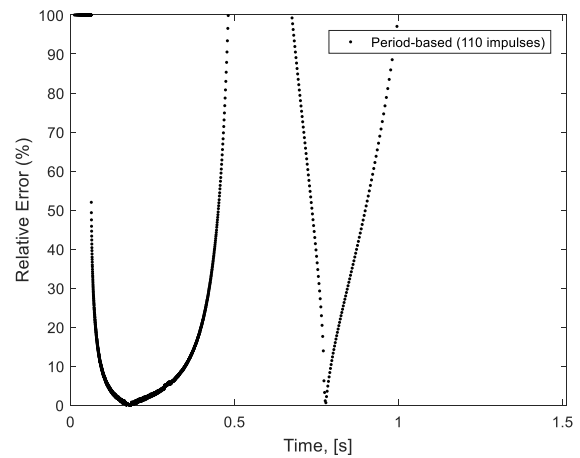


Figure 3.5.2 – Relative error, period-based.

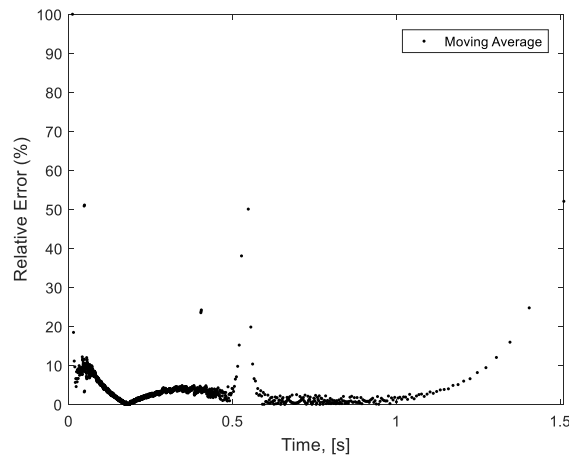


Figure 3.5.3 – Relative error, moving average with floating window.

With the period-based and frequency-based methods, the respective regions of high error are as discussed. The hybrid method combines the desirable low-and-high speed behaviours and improves the error across both speed regimes. The mean relative error is 3.1% with a standard deviation of 3.5%. There is still high relative error where the angular speed changes sign, but further correction is nontrivial, as the estimation method already makes use of all the position information in regions of near-zero speed.

3.6 Real-time implementation

To effect this angular speed estimation method in the NI VeriStand[®] framework, the method is translated into a Simulink[®] model (Figure 3.6.1) with the moving average and floating window described.

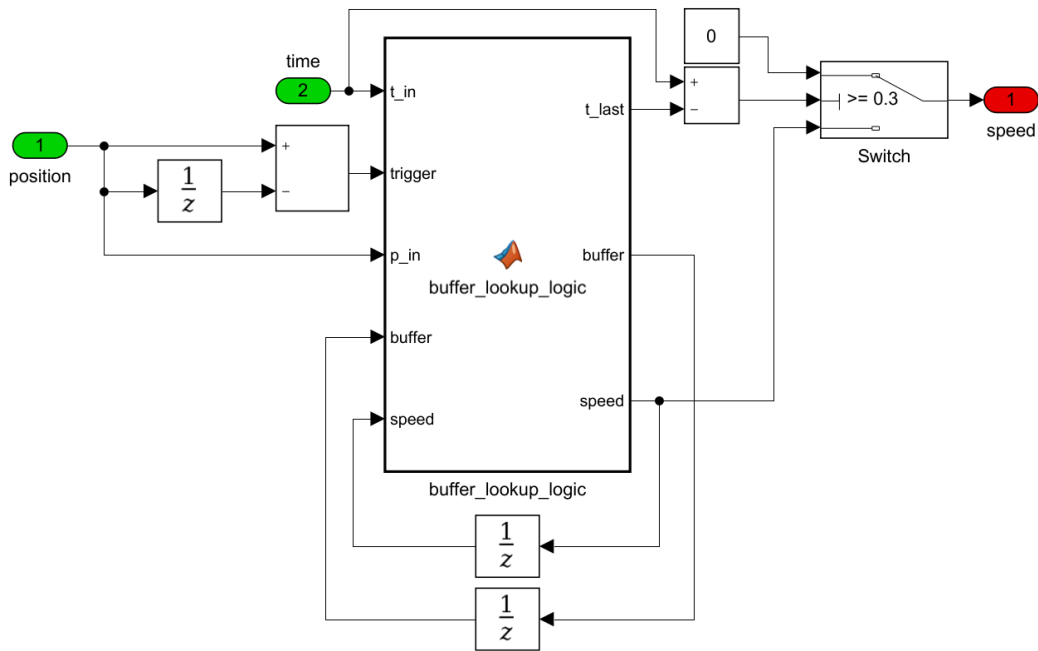


Figure 3.6.1 –Simulink® implementation of angular speed estimation.

The model takes a change in position as a trigger event for the estimation. A simple *if*-loop applies the lookup table, prioritising the speed of the algorithm. Another feature of note is a switch that sets the estimated speed to 0 if the time from the last *pulse* exceeds a threshold (here set to 0.3 seconds). This is necessary because the moving average recalculates only at a change in position. Zero speed causes no trigger and the estimated speed will always default to the last speed calculation and be non-zero; the model needs the switch to detect if the encoder has not moved from the last *pulse*.

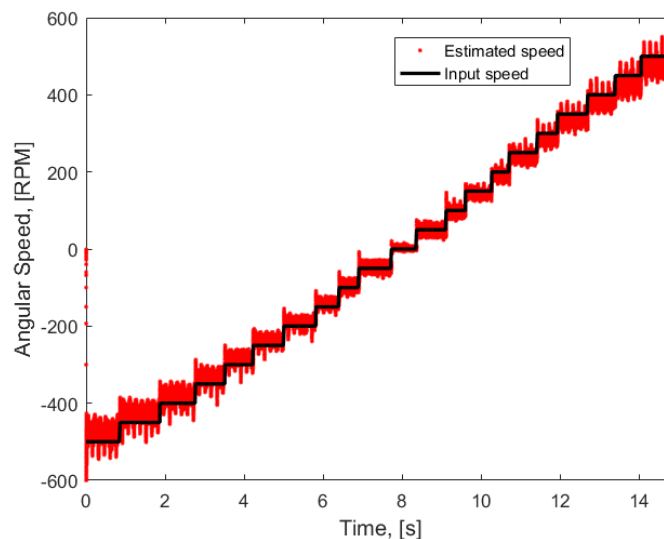


Figure 3.6.2 –Speed estimate obtained from motor position data.

Figure 3.6.2 shows the speed estimate for running the motor at tiered speeds between -500 and 500 rpm. The input is an open-loop scale of voltages to the unloaded motor. It is clear from the estimate that the motor speed is not strictly linear with voltage, and there is an error between the input speed and the average output speed. This error could be corrected through feedback [6] – for example, controlling the motor in an internal loop with a PI controller. Second, the estimate is noisier than predicted, which could require a filter or alternative processing.

The source of the noise could be an electrical phenomenon of the driver or a physical vibration in the motor. It is likely not external to the driver-motor pair because speed estimates using the free pendulum position are not subject to a similar noise (see Figure 3.6.4).

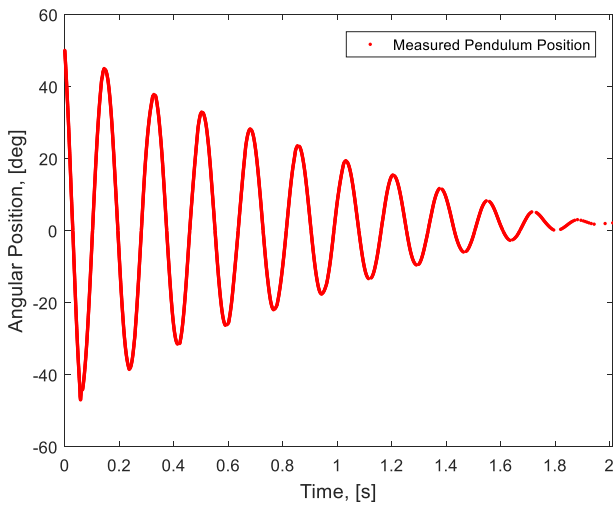


Figure 3.6.3 – Measured pendulum position.

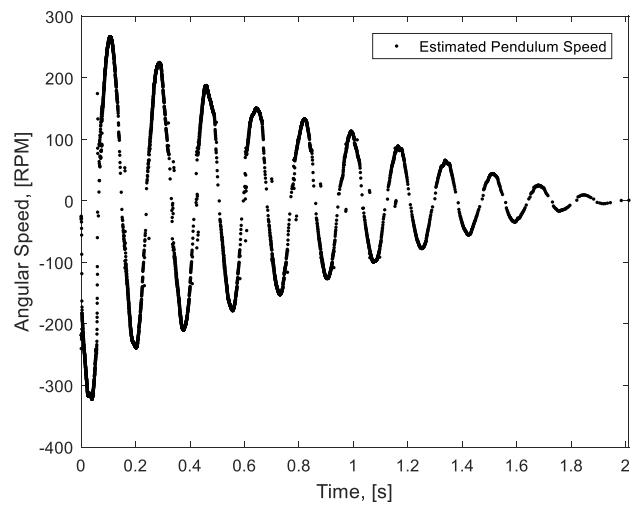


Figure 3.6.4 – Estimated pendulum speed.

3.7 Conclusions

Speed estimation from the incremental encoders is critical because they are the only sensors used for state measurements of the system. Since the states are also used to calculate the control action, the accuracy and perturbations of the position and speed estimates directly impact the observation and control of the pendulum. Because of this a robust angular speed estimator is an important first step to control. Typically sensors are paired with a low-pass filter, but at normal operating frequencies the position estimate is reliable while the challenge is with the frequency-sensitive speed estimation. In full operation the pendulum test bank collects data from three encoders: one for either motor and the pendulum, so any filtering is implemented in triple and must be computationally efficient for running in real-time. The speed estimator used acts as a simplified, lean derivative filter with minimal real-time cost. The cost is that the speed estimate is affected by the frequency behaviour of the filter itself, which imputes its own damping and phase delay; due to the unconventional structure of the estimator, these characteristics are difficult to calculate.

A consequence of using incremental encoders as sensors is that state sensing is sensitive to small-scale vibrations of the encoders. Small vibrations can trigger false quadrature of the encoder about a *pulse* threshold and cause the encoder to falsely sense a change in position. The encoder most sensitive to this phenomenon is the pendulum-paired encoder, which is mounted to the carriage and receives all transmission vibrations in X and Y. Because vibration in Y-motion is significantly greater than in X, a practical compensation will be to reduce Y-motion in control to improve the pendulum sensing accuracy. The effect on either motor or pendulum encoders is position creep, which can lose the location of the cart or pendulum. For the pendulum this is doubly critical because its equilibrium positions are no longer accurate. Zeroing procedures should be used to allow recalibration of the cart and pendulum positions.

4. System equations and state space

The analytical model for the pendulum test rig is revisited. Models for the pendulum test bank have been developed in previous theses [1][2], but the choice to control the pendulum through LQR requires a single analytical model consolidating all subsystems (pendulum, motors, and kinematic links) in state space. The previous work developed separate models for X-axis actuation of the plane pendulum, the carriage kinetics and kinematics, and a model of the motor in speed-control, significantly updated in this thesis [2]. The work presented abstracts the plane pendulum to XY movement of the carriage and combines these systems into a single set of equations for the plane pendulum, which are then linearized for the simple and inverted pendulum cases. Transmission kinematics are modelled with a new approach and terms are introduced to account for experimentally observed unmodelled losses. Additionally, the equations are updated to reflect a new choice of coordinate system and introduce the effect of viscous damping on the pendulum and carriage axis movement.

4.1 Pendulum and carriage

Despite the planar pendulum constraint, the system cannot be treated as if the cart moves solely along the X-axis. Because the motor and driver pairs are not the same, it is impossible to have motion perfectly isolated to the X-direction, so the model must be changed to account for the state Y. Furthermore, the state must also be accounted for because the motors produce bi-axis XY motion by default and the projected LQR (linear quadratic regulator) controller does not inherently prioritise planar motion; motion along the X-axis must be designed. Because it is also intended to control the cart in X and Y (for centring or servo behaviour), the system changes from MISO (multiple input single output) to MIMO (multiple input multiple output). This change makes controlling the system through PID impractical from a complexity and tuning standpoint, so an LQR scheme is chosen instead. Thus the target is an updated model accounting for XY motion of the cart, ultimately represented in a state space connecting the motor voltages as inputs to the output states of cart position and pendulum angle.

The model is developed by treating the pendulum and carriage together through Euler-Lagrange, then combining the resulting equations with the motor equations and transmission kinematics.

The plane pendulum is given in Figure 4.1.1, shown in the XZ plane as it is fixed to the carriage.

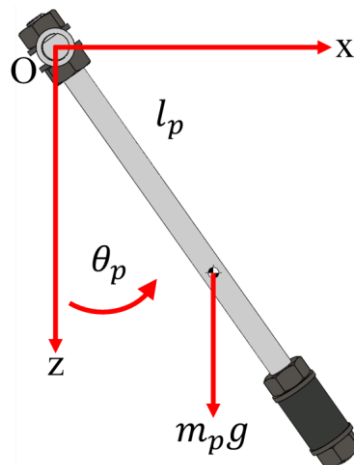


Figure 4.1.1 – Plane pendulum reference system.

The relevant parameters for the pendulum are given:

- θ_p : angular position of the pendulum;
- m_p : pendulum mass;
- l_p : distance between fulcrum and center of mass;
- c_p : viscous damping of the pendulum in rotation;
- J_p : mass moment of inertia of the pendulum about its center of mass;
- g : acceleration of gravity;
- x_p, y_p, z_p : position of the concentrated mass of the pendulum in X, Y, and Z directions.

The components of pendulum position are defined in the reference frame:

$$\begin{aligned} x_p &= x + l_p \sin \theta_p \\ y_p &= y \\ z_p &= z + l_p \cos \theta_p \end{aligned} \quad (4.1)$$

The time derivatives of eq. (4.1) find the components of pendulum velocity in the reference frame:

$$\begin{aligned} \dot{x}_p &= \dot{x} + l_p \dot{\theta}_p \cos \theta_p \\ \dot{y}_p &= \dot{y} \\ \dot{z}_p &= -l_p \dot{\theta}_p \sin \theta_p \end{aligned} \quad (4.2)$$

The transmission scheme and new coordinate system in the XY plane are given in Figure 4.1.2 [1].

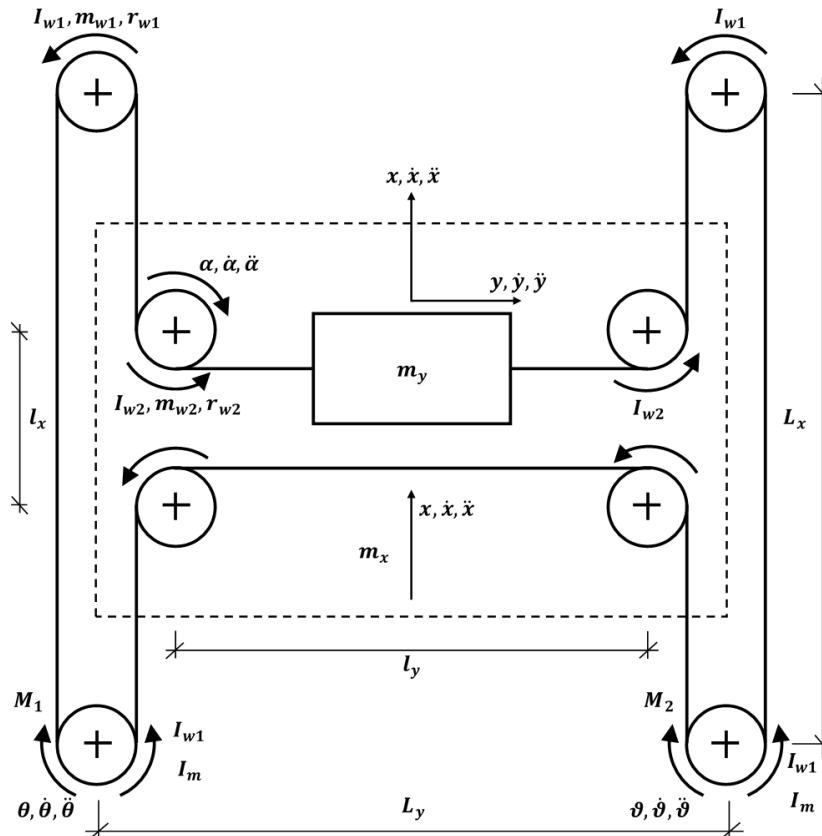


Figure 4.1.2 – Plane pendulum reference system.

The relevant parameters for the carriage and transmission are:

- x, y : displacement of the carriage in the planar and transverse directions;
- θ, ϑ : angular displacement of motor 1 and motor 2;
- α : angular displacement of the idlers;
- I_{w1}, I_{w2} : moments of inertia of the pulley and of the idler;
- m_{w1}, m_{w2} : masses of the pulley and of the idler;
- r_{w1}, r_{w2} : radii of the pulley and of the idler;
- I_m : moment of inertia of the motors (parameter provided by the manufacturer);
- m_x, m_y : isolated mass of the carriage moving in X and Y;
- c_x, c_y : viscous damping of the carriage in X and Y directions;
- c_p : approximated viscous damping of the pendulum;
- C_1, C_2 : torque provided by motor 1 and motor 2;
- F_y, F_x : force applied on the carriage in X and Y;
- L_x, L_y : distances between the centers of the pulleys;
- l_x, l_y : distances between the centers of the idlers;
- I_{b1}, I_{b2} : mass moment of inertia of the portions of the transmission belt rotating about the pulleys and idlers (eq. (4.8));
- μ : coefficient of friction along the linear guide;
- ρ : mass per unit length of the transmission belt;
- η : mechanical efficiency in power transmission, considered at 93%, due to elasticity of the belt.

The equations of motion for the carriage-pendulum subsystem are developed through Euler-Lagrange. As such, the lagrangian is defined:

$$L = T - V \quad (4.3)$$

$$L = T_{carriage,x} + T_{carriage,y} + T_{motors} + T_{pulleys} + T_{idlers} + T_{belt} + T_{pendulum} - V_{pendulum}$$

The chosen generalised coordinates are the same as the chosen system states:

$$q = \{x, y, \theta_p\} \quad (4.4)$$

$$\dot{q} = \{\dot{x}, \dot{y}, \dot{\theta}_p\}$$

The energy components can be defined in terms of cartesian coordinates and coordinates germane to the angular position of the motors. This is performed through the known kinematic relations, used for building the model, but also for translating the motor kinematics into the cart kinematics. Since the cart position and speed in X and Y are system states and there is no direct position sensing of the cart, this transformation is important.

$$\theta = \frac{-x - y}{r_{w1}} \quad (4.5)$$

$$\vartheta = \frac{x - y}{r_{w1}}$$

$$\alpha = \frac{y}{r_{w2}}$$

The time derivatives of these relations are:

$$\begin{aligned}\dot{\theta} &= \frac{-\dot{x} - \dot{y}}{r_{w1}} \\ \dot{g} &= \frac{\dot{x} - \dot{y}}{r_{w1}} \\ \dot{\alpha} &= \frac{\dot{y}}{r_{w2}}\end{aligned}\quad (4.6)$$

Each term of the Langrangian is defined in cartesian coordinate states x and y or the pendulum angle:

$$\begin{aligned}T_{carriage,x} &= \frac{1}{2} m_x \dot{x}^2 \\ T_{carriage,y} &= \frac{1}{2} m_y (\dot{x}^2 + \dot{y}^2) \\ T_{motors} &= \frac{I_m}{r_{w1}^2} (\dot{x}^2 + \dot{y}^2) \\ T_{pulleys} &= \frac{2I_{w1}}{r_{w1}^2} (\dot{x}^2 + \dot{y}^2) \\ T_{idlers} &= \frac{2I_{w2}}{r_{w2}^2} \dot{y}^2 \\ T_{belt} &= \left(2\rho(2L_x - l_x) + \frac{4I_{b1}}{r_{w1}^2} \right) \dot{x}^2 + \left(\rho l_y + \frac{4I_{b1}}{r_{w1}^2} + \frac{2I_{b2}}{r_{w2}^2} \right) \dot{y}^2 \\ T_{pendulum} &= \left(\frac{1}{2} J_p + \frac{1}{2} m_p l_p^2 \right) \dot{\theta}_p^2 + \frac{1}{2} m_p \dot{x}^2 + \frac{1}{2} m_p \dot{y}^2 + \dot{x} m_p l_p \dot{\theta}_p \cos \theta_p \\ V_{pendulum} &= m_p l_p g \cos \theta_p\end{aligned}\quad (4.7)$$

Where:

$$\begin{aligned}I_{b1} &= \frac{1}{16} \rho \pi r_{p1} (r_{p1}^2 - r_{w1}^2) \\ I_{b2} &= \frac{1}{16} \rho \pi r_{p2} (r_{p2}^2 - r_{w2}^2)\end{aligned}\quad (4.8)$$

Now Euler-Lagrange (eq. (4.9)) is applied to each of the generalised coordinates. Intermediate passages are skipped, but the resulting equations of motion for the cart and pendulum are given in eq. (4.10), where the generalised forces are the applied carriage forces F_x and F_y .

$$\frac{d}{dt} \left(\frac{\partial L}{\partial \dot{q}_k} \right) - \frac{\partial L}{\partial q_k} = Q_k \quad (4.9)$$

$$\begin{aligned}
M_{x,eq}\ddot{x} + c_x\dot{x} + \ddot{\theta}_p m_p l_p \cos \theta_p - m_p l_p \dot{\theta}_p^2 \sin \theta_p &= F_x \\
M_{y,eq}\ddot{y} + c_y\dot{y} &= F_y \\
(J_p + m_p l_p^2)\ddot{\theta}_p + c_p\dot{\theta}_p + \ddot{x} m_p l_p \cos \theta_p - m_p l_p g \sin \theta_p &= 0
\end{aligned} \tag{4.10}$$

Inertia terms are simplified into equivalent masses:

$$\begin{aligned}
M_{x,eq} &= m_x + m_y + m_p + \frac{2I_m}{r_{w1}^2} + \frac{4I_{w1}}{r_{w1}^2} + 4\rho(2L_x - l_x) + \frac{8I_{b1}}{r_{w1}^2} \\
M_{y,eq} &= m_y + m_p + \frac{2I_m}{r_{w1}^2} + \frac{4I_{w1}}{r_{w1}^2} + \frac{4I_{w2}}{r_{w2}^2} + 2\rho l_y + \frac{8I_{b1}}{r_{w1}^2} + \frac{4I_{b2}}{r_{w2}^2}
\end{aligned} \tag{4.11}$$

4.2 BLDC motor

Beginning from generic motor equations [2][7] for a DC motor relating motor position to motor torque and voltage to motor position (eq. (4.12)), a relation for motor torque solely in terms of the states x and y and input voltages to the motors will connect the system inputs to the equations of motion of eq. (4.11).

$$\begin{aligned}
v_m &= Ri + L \frac{d}{dt} i + k_e \dot{\theta} \\
J\ddot{\theta} &= k_t i + \beta \dot{\theta} + C_r
\end{aligned} \tag{4.12}$$

The parameters in the motor equations are:

- v_m : motor voltage;
- J : rotor mass moment of inertia;
- R : line to line resistance of the motor;
- L : terminal inductance;
- k_e : electric constant;
- k_t : torque constant;
- C_r : resistive couple;
- θ : motor angular position;
- i : armature current;

The generic motor transfer function has a first-order approximation when assuming that the current does not change [1]. The corresponding coefficients are set to zero:

$$\begin{aligned}
\beta &\approx 0 \\
L &\approx 0
\end{aligned} \tag{4.13}$$

The resulting first-order motor equations come from updating eq. (4.12) with the approximation:

$$\begin{aligned}
v_m &= Ri + k_e \dot{\theta} \\
J\ddot{\theta} &= k_t i + C_r
\end{aligned} \tag{4.14}$$

In prior work [2], the resistive couple was accounted for as a static opposition based on the system masses and friction moved by the motors, provided for completeness in Table 4.2.1 and Table 4.2.2. The moment is different for either motor in XY motion because in two-axis movement, one motor acts as a driver and the other as a hold.

Table 4.2.1 – C_r of motor 1 in the 3 motion configurations.

Configuration	C_r
X	$\pm \frac{1}{\eta} (\mu(m_x + m_p + m_y)g)r_{wl}$
Y	$\pm \frac{1}{\eta} (\mu(m_y + m_p)g)r_{wl}$
XY	$\pm \frac{1}{\eta} (\mu(2(m_y + m_p) + m_x)g)r_{wl}$

Table 4.2.2 – C_r of motor 2 in the 3 motion configurations.

Configuration	C_r
X	$\pm \frac{1}{\eta} (\mu(m_x + m_p + m_y)g)r_{wl}$
Y	$\pm \frac{1}{\eta} (\mu(m_y + m_p)g)r_{wl}$
XY	$\pm \frac{1}{\eta} (\mu m_x g)r_{wl}$

XY motion is assumed because the motor and driver pairs are not exactly equal. However, instead of using the static terms from the tables, the resistive couple is accounted for by updating the rotor inertia by an effective inertia of the system seen by the motor. Updating eq. (4.14) with this gives eq. (4.15), which directly relates the effective inertia to the current.

$$J_{eff} \ddot{\theta} = k_t i \quad (4.15)$$

It is also known that the moment produced by the motor is given by the product of the torque constant and the current, eq. (4.16):

$$k_t i = C_m \quad (4.16)$$

By combining eq. (4.15) and eq. (4.16), the motor moment can be substituted and the new set of motor equations found, where the current term can be eliminated by substitution (eq. (4.17)). This is important because there is no reliable measure of current in the test rig, so it is desired to eliminate it as a state.

$$i = \frac{1}{R} (v_m - k_e \dot{\theta}) \quad (4.17)$$

$$C_m = k_t i$$

By substituting, the current term is eliminated:

$$C_m = \frac{k_t}{R} v_m - \frac{k_e k_t}{R} \dot{\theta} \quad (4.18)$$

Because both motor and driver pairs are different, each has their own estimated parameters. These are represented by two separate motor equations, one for each motor, each relating the output moment to the voltage input and motor position. Lastly, the motor equations are updated to be in terms of the states x and y of the cart position using the kinematic relation from eq. (4.6):

$$\begin{aligned} C_1 &= \frac{\hat{k}_{e,1} \hat{k}_{t,1}}{\hat{R}_1 r_{w1}} \dot{x} + \frac{\hat{k}_{e,1} \hat{k}_{t,1}}{\hat{R}_1 r_{w1}} \dot{y} + \frac{\hat{k}_{t,1}}{\hat{R}_1} v_1 \\ C_2 &= -\frac{\hat{k}_{e,2} \hat{k}_{t,2}}{\hat{R}_2 r_{w1}} \dot{x} + \frac{\hat{k}_{e,2} \hat{k}_{t,2}}{\hat{R}_2 r_{w1}} \dot{y} + \frac{\hat{k}_{t,2}}{\hat{R}_2} v_2 \end{aligned} \quad (4.19)$$

To complete the equations of motion for the system, a link is needed between the forces on the carriage in eq. (4.11) and the motor moments eq. (4.19). The link comes in eq. (4.20) which emerges from the system geometry and experimentally adjusted gains which account for the motor driving and holding described above as well as unmodelled attrition which cause general losses.

$$\begin{aligned} F_x &= -\frac{\eta \gamma_{m1} \gamma_{fx}}{r_{w1}} C_1 + \frac{\eta \gamma_{m2} \gamma_{fx}}{r_{w1}} C_2 \\ F_y &= -\frac{\eta \gamma_{m1} \gamma_{fy}}{r_{w1}} C_1 - \frac{\eta \gamma_{m2} \gamma_{fy}}{r_{w1}} C_2 \end{aligned} \quad (4.20)$$

4.3 State space equations

The equations obtained above are combined, a complete nonlinear set of equations is found for the system, and then it is linearized and converted into the state space. First the carriage equations are given in canonical nonlinear form in eq. (4.21). A unitless gain is added on the force in the carriage X-direction as seen by the pendulum, which is experimentally tuned.

$$\begin{aligned} \ddot{x} &= \frac{1}{M_{x,eq} - \frac{m_p^2 l_p^2 \cos^2 \theta_p}{J_{eq}}} \left[\begin{array}{l} -c_x \dot{x} + \frac{m_p l_p \cos \theta_p}{J_{eq}} c_p \dot{\theta}_p + \frac{m_p^2 l_p^2 g}{J_{eq}} \cos \theta_p \sin \theta_p \\ + m_p l_p \dot{\theta}_p^2 \sin \theta_p + F_x \end{array} \right] \\ \ddot{y} &= \frac{1}{M_{y,eq}} [-c_y \dot{y} + F_y] \\ \ddot{\theta}_p &= \frac{1}{J_{eq} - \frac{m_p^2 l_p^2 \cos^2 \theta_p}{M_{x,eq}}} \left[\begin{array}{l} -c_p \dot{\theta}_p + \frac{m_p l_p \cos \theta_p}{M_{x,eq}} c_x \dot{x} - \frac{m_p^2 l_p^2}{M_{x,eq}} \dot{\theta}_p^2 \cos \theta_p \sin \theta_p \\ - m_p l_p g \sin \theta_p - \frac{m_p l_p \cos \theta_p}{\alpha_{mx} M_{x,eq}} F_x \end{array} \right] \end{aligned} \quad (4.21)$$

The definitions for the forces on the carriage from eq. (4.20) are substituted into the canonical carriage equations of motion from eq. (4.21), then the motor equations for each motor couple are substituted. The result is a cononical nonlinear system of equations in terms of the states x and y cart position and pendulum position with motor voltage inputs, given in eq. (4.22).

It should be noted that the equations of motion assume and are therefore only valid when the motors are driving the cart. Because of feedback through the cart speed, the equations of motion suggest that the cart could be used to drive the motors if they were disabled, which is incorrect, but this is a use case outside of the operation conditions.

$$\begin{aligned}
\ddot{x} &= M_x^* \left[\begin{aligned} & -\left(c_x + \gamma_{fx}(u_{m1} + u_{m2})\right)\dot{x} + \gamma_{fx}(-u_{m1} + u_{m2})\dot{y} + \frac{m_p l_p c_p \cos \theta_p}{J_{eq}} \dot{\theta}_p \\ & + \frac{m_p^2 l_p^2 g}{J_{eq}} \cos \theta_p \sin \theta_p + m_p l_p \dot{\theta}_p^2 \sin \theta_p - \frac{\gamma_{fx} r_{w1} u_{m1}}{\hat{k}_{e,1}} v_1 + \frac{\gamma_{fx} r_{w1} u_{m2}}{\hat{k}_{e,2}} v_2 \end{aligned} \right] \\
\ddot{y} &= M_y^* \left[\begin{aligned} & \gamma_{fy}(-u_{m1} + u_{m2})\dot{x} - \left(c_y + \gamma_{fy}(u_{m1} + u_{m2})\right)\dot{y} - \frac{\gamma_{fy} r_{w1} u_{m1}}{\hat{k}_{e,1}} v_1 - \frac{\gamma_{fy} r_{w1} u_{m2}}{\hat{k}_{e,2}} v_2 \end{aligned} \right] \\
\ddot{\theta}_p &= J_{eq}^* \left[\begin{aligned} & \left(\frac{m_p l_p c_x \cos \theta_p}{M_{x,eq}} + \frac{m_p l_p \gamma_{fx} \cos \theta_p}{\alpha_{mx} M_{x,eq}} (u_{m1} + u_{m2}) \right) \dot{x} - c_p \dot{\theta}_p \\ & - \left(\frac{m_p l_p \gamma_{fx} \cos \theta_p}{\alpha_{mx} M_{x,eq}} (-u_{m1} + u_{m2}) \right) \dot{y} - \frac{m_p^2 l_p^2}{M_{x,eq}} \dot{\theta}_p^2 \cos \theta_p \sin \theta_p \\ & - m_p l_p g \sin \theta_p + \frac{m_p l_p \gamma_{fx} r_{w1} u_{m1} \cos \theta_p}{\alpha_{mx} M_{x,eq} \hat{k}_{e,1}} v_1 - \frac{m_p l_p \gamma_{fx} r_{w1} u_{m2} \cos \theta_p}{\alpha_{mx} M_{x,eq} \hat{k}_{e,2}} v_2 \end{aligned} \right] \quad (4.22)
\end{aligned}$$

Where the simplified terms are:

$$\begin{aligned}
u_{m1} &= \frac{\eta \gamma_{m1} \hat{k}_{e,1} \hat{k}_{t,1}}{\hat{R}_1 r_{w1}^2} \\
u_{m2} &= \frac{\eta \gamma_{m2} \hat{k}_{e,2} \hat{k}_{t,2}}{\hat{R}_2 r_{w1}^2} \\
M_x^* &= \frac{1}{M_{x,eq} - \frac{m_p^2 l_p^2 \cos^2 \theta_p}{J_{eq}}} \\
M_y^* &= \frac{1}{M_{y,eq}} \\
J_{eq}^* &= \frac{1}{J_{eq} - \frac{m_p^2 l_p^2 \cos^2 \theta_p}{M_{x,eq}}} \quad (4.23)
\end{aligned}$$

The state space representation can be applied only to linear systems, so the canonical equations of eq. (4.22) are linearized. For the simple pendulum, linearizing about the equilibrium point 0 with small-angle assumptions gives:

$$\begin{aligned}\cos \theta_p &\approx 1 \\ \sin \theta_p &\approx \theta_p\end{aligned}\quad (4.24)$$

When applied to eq. (4.22), the linearized simple pendulum equations are:

$$\begin{aligned}\ddot{\mathbf{x}} &= M_x^* \begin{bmatrix} -\left(c_x + \gamma_{fx}(u_{m1} + u_{m2})\right)\dot{x} + \gamma_{fx}(-u_{m1} + u_{m2})\dot{y} + \frac{m_p l_p c_p}{J_{eq}} \dot{\theta}_p + \frac{m_p^2 l_p^2 g}{J_{eq}} \theta_p \\ -\frac{\gamma_{fx} r_{w1} u_{m1}}{\hat{k}_{e,1}} v_1 + \frac{\gamma_{fx} r_{w1} u_{m2}}{\hat{k}_{e,2}} v_2 \end{bmatrix} \\ \ddot{\mathbf{y}} &= M_y^* \begin{bmatrix} \gamma_{fy}(-u_{m1} + u_{m2})\dot{x} - \left(c_y + \gamma_{fy}(u_{m1} + u_{m2})\right)\dot{y} - \frac{\gamma_{fy} r_{w1} u_{m1}}{\hat{k}_{e,1}} v_1 - \frac{\gamma_{fy} r_{w1} u_{m2}}{\hat{k}_{e,2}} v_2 \end{bmatrix} \\ \ddot{\theta}_p &= J_{eq}^* \begin{bmatrix} \pm \left(\frac{m_p l_p c_x}{M_{x,eq}} + \frac{m_p l_p \gamma_{fx}}{\alpha_{mx} M_{x,eq}} (u_{m1} + u_{m2}) \right) \dot{x} - \left(\frac{m_p l_p \gamma_{fx}}{\alpha_{mx} M_{x,eq}} (-u_{m1} + u_{m2}) \right) \dot{y} - c_p \dot{\theta}_p \\ -m_p l_p g \theta_p + \frac{m_p l_p \gamma_{fx} r_{w1} u_{m1}}{\alpha_{mx} M_{x,eq} \hat{k}_{e,1}} v_1 - \frac{m_p l_p \gamma_{fx} r_{w1} u_{m2}}{\alpha_{mx} M_{x,eq} \hat{k}_{e,2}} v_2 \end{bmatrix}\end{aligned}\quad (4.25)$$

In contrast, for the inverted pendulum, linearizing about the equilibrium point π [8] gives:

$$\begin{aligned}\cos \theta_p &\approx -1 \\ \sin \theta_p &\approx \pi - \theta_p\end{aligned}\quad (4.26)$$

When substituted, there is a static term in π that must be accounted for within the dynamic state space representation. This is achieved by introducing a new variable for the pendulum angle that is offset by π ; the derivatives of the new variable are the same as the original state:

$$\begin{aligned}\theta_p^\diamond &= \theta_p - \pi \\ \dot{\theta}_p^\diamond &= \dot{\theta}_p \\ \ddot{\theta}_p^\diamond &= \ddot{\theta}_p\end{aligned}\quad (4.28)$$

Applying the change of variable, the linearized equations of motion for the inverse pendulum are:

$$\begin{aligned}
\ddot{x} &= M_x^* \begin{bmatrix} -\left(c_x + \gamma_{fx}(u_{m1} + u_{m2})\right)\dot{x} + \gamma_{fx}(-u_{m1} + u_{m2})\dot{y} - \frac{m_p l_p c_p}{J_{eq}} \dot{\theta}_p^\diamond \\ -\frac{m_p^2 l_p^2 g}{J_{eq}} \theta_p^\diamond - \frac{\gamma_{fx} r_{w1} u_{m1}}{\hat{k}_{e,1}} v_1 + \frac{\gamma_{fx} r_{w1} u_{m2}}{\hat{k}_{e,2}} v_2 \end{bmatrix} \\
\ddot{y} &= M_y^* \begin{bmatrix} \gamma_{fy}(-u_{m1} + u_{m2})\dot{x} - \left(c_y + \gamma_{fy}(u_{m1} + u_{m2})\right)\dot{y} - \frac{\gamma_{fy} r_{w1} u_{m1}}{\hat{k}_{e,1}} v_1 - \frac{\gamma_{fy} r_{w1} u_{m2}}{\hat{k}_{e,2}} v_2 \end{bmatrix} \\
\ddot{\theta}_p^\diamond &= J_{eq}^* \begin{bmatrix} -\left(\frac{m_p l_p c_x}{M_{x,eq}} + \frac{m_p l_p \gamma_{fx}}{\alpha_{mx} M_{x,eq}}(u_{m1} + u_{m2})\right)\dot{x} + \left(\frac{m_p l_p \gamma_{fx}}{\alpha_{mx} M_{x,eq}}(-u_{m1} + u_{m2})\right)\dot{y} \\ -c_p \dot{\theta}_p^\diamond + m_p l_p g \theta_p^\diamond - \frac{m_p l_p \gamma_{fx} r_{w1} u_{m1}}{\alpha_{mx} M_{x,eq} \hat{k}_{e,1}} v_1 + \frac{m_p l_p \gamma_{fx} r_{w1} u_{m2}}{\alpha_{mx} M_{x,eq} \hat{k}_{e,2}} v_2 \end{bmatrix}
\end{aligned} \tag{4.27}$$

Beside the offset in the pendulum angle, the only difference between the linearized cases is the sign on some of the coefficients, so the two cases can be paired into eq. (4.29), the consolidated linearized canonical equations of motion, where the change of variable is reflected elsewhere in the choice of pendulum angle state.

$$\begin{aligned}
\ddot{x} &= M_x^* \begin{bmatrix} -\left(c_x + \gamma_{fx}(u_{m1} + u_{m2})\right)\dot{x} + \gamma_{fx}(-u_{m1} + u_{m2})\dot{y} \pm \frac{m_p l_p c_p}{J_{eq}} \dot{\theta}_p \pm \frac{m_p^2 l_p^2 g}{J_{eq}} \theta_p \\ -\frac{\gamma_{fx} r_{w1} u_{m1}}{\hat{k}_{e,1}} v_1 + \frac{\gamma_{fx} r_{w1} u_{m2}}{\hat{k}_{e,2}} v_2 \end{bmatrix} \\
\ddot{y} &= M_y^* \begin{bmatrix} \gamma_{fy}(-u_{m1} + u_{m2})\dot{x} - \left(c_y + \gamma_{fy}(u_{m1} + u_{m2})\right)\dot{y} - \frac{\gamma_{fy} r_{w1} u_{m1}}{\hat{k}_{e,1}} v_1 - \frac{\gamma_{fy} r_{w1} u_{m2}}{\hat{k}_{e,2}} v_2 \end{bmatrix} \\
\ddot{\theta}_p &= J_{eq}^* \begin{bmatrix} \pm \left(\frac{m_p l_p c_x}{M_{x,eq}} + \frac{m_p l_p \gamma_{fx}}{\alpha_{mx} M_{x,eq}}(u_{m1} + u_{m2})\right)\dot{x} \mp \left(\frac{m_p l_p \gamma_{fx}}{\alpha_{mx} M_{x,eq}}(-u_{m1} + u_{m2})\right)\dot{y} - c_p \dot{\theta}_p \\ \mp m_p l_p g \theta_p \pm \frac{m_p l_p \gamma_{fx} r_{w1} u_{m1}}{\alpha_{mx} M_{x,eq} \hat{k}_{e,1}} v_1 \mp \frac{m_p l_p \gamma_{fx} r_{w1} u_{m2}}{\alpha_{mx} M_{x,eq} \hat{k}_{e,2}} v_2 \end{bmatrix}
\end{aligned} \tag{4.29}$$

With these equations, the inputs, outputs, and states of the state space are declared:

$$\begin{aligned}
z &= \{\dot{x} \quad \dot{y} \quad \dot{\theta}_p \quad x \quad y \quad \theta_p\}^T \\
u &= \{v_1 \quad v_2\}^T \\
y &= \{x \quad y \quad \theta_p\}^T
\end{aligned} \tag{4.30}$$

The general representation of the state space is:

$$\begin{aligned}
\dot{z} &= Az + Bu \\
y &= Cz + Du
\end{aligned} \tag{4.31}$$

The linearized equations of motion from eq. (4.29) can be represented in matrix form as:

$$\begin{Bmatrix} \ddot{x} \\ \ddot{y} \\ \ddot{\theta}_p \end{Bmatrix} = [\mathbf{G}^*] \begin{Bmatrix} \dot{x} \\ \dot{y} \\ \dot{\theta}_p \end{Bmatrix} + [\mathbf{K}^*] \begin{Bmatrix} x \\ y \\ \theta_p \end{Bmatrix} + [\mathbf{V}] \begin{Bmatrix} v_1 \\ v_2 \end{Bmatrix} \quad (4.32)$$

The damping (eq. (4.33)), stiffness (eq. (4.34)), and input matrix (eq. (4.35)) are defined:

$$[\mathbf{G}^*] = \begin{bmatrix} -M_x^* (c_x + \gamma_{fx} (u_{m1} + u_{m2})) & M_x^* \gamma_{fx} (-u_{m1} + u_{m2}) & \pm M_x^* \frac{m_p l_p c_p}{J_{eq}} \\ M_y^* \gamma_{fy} (-u_{m1} + u_{m2}) & -M_y^* (c_y + \gamma_{fy} (u_{m1} + u_{m2})) & - \\ \pm J_{eq}^* \left(\frac{m_p l_p c_x}{M_{x,eq}} + \frac{m_p l_p \gamma_{fx}}{\alpha_{mx} M_{x,eq}} (u_{m1} + u_{m2}) \right) & \mp J_{eq}^* \left(\frac{m_p l_p \gamma_{fx}}{\alpha_{mx} M_{x,eq}} (-u_{m1} + u_{m2}) \right) & -J_{eq}^* c_p \end{bmatrix} \quad (4.33)$$

$$[\mathbf{K}^*] = \begin{bmatrix} - & - & \pm M_x^* \frac{m_p^2 l_p^2 g}{J_{eq}} \\ - & - & - \\ - & - & \mp J_{eq}^* m_p l_p g \end{bmatrix} \quad (4.34)$$

$$[\mathbf{V}] = \begin{bmatrix} -M_x^* \frac{\gamma_{fx} r_{w1} u_{m1}}{\hat{k}_{e,1}} & M_x^* \frac{\gamma_{fx} r_{w1} u_{m2}}{\hat{k}_{e,2}} \\ -M_y^* \frac{\gamma_{fy} r_{w1} u_{m1}}{\hat{k}_{e,1}} & -M_y^* \frac{\gamma_{fy} r_{w1} u_{m2}}{\hat{k}_{e,2}} \\ \pm J_{eq}^* \frac{m_p l_p \gamma_{fx} r_{w1} u_{m1}}{\alpha_{mx} M_{x,eq} \hat{k}_{e,1}} & \mp J_{eq}^* \frac{m_p l_p \gamma_{fx} r_{w1} u_{m2}}{\alpha_{mx} M_{x,eq} \hat{k}_{e,2}} \end{bmatrix} \quad (4.35)$$

Moving to the state space eq. (4.36), the damping and stiffness matrices are combined to form the state matrix A in eq. (4.37); the direct input matrix is also found (eq. (4.38)):

$$\begin{Bmatrix} \ddot{x} \\ \ddot{y} \\ \ddot{\theta}_p \\ \dot{x} \\ \dot{y} \\ \dot{\theta}_p \end{Bmatrix} = [\mathbf{A}] \begin{Bmatrix} \dot{x} \\ \dot{y} \\ \dot{\theta}_p \\ x \\ y \\ \theta_p \end{Bmatrix} + [\mathbf{B}] \begin{Bmatrix} v_1 \\ v_2 \end{Bmatrix} \quad (4.36)$$

$$[A] = \begin{bmatrix} & [G^*] & [K^*] & & & \\ 1 & - & - & - & - & - \\ - & 1 & - & - & - & - \\ - & - & 1 & - & - & - \end{bmatrix} \quad (4.37)$$

$$[B] = \begin{bmatrix} [V] \\ - \\ - \\ - \end{bmatrix} \quad (4.38)$$

4.4 Motor parameter estimation

Each brushless electric motor used in the pendulum test rig is paired with a driver which changes the composite motor-driver system because of its internal electronics and control logic. An estimated model of the motors is the beginning of a model of the total pendulum test rig in control because the motors connect the sole inputs (motor voltage) to the kinematics of the belt, carriage, and pendulum.

A generic DC electric motor has the following transfer function between output speed and input voltage [9]:

$$\frac{\Omega(s)}{V(s)} = \frac{k_t}{LJs^2 + (RJ + L\beta)s + (k_e k_t + R\beta)} \quad (4.39)$$

Nominal values of the parameters are provided by the manufacturer (Table 4.4.1). These values would be used to estimate the actual parameters for both BN34-BLDC motors used in the test bank, but the motors are never an isolated unit in the rig since they are always paired with a dedicated SCA-B4-70-30 driver. The driver has internal electronics and a tuneable control logic, which undoubtedly affect the composite motor-driver transfer function. Furthermore, the structure of the driver transfer function is unknown, so the effect is black-box dynamics.

Typically the internal control loop of a driver will have a much larger bandwidth than the motor it controls so as to be dynamically negligible. It is decided to model the driver as if it changes the values of the motor's electrical parameters but not the order of the transfer function itself, so there remains a second-order transfer function with unknown variables. To aid in the estimation, the nominal parameter for the rotor inertia, (J in eq (4.39)) is taken as the nominal value since this physical property is unchanged by the driver pairing. This leaves five unknown motor parameters to be estimated:

- R : line-to-line equivalent resistance;
- L : terminal inductance;
- β : coefficient of friction (physical property, expected close to nominal);
- k_e : electric constant (tuneable);
- k_t : torque constant (tuneable unknown).

Of these parameters, the electric constant k_e can be found directly from the DC speed output, leaving four unknown parameters.

The objective of the motor parameter estimation is to use both the DC and frequency behaviour of the unloaded motor-driver pair to build an experimental transfer function of the target order that can

be compared to the target transfer function given in eq (4.39). Because this is an opaque function of six parameters, the function is compared to the prototypical transfer function of a generic second-order system with a gain (eq (4.40)), which has intuitive properties in gain, damping, and natural frequency; it is also beneficial because the time response of this system to a step input is known.

$$G(s) = \frac{k\omega_n^2}{s^2 + 2\zeta\omega_n s + \omega_n^2} \quad (4.40)$$

To compare the DC motor transfer function to the second-order prototype, eq (4.39) is rearranged to give the same gain, damping, and natural frequency form as eq (4.40):

$$\frac{\Omega(s)}{V(s)} = \frac{\left(\frac{k_t}{k_e k_t + R\beta}\right)\left(\frac{k_e k_t + R\beta}{LJ}\right)}{s^2 + 2\left(\frac{RJ + L\beta}{2LJ\sqrt{\frac{k_e k_t + R\beta}{LJ}}}\right)\sqrt{\frac{k_e k_t + R\beta}{LJ}}s + \left(\frac{k_e k_t + R\beta}{LJ}\right)} \quad (4.41)$$

The procedure is to use the motor-driver step response and frequency response to estimate an equivalent gain, damping, and natural frequency, and then compare by fitting the prototype transfer function to the rearranged generic DC motor transfer function in eq (4.41).

Table 4.4.1 – BLDC BN34-25EU-02LH nominal parameters.

Nominal Motor Parameter	J, mass moment of inertia [kg m ²]	R, line-to-line resistance [Ω]	L, terminal inductance [H]	β, coefficient of friction [Nms]	k _e , electric constant [Vs/rad]	k _t , torque constant [Nm/A]
Value	5.1e-5	0.253	6.2e-4	9e-6	0.06	0.06

Estimation begins from the motor-driver DC characteristics to estimate the electric constant k_e and assess the step response. DC data is taken in two parts, highlighted in black and blue in Figure 4.4.1 and Figure 4.4.2. The first figure gives the input voltage to the motor and the second gives the speed output of the unloaded motor. In both these figures, the black section of data is a scale of speed outputs for different voltage inputs along the entire input voltage range ($\pm 24V$). The second section is the step response when stepping from top speed to top speed in the other direction. This step is repeated three times to improve the estimate.

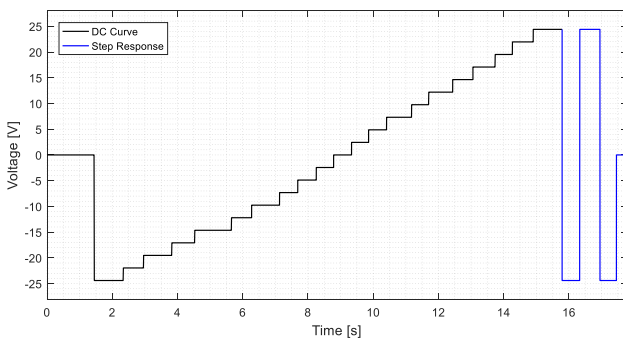


Figure 4.4.1 – DC step voltage, motor 1.

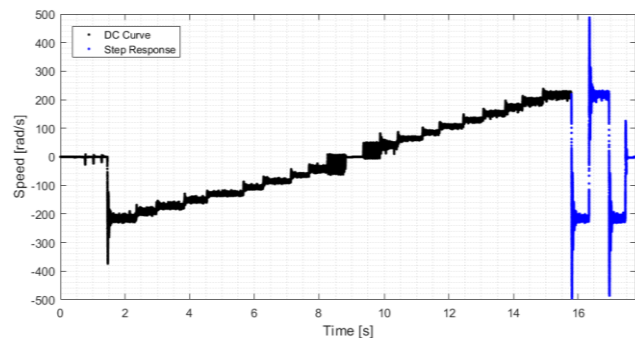


Figure 4.4.2 – DC step speed, motor 1.

From the scale of output speeds along the range of input voltages, a voltage-speed curve can be charted. The electric constant k_e is the relation between the input voltage and the speed:

$$V = k_e \Omega \tag{4.42}$$

In Figure 4.4.3 the clear linear tendency of the voltage-speed curve gives an estimated value of 0.1129 for the motor-driver 1 voltage constant k_{e1} . Repeating the procedure for motor-driver 2 in Figure 4.4.4 finds an estimated k_{e2} value of 0.1167.

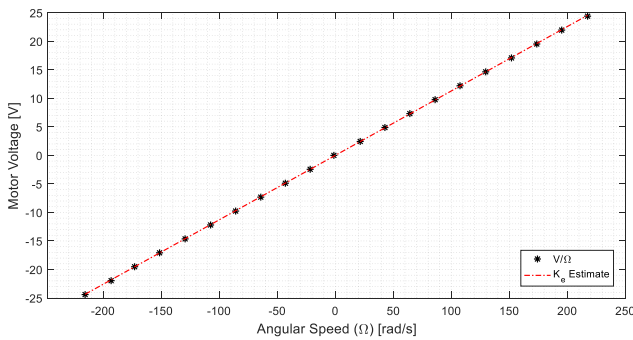


Figure 4.4.3 – K_e tendency, motor 1.

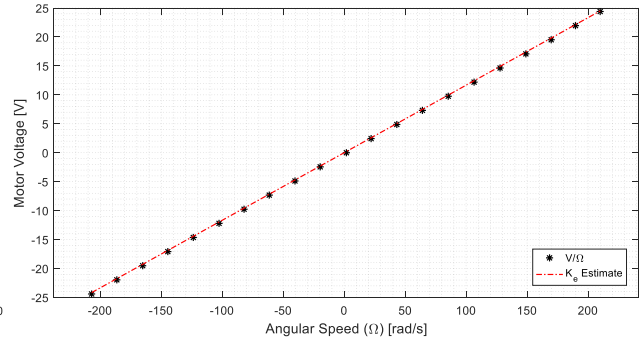


Figure 4.4.4 – K_e tendency, motor 2.

In the second section of the DC data, the response of the motor speed and position to a step reference input is measured. The shape of the position response is shown in Figure 4.4.5 and the speed response in Figure 4.4.6 with typical second-order overshoot. This step data can be compared to the time response of the prototype second-order system (eq (4.45)); the prototype response is fit to the three steps in both position and speed to obtain an aggregate idea of the natural frequency and damping of the unknown transfer function.

The procedure for the second motor-driver pair follows that of the first, but where the first has a bandwidth within the frequency range studied, the second motor-driver is much faster than the first, outside of the frequency range that can be captured with the sampling rate, so that the poles of the transfer function cannot be directly observed. Another critical difference is that, while the first pair behaved like the desired second-order system, this motor and driver do not fit the prototype as well. It is unclear whether differences in the driver or the tuning of the pair, or some internal dynamics of the second motor itself cause the composite system to not behave as if it were of the same order.

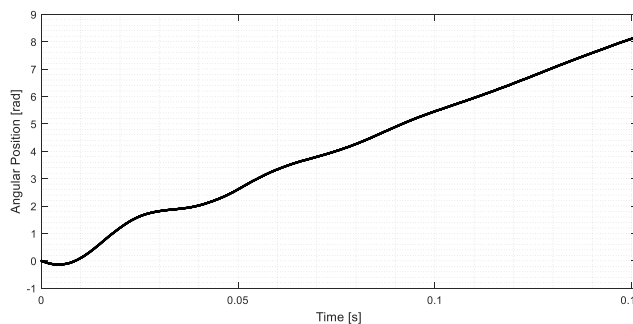


Figure 4.4.5 – Position step response, motor 1.

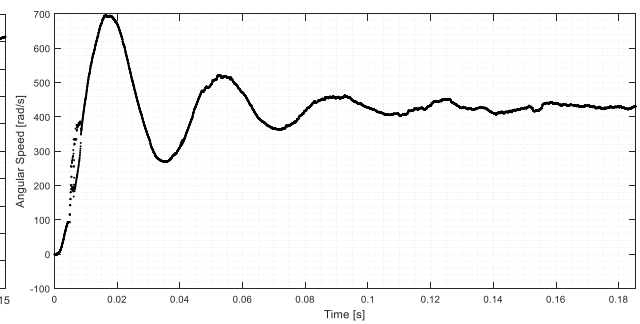


Figure 4.4.6 – Speed step response, motor 1.

In the Laplace domain, the step response of the second-order prototype system $G(s)$ is given by:

$$\Omega(s) = u(s)G(s) \tag{4.43}$$

Where the unit impulse is:

$$u(s) = \frac{1}{s} \quad (4.44)$$

It should be noted that in Laplace, the gain, k , of $G(s)$ is ambiguous; it can be the gain of the transfer function or a scaling of the step input, demonstrated in eq (4.45). This does not affect the fit, but it means that the gain should be estimated from the frequency response instead.

$$u(s)G(s) = \frac{k}{s} \frac{\omega_n^2}{s^2 + 2\zeta\omega_n s + \omega_n^2} \quad (4.45)$$

The time-domain speed response is found in eq (4.46):

$$\dot{\theta}(t) = \mathcal{L}^{-1} \{u(s)G(s)\} = k - ke^{-t\omega_n\zeta} \left[\cos(t\omega_n\sqrt{1-\zeta^2}) + \frac{\zeta}{\sqrt{1-\zeta^2}} \sin(t\omega_n\sqrt{1-\zeta^2}) \right] \quad (4.46)$$

Similarly, since the position is ideally the integral of the speed, the position response is the integral of the speed step response; this is performed using the integrator in Laplace:

$$\theta(t) = \mathcal{L}^{-1} \left\{ \frac{1}{s} u(s)G(s) \right\} \quad (4.47)$$

Through inverse Laplace the time-domain position response is:

$$\theta(t) = kt - k \frac{2\zeta}{\omega_n} + k \frac{2\zeta}{\omega_n} e^{-t\omega_n\zeta} \left[\cos(t\omega_n\sqrt{1-\zeta^2}) - \frac{1-2\zeta^2}{2\zeta\sqrt{1-\zeta^2}} \sin(t\omega_n\sqrt{1-\zeta^2}) \right] \quad (4.48)$$

For each response of position or speed, the ideal time response is fitted to the data. The reason for treating both the position and speed data, which should ideally yield the same estimate, is because the angular position of the motor is measured accurately from the attached incremental encoder but the angular speed of the motor is estimated using a specialized moving average estimator, a type of filter, and therefore has its own phase delay and gain which, however minimal, alters the speed measurement. As such it is advantageous to use all available information to gather an idea of how well the estimate fits.

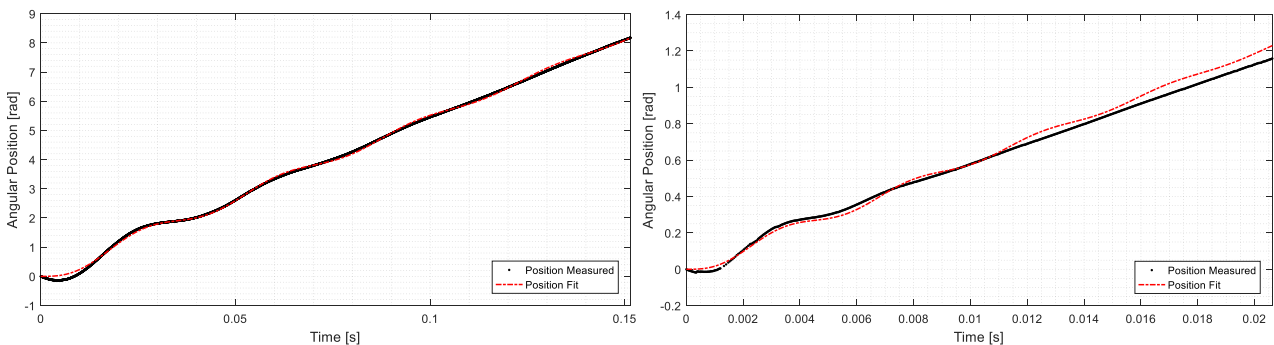


Figure 4.4.7 – Fitted position response, motor 1.

Figure 4.4.8 – Fitted position response, motor 2.

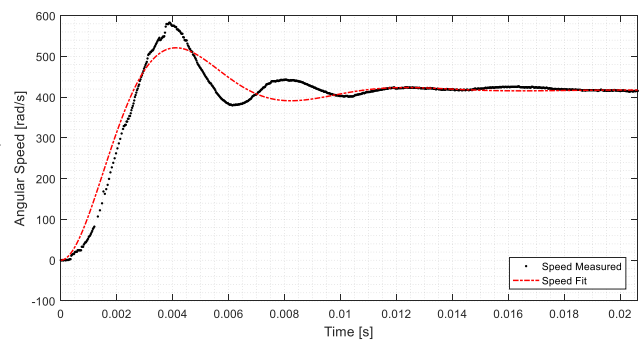
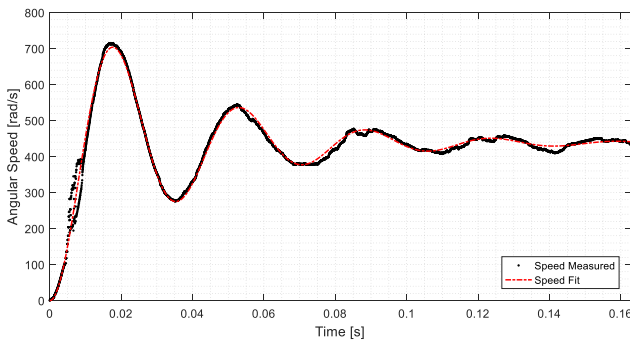


Figure 4.4.9 – Fitted speed response, motor 1.

Figure 4.4.10 – Fitted speed response, motor 2.

The fitted position and speed responses for motor-driver 1 are given in Figure 1.2.6 (one of the three runs). The initial transience is captured well with what seems to be a small underestimate of the damping. With all the fits going forward, the parameters of gain, damping, and natural frequency for all three runs are aggregated into a single estimate; the same is done for the speed step response. As indicated previously, the estimated gain k is ambiguous and not useful information for the step response, but there is a clear agreement between the position and speed response for the natural frequency for motor-driver 1. As anticipated, the step responses in position (Figure 4.4.8) and speed (Figure 4.4.10) show that the motor-driver pair 2 is much faster than the first. Also seen from fitting the prototype step responses is that there is a significant difference between the shape of the prototype response and the data. It should also be noted that (catalogued in Table 4.4.2) the standard deviation is much higher for the three step response runs than in the first motor-driver pair; there is much less consistency in the operation.

With motor-driver 2, the position step response (Figure 4.4.8) appears to give a good estimate of the frequency, even if the gain and damping do not match well. From the estimate the natural frequency is near 1300 rad/s, over seven times faster than the first motor-driver. The origin of this difference is unclear; it is possible that the drivers have significant electrical differences. Another possibility is that the manual tuning of the motor and driver, which involves tuning two gains based on the chattering of the motor -which in turn depends on mechanical differences in the motors- causes this great increase.

The speed of the system poses a problem for the speed estimator. As stated before, the speed estimator works as a filter, and the filter does not have the bandwidth to accurately capture behaviour this fast; it can approximate the loaded speed, which is enough for the control system, but the resulting data is transformed and will clearly not fit an ideal response. As such, the best fit of a second-order prototype is poor, with unreliable estimates for all parameters.

Moving to the frequency domain, the experimental transfer function of the unknown motor-driver system is constructed by giving as input a well-defined harmonic function of constant amplitude and varying frequencies, and then finding the output speed. It is known that the steady-state response of a forced harmonic system is at the forcing frequency; so by finding the output speed at the frequency of the input and then by finding the magnitude of that output signal, the experimental transfer function can be established across a range of frequencies.

The motor-driver input voltage (mid-voltage input) is a constant amplitude harmonic signal:

$$v(t) = 7.32 \sin(\omega_f t) \quad (4.49)$$

With ω_f as the forcing frequency ranging between 0.1 and 600 rad/s. The increasing-frequency speed response for both motors are shown in in Figure 4.4.11 and Figure 4.4.12. The data is affected

by significant noise, more notably for motor-driver 2. The speed data is affected by more noise at higher frequencies because the motor itself is noisier than motor 1.

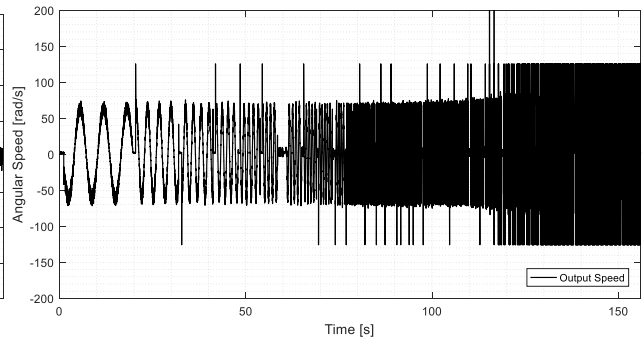
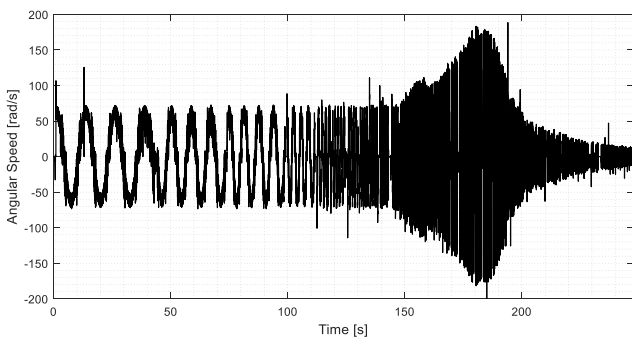


Figure 4.4.11 – Frequency speed output, motor 1. Figure 4.4.12 – Frequency speed output, motor 2.

The first step is to filter the speed data using a notch filter. Since the steady-state output signal of interest is at the forcing frequency, each section of data (segmented by input frequency) is filtered with a notch filter at that segment’s frequency. The initial transience seen at the beginning of the time is also removed, leaving only the steady-state response at the forcing frequency.

As an example, filtering of a section of constant forcing frequency at 70 rad/s is shown in Figure 4.4.13.

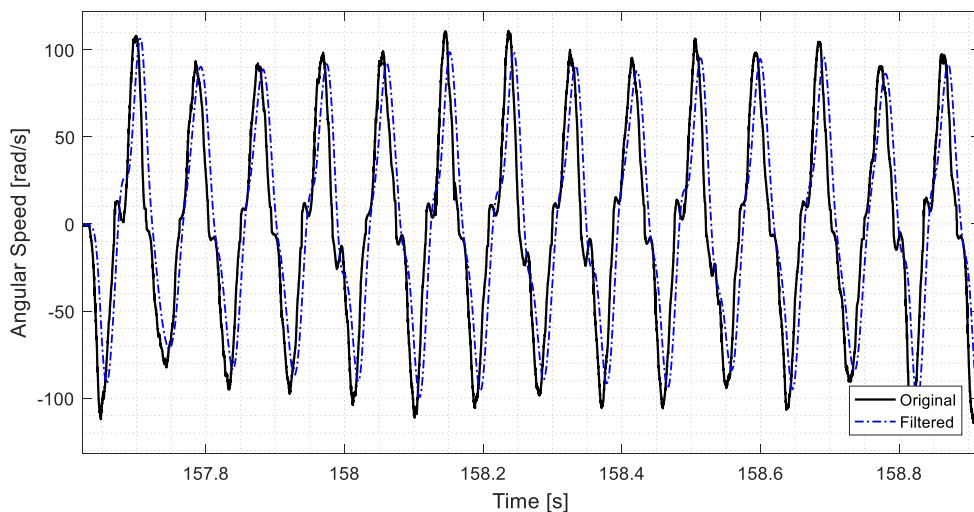


Figure 4.4.13 – Example notch-filtered speed (70 rad/s), motor 1.

The filtered speed data is fitted to the prototype harmonic signal (eq (4.50)), shown for a section at 70 rad/s in Figure 4.4.14. A similar fit is done for the voltage input data, Figure 4.4.15.

The prototype harmonic at forcing frequency has two variables to fit: the amplitude, A , and the phase delay, φ :

$$\Omega(t) = A \sin(\omega_f t + \varphi) \tag{4.50}$$

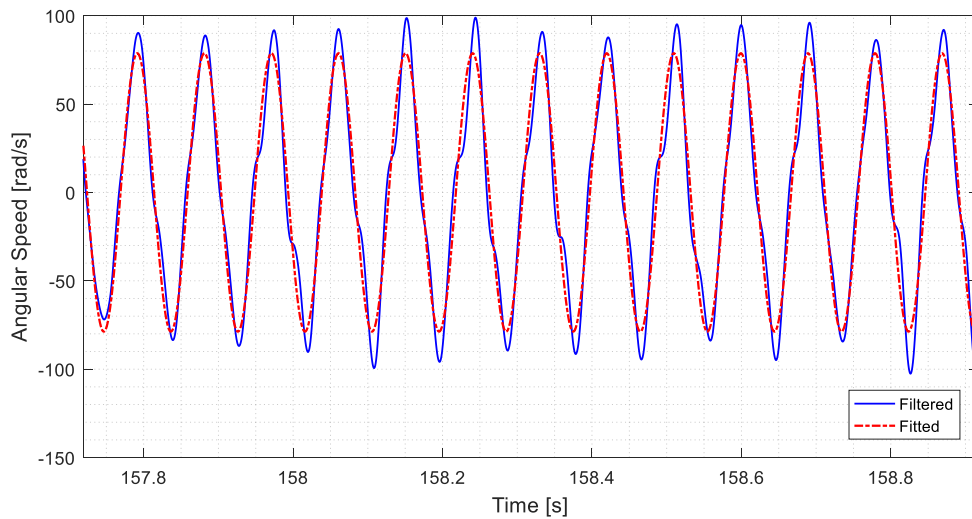


Figure 4.4.14 – Example fitted speed output (70 rad/s), motor 1.

The voltage is also fit to a prototype harmonic signal, though it does not require filtering because the data is extremely clean (Figure 1.2.14).

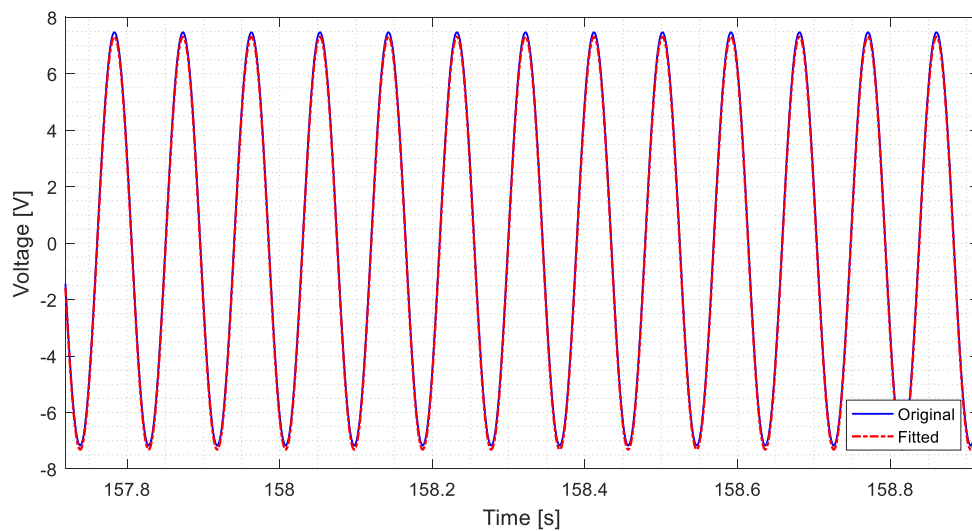


Figure 4.4.15 – Example fitted voltage input (70 rad/s), motor 1.

The input and output signals for a frequency segment are compared, this time with the clean, fitted signals. The difference between the original signals and the input/outputs after filtering and fitting can be seen with Figure 4.4.16 and Figure 4.4.17 at an example frequency of 70 rad/s.

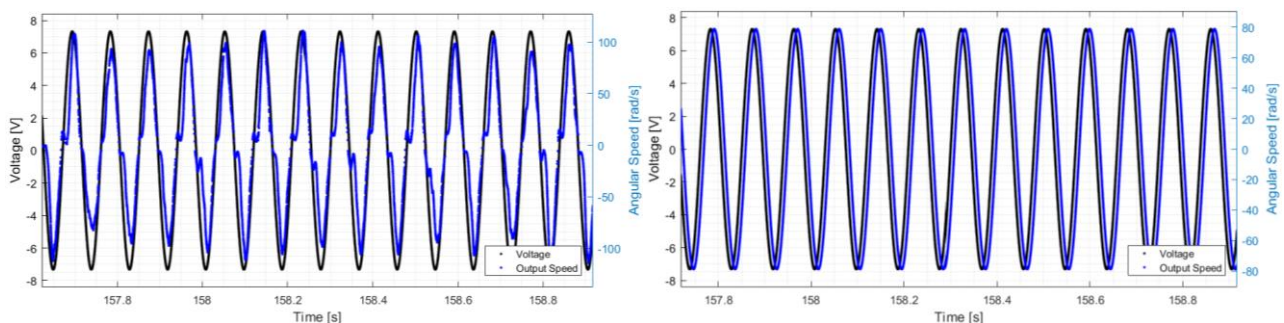


Figure 4.4.16 – Example raw input/output. Figure 4.4.17 – Example cleaned input/output.

The input is a harmonic voltage and the output is a harmonic speed at the same frequency, though affected by a small phase delay. With both input and output signals found for each frequency point, the amplitude of the signals can be compared to reach the frequency response experimental transfer function of the motor/driver pair (Figure 4.4.18 for motor 1 and Figure 4.4.19 for motor 2). The great difference between the motor-driver pairs is that the range of frequencies studied does not capture the pole behaviour of the transfer function of motor 2. The system cannot be studied with higher frequency inputs because the sampling rate is not large enough to describe the harmonic signal and information is lost to aliasing, most visible in the high frequency of Figure 4.4.18.

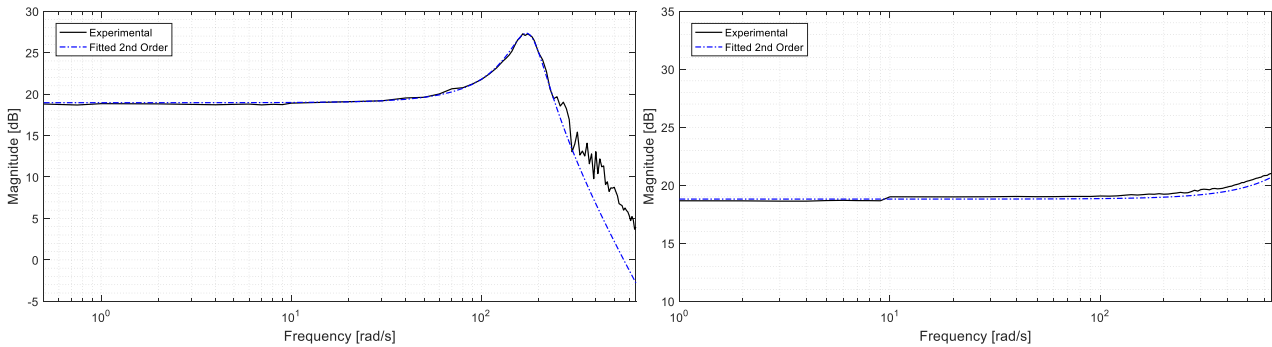


Figure 4.4.18 – Transfer function, motor 1. Figure 4.4.19 – Transfer function, motor 2.

The frequency response transfer function is then fit to the prototype second-order system of eq (4.40) to again estimate the gain, damping, and natural frequency of the system. The compiled prototype parameter data for the position, speed, and frequency response for both motor-drivers is listed in Table 4.4.2.

Table 4.4.2 – Position, speed, and frequency response aggregate prototype parameters.

		Motor 1		Motor 2	
Estimated Prototype Parameter	Method	Value	Standard Deviation	Value	Standard Deviation
k, gain [-]	Position Response	54.76	0.22	54.98	4.17
	Speed Response	108.37	1.40	99.92	6.23
	Frequency Response	2.218	-	2.18	-
ζ , damping ratio [-]	Position Response	0.058	1.7e-3	0.159	0.139
	Speed Response	0.155	3.5e-3	0.407	0.055
	Frequency Response	0.193	-	0.205	-
ω_n , natural frequency [rad/s]	Position Response	178.7	0.447	1277.1	101.28
	Speed Response	181.0	1.027	739.34	86.55
	Frequency Response	179.49	-	1391	-

The relative error of the frequency domain fits are shown in Figure 4.4.20. At low and mid-frequencies the fit error is low with a greater error at higher frequencies that can be attributed to aliasing due to the sampling frequency. From the comparison, the fit is good enough to validate the assumption that the motor-driver composite system can be modelled by a second-order system like the generic DC motor.

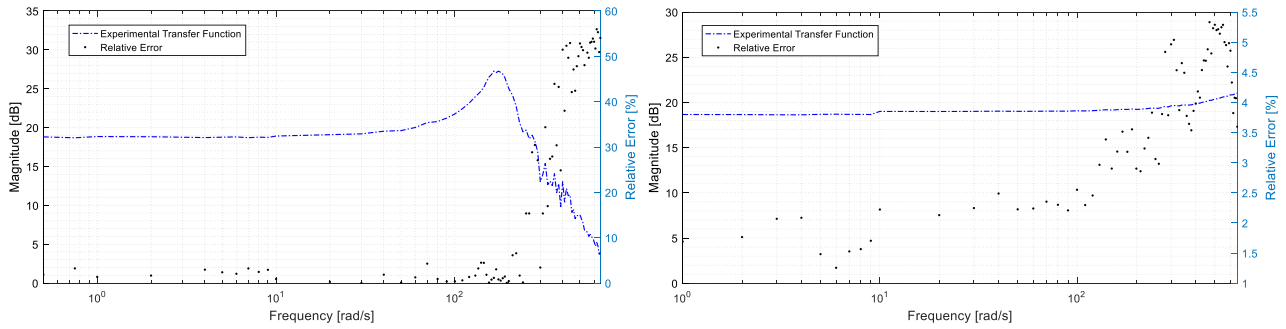


Figure 4.4.20 – Relative error on prototype transfer function, motor 1 (left) and relative error on prototype transfer function, motor 2 (right).

The transfer functions obtained by all the different methods (position and speed step response, frequency response) are compiled for motor-driver 1 in Figure 4.4.21 and in Figure 4.4.22 for motor-driver 2, with their normalized step responses shown in Figure 4.4.23. The benefit of these comparisons is to evaluate the appropriateness of the damping and frequency of each estimate using the intuitive parameters of the prototype second-order system.

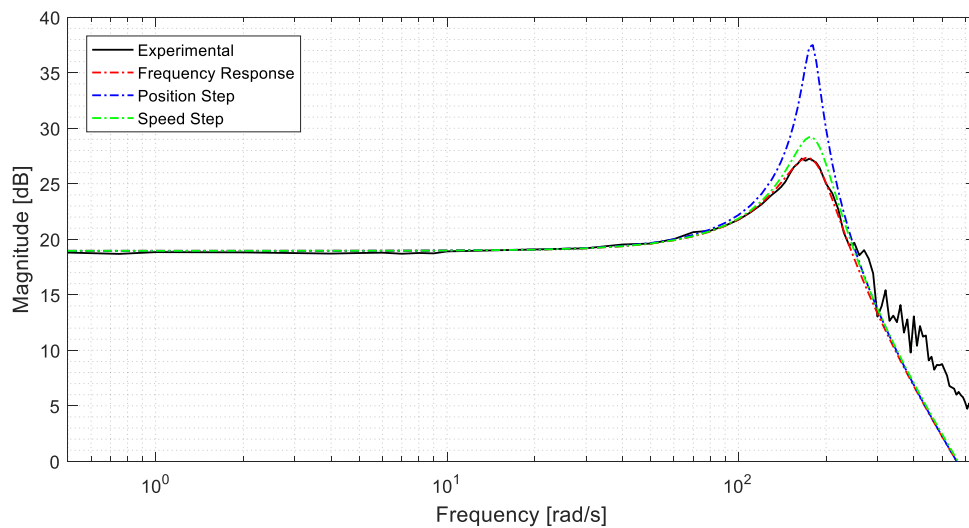


Figure 4.4.21 – Plotting of transfer functions from different response methods, motor 1.

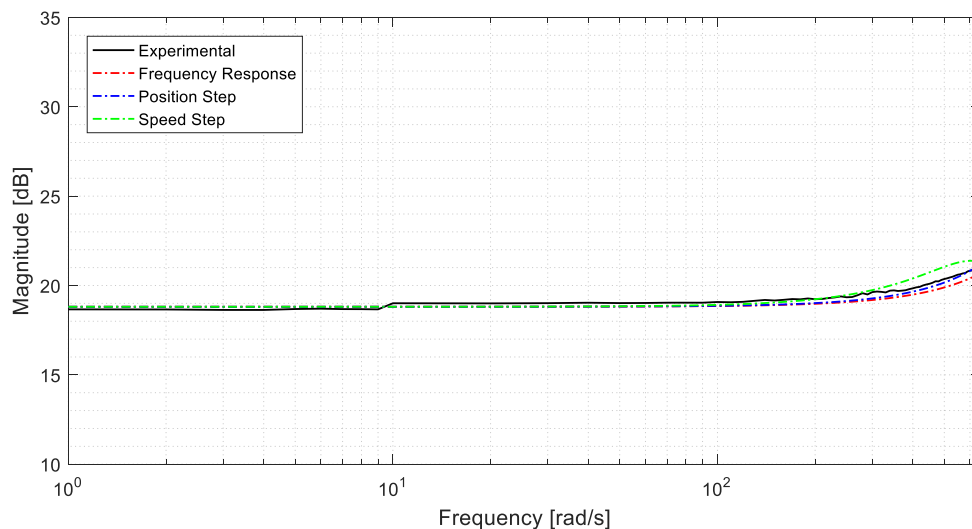


Figure 4.4.22 – Plotting of transfer functions from different response methods, motor 2.

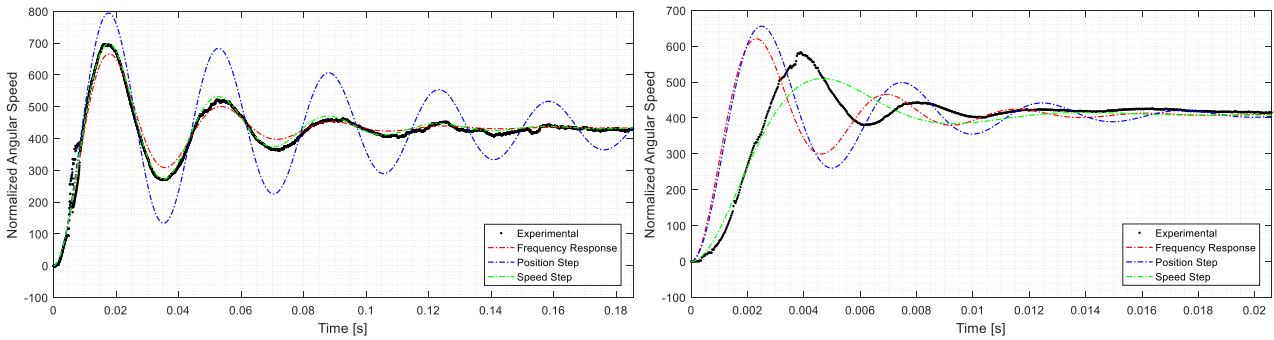


Figure 4.4.23 – Normalized step responses, motor 1 (left) and normalized step responses, motor 2 (right).

A target transfer function for either motor-driver pair is set based on the best estimate for the prototype parameters. Because of the good fit for motor-driver 1, all estimates have nearly the same natural frequency, and the target gain is taken from the frequency response. The only critical determination is the correct damping. As discussed previously, the function that estimates speed from angular position data acts as a derivative filter, so the damping of this filter at higher frequencies must also be considered. The filter has a heuristic decrement of around 15% at the higher frequencies in the range studied here, so the magnitude of the frequency response around the resonance is slightly underestimated. Because of this, the best match for damping value seems to be the damping from the speed response estimate, whose transfer function has the appropriate underdamped behaviour near resonance.

For the second motor a target second-order transfer function is fit to the data using the frequency response gain, a natural frequency of the order observed in the position step response (1300 rad/s), and an approximate damping drawn from the speed data, accounting for the damping of the speed estimator. Since the control system will not operate outside the frequency range studied, for the transfer function it is more important to match the low-frequency dynamics than the mid-range. However, since the composite motor parameters will be estimated using the total transfer function, representing the damping as well as possible is important for these estimates to be informed by the system behaviour itself.

From the considerations on gain, damping, and natural frequency, the chosen values are combined to form the target prototype second-order transfer function, compiled in Table 4.4.3.

Table 4.4.3 – Target prototype transfer function parameters.

Estimated Prototype Parameter	k , gain [-]	ζ , damping ratio [-]	ω_n , natural frequency [rad/s]
Motor 1	8.872	0.155	179.49
Motor 2	8.720	0.205	1391

With the target transfer function set, what remains is to compare it to the motor transfer function of the same form (eq (4.41)). After applying the found electric constant k_e and applying the assumption that the motor inertia, J , is close to the nominal value, there are four unknowns in the motor transfer function. From the target transfer function there are three parameters found, so the system is underdetermined. The motor transfer function in four unknowns is fit to the target using a least-squares fit.

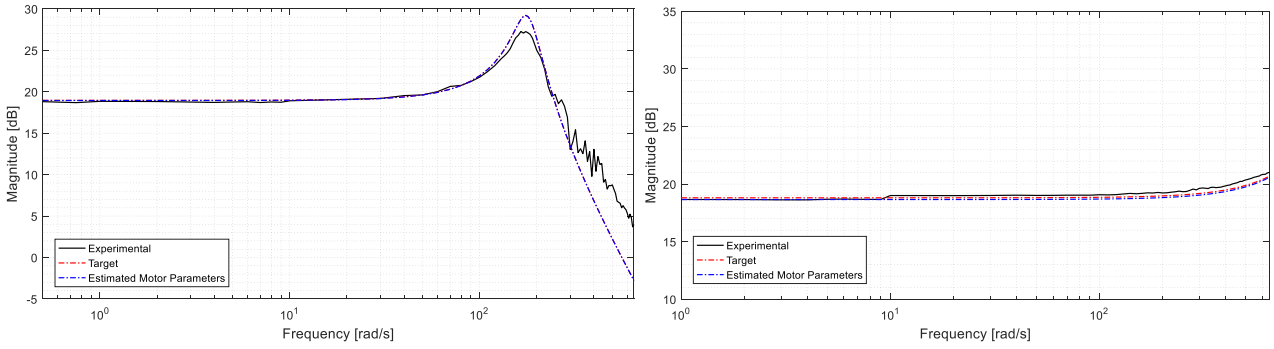


Figure 4.4.24 – Comparison of target to estimated parameter transfer function, motor 1 (left) and comparison of target to estimated parameter transfer function, motor 2 (right).

The fitted transfer function (in red) is compared to the target (in blue) in frequency domain in Figure 4.4.24 to show the fit, and the estimated motor parameters found using the least-squares are reported in Table 4.4.4. A minimal-error solution is achievable for the better condition motor-driver 1, and a reasonable solution is found for motor 2.

Table 4.4.4 – Estimated composite driver and motor 1 parameters.

Parameter	\hat{J}_1 , mass moment of inertia [kg m ²]	\hat{R}_1 , line-to-line resistance [Ω]	\hat{L}_1 , terminal inductance [H]	$\hat{\beta}_1$, coefficient of friction [Nms]	\hat{k}_{e1} , electric constant [Vs/rad]	\hat{k}_{t1} , torque constant [Nm/A]
Motor 1	5.1e-5	0.0929	1.66e-3	3.23e-6	0.4517	6.06e-3
Motor 2	5.1e-5	0.1846	3.63e-4	1.059e-5	0.4667	0.0768

The fit for motor-driver 2 is not perfect; there is a slight difference in gain and damping, but given the deviation from ideal present in all of the motor-driver 2 performance, it is an acceptable estimate. The speed step response of both target and estimated transfer function of motor-driver 2 is shown in Figure 4.4.25. This highlights the difference in damping, though the frequency and location of the mid-frequency dynamics is reliably estimated.

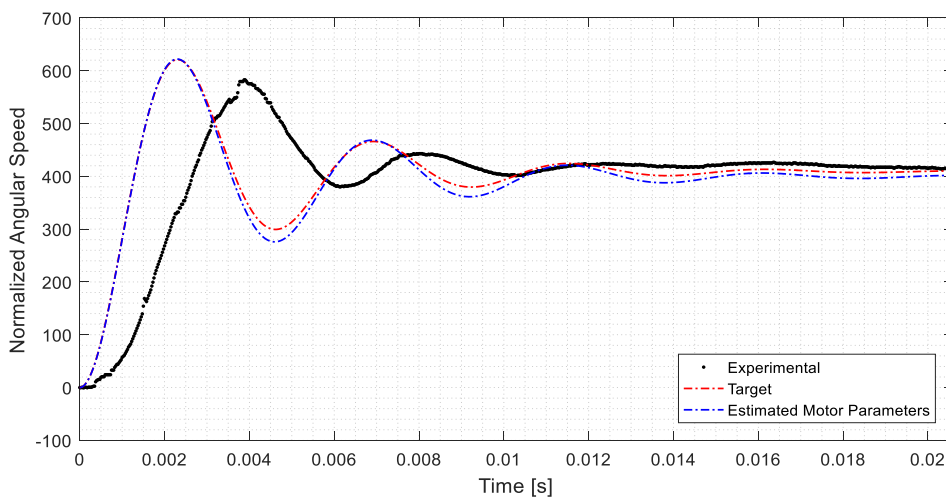


Figure 4.4.25 – Step response of target and motor estimated parameter transfer function, motor 2.

4.5 Pendulum damping estimation

To study the pendulum damping, the cart is fixed so that there can be no translational movement. The only degree of freedom is the free rotation of the pendulum about its axle. The plane pendulum configuration can be referenced in in Figure 4.1.1.

The equation of motion of this one degree of freedom system is eq (4.51), which is nonlinear in the pendulum angle. There are four pendulum parameters which affect the trajectory, three of which are known and listed in Table 4.5.1. The only unknown is c_p , the pendulum damping, modelled in this case as a viscous damping.

$$J_p \ddot{\theta}_p + c_p \dot{\theta}_p + m_p l_p g \sin \theta_p = M \quad (4.51)$$

Table 4.5.1 – Properties of fabricated pendulum.

Parameter	Value
m_p , mass [g]	72.40
l_p , distance fulcrum to center of mass [mm]	91.5
J_p , mass moment of inertia (with axle) [kg m ²]	6.65e-5

With only one unknown the simplest method of estimation is to sample the free position response of the real pendulum and compare it to the nonlinear ideal solution, adjusting the damping until the model fits the real pendulum behaviour. The free response of the pendulum is collected for three different initial starting angles: 15°, 25°, and 45°, which is the maximum oscillating range of the pendulum due to the cart geometry. These runs are shown in totality in Figure 4.5.1, where the three sections are the damped harmonics and the fluctuations in-between are the positioning of the pendulum at its initial angle.

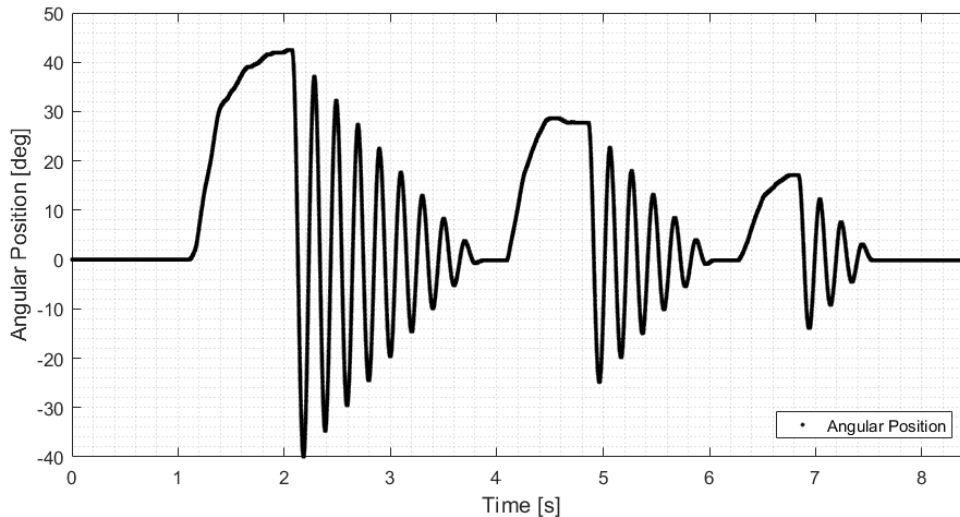


Figure 4.5.1 – Free pendulum response at different initial angles.

The nonlinear pendulum model is fit against the experimental data. To solve the second-order differential equation, the equation is split into a system of two first-order equations (eq (4.52) and eq (4.53)).

$$\begin{aligned}x_1 &= \theta_p \\x_2 &= \dot{\theta}_p\end{aligned}\tag{4.52}$$

$$\begin{aligned}\dot{x}_1 &= x_2 \\ \dot{x}_2 &= -\frac{c_p}{J_p}x_2 - \frac{m_p l_p}{J_p} \sin x_1 + \frac{M}{J_p}\end{aligned}\tag{4.53}$$

M is the external moment applied to the pendulum, which for the free response is trivially zero. It is included in eq (4.53) for completeness. The system of equations is solved for each pendulum section taking as initial conditions the initial pendulum angle and assuming the motion starts from rest. The comparison for the first section is seen in Figure 4.5.2, which indicates an important distinction in the damping definition. The ideal pendulum has been modelled assuming viscous damping in the rotational bearings suspending the pendulum axle, but the shape of the experimental decrement (linear rather than exponential) suggests that the dominant energy loss is due to Coulomb friction in the bearings. Given the difficulty of describing this effect within a linear system of equations, which is the intended state description, it is decided to estimate the Coulomb friction with a viscous damping and accept that there will be error in the estimate. However, the equivalent viscous damping can be chosen so that the damping is best described in the operating region of pendulum angle, from around 20° to 5° , that most of the control will take place in. This displaces the error so it will be less impactful.

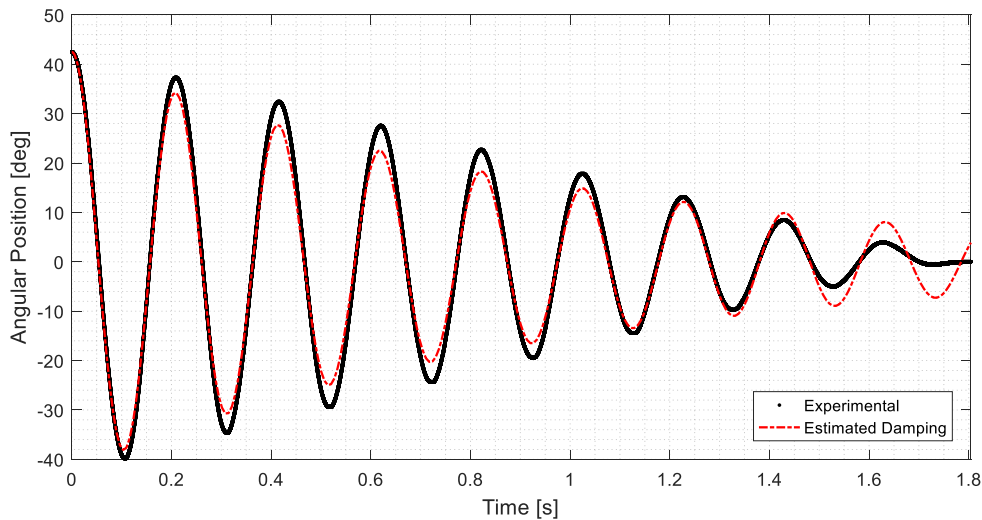


Figure 4.5.2 – Model comparison to experimental at 45° initial offset.

The chosen viscous damping coefficient which yields a good estimate in the operating region is a c_p of 1.3×10^{-4} (N·m·s/rad). To validate the choice the other pendulum runs of different initial angles are solved similarly, predicting the trajectory with the assumed damping (Figure 4.5.3). This supports the fit in the desired region, with an expected and unavoidable overestimation of the trajectory at lower angles. This is likely due to there being nonlinear and static effects that occur at low angular speeds which halt the pendulum motion. The disparity between the real behaviour and the damping prediction is not as consequential for the complete control system because the system has sensor feedback to adjust at small angles.

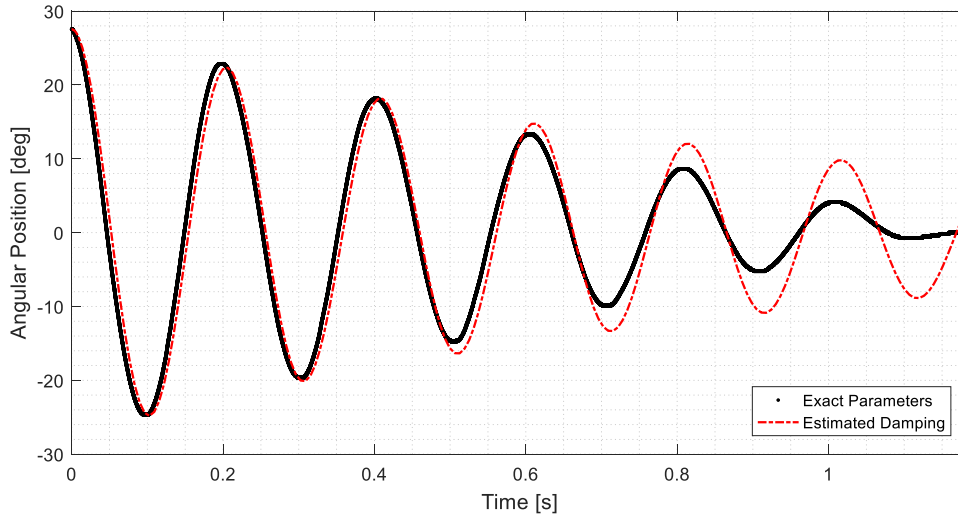


Figure 4.5.3 – Model comparison to experimental at 30° initial offset.

4.6 Model validation

A complete list of parameters used in the model is given in Table 4.6.1, with which the system can be simulated with a given voltage input to each motor.

Table 4.6.1 – Properties of pendulum test bank.

Characteristics	Property	Value
Environmental	g , gravitational acceleration [m/s^2]	9.81
	E , power supply voltage [V]	24.4
Pendulum	m_p , mass [kg]	0.0724
	l_p , distance fulcrum to center of mass [m]	0.0915
	J_p , mass moment of inertia [kg m^2]	6.6e-5
	c_p , pendulum viscous damping [N m s/rad]	1.5e-4
Carriage X	m_x , isolated mass [kg]	1.77
	c_x , estimated viscous damping [N s/m]	0.02
Carriage XY	m_{xy} , isolated mass [kg]	0.706
	c_y , estimated viscous damping [N s/m]	0.2
Transmission	m_{w1} , mass of pulley [kg]	0.024
	m_{w2} , mass of idler [kg]	0.045
	r_{w1} , radius of pulley [m]	0.0128
	r_{w2} , radius of idler [m]	0.015
	I_{w1} , mass moment of inertia of pulley [kg m^2]	2.0e-6
	I_{w2} , mass moment of inertia of idler [kg m^2]	5.5e-6
	L_x , distance between pulley centers, X [m]	0.67
	L_y , distance between pulley centers, Y [m]	0.60
	l_x , distance between idler centers in X [m]	0.0775
	l_y , distance between idler centers in Y [m]	0.544
	μ , coefficient of friction of linear guide [-]	0.5
	ρ , mass per unit length of belt [kg/m]	0.024
	η , belt mechanical efficiency [%]	83.7
g_x , transmission efficiency in X [-]	0.85	

	g_y , transmission efficiency in Y [-]	0.5
Motor 1	\hat{J}_1 , assumed mass moment of inertia [kg m ²]	5.1e-5
	\hat{R}_1 , line to line resistance [Ω]	0.0801
	\hat{L}_1 , terminal inductance [H]	0.0014
	$\hat{\beta}_1$, estimated coefficient of friction [Nms]	5.1e-6
	\hat{k}_{e1} , electric constant [Vs/rad]	0.1130
	\hat{k}_{t1} , torque constant [Nm/A]	0.0209
Motor 2	\hat{J}_2 , assumed mass moment of inertia [kg m ²]	5.1e-5
	\hat{R}_2 , line to line resistance [Ω]	0.0533
	\hat{L}_2 , terminal inductance [H]	1.0e-4
	$\hat{\beta}_2$, estimated coefficient of friction [Nms]	1.0e-5
	\hat{k}_{e2} , electric constant [Vs/rad]	0.1167
	\hat{k}_{t2} , torque constant [Nm/A]	0.08837

Because the motor parameters are estimated using a second-order motor model, the damping of the pendulum is been estimated from comparison with the nonlinear pendulum, and the real-time state space is built from a linearized pendulum and first-order motor model, it is valuable to confront these types of models against the experimental to see first how the model captures the actual behaviour of the test bank, and second, what information is lost through the model simplifications.

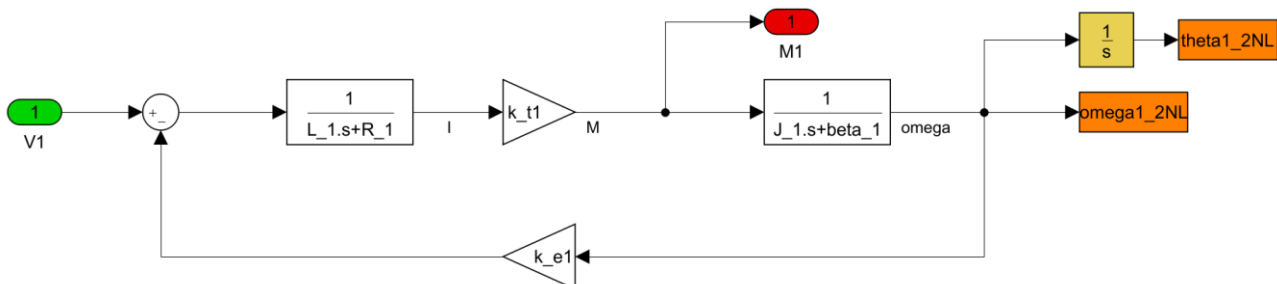


Figure 4.6.1 – Second-order motor transfer function.

Different models are built in Simulink[®], combining a second-or- first-order motor model with a linearized or nonlinear pendulum plant. The motor transfer function block diagram is given in Figure 4.6.1, while the order can be changed by applying the assumptions of eq. (4.13). The nonlinear carriage plant (Figure 4.6.2) represents the canonical equations of motion presented in eq. (4.21).

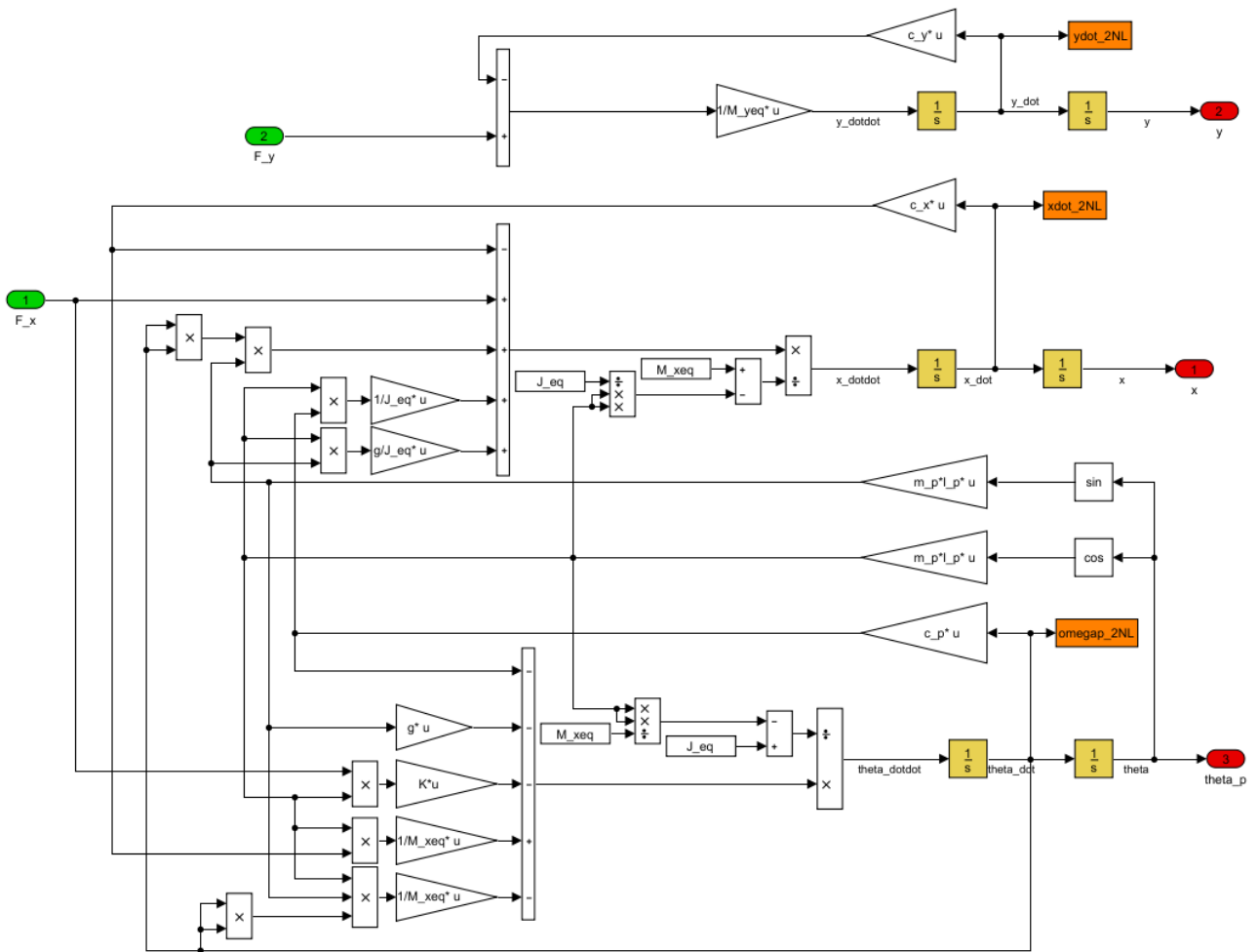


Figure 4.6.2 – Nonlinear carriage plant, block diagram.

Instead, for the linearized plant (Figure 4.6.3), the carriage plant has been linearized about the equilibrium point 0, since the test bank is run in a simple pendulum configuration for the first test.

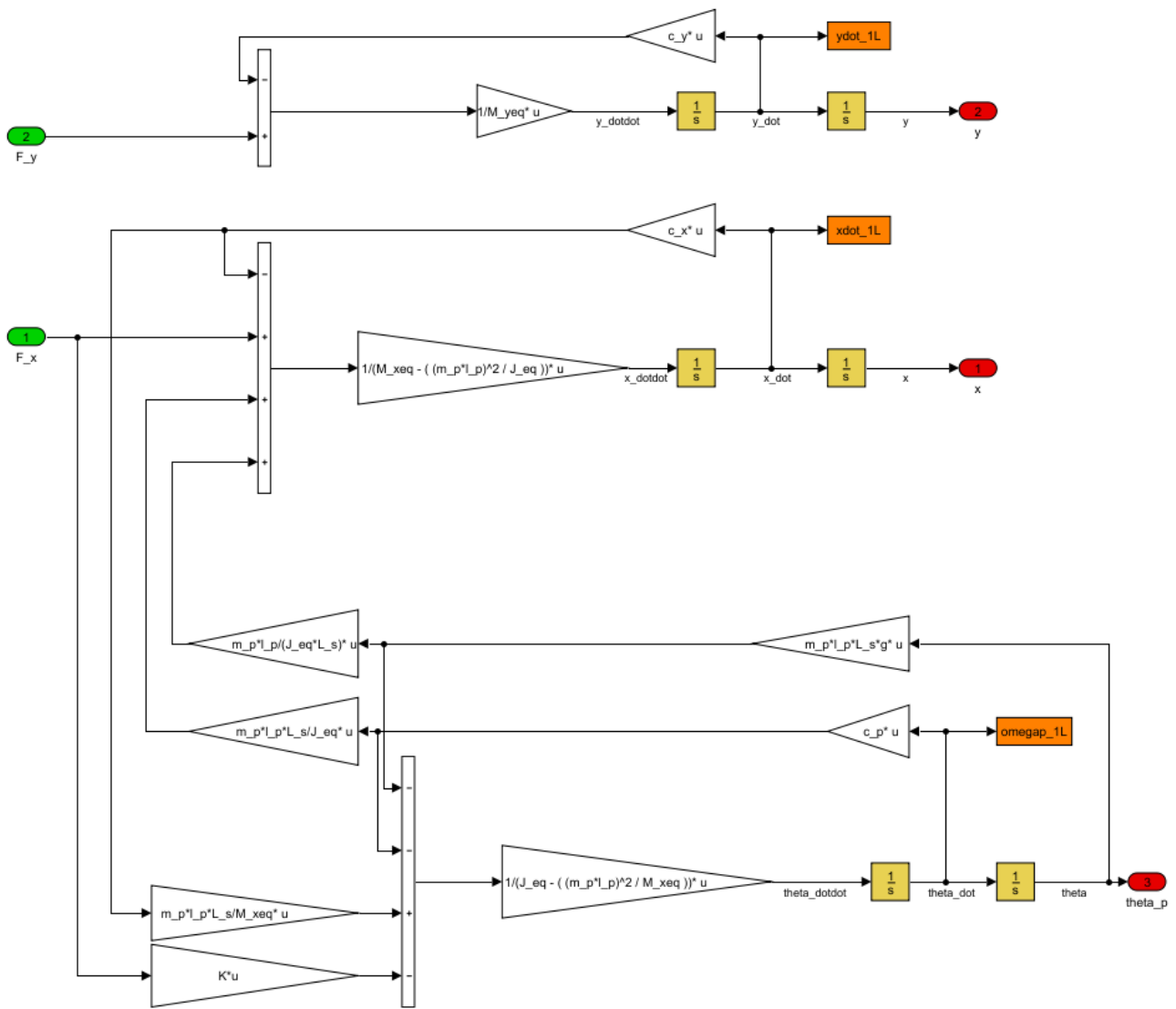


Figure 4.6.3 – Linearized carriage plant, block diagram.

The experimental system behaviour is captured by running the test bank through an open-loop programmed zeroing procedure with the limit switches manually triggered so that the carriage never makes an external contact. In this way the system response to an input voltage sequence is captured.

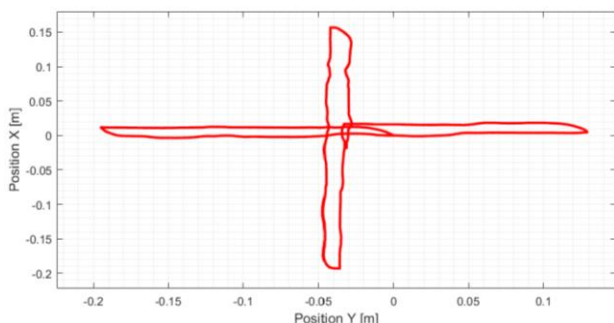


Figure 4.6.4 – Open-loop zeroing cart XY positions.

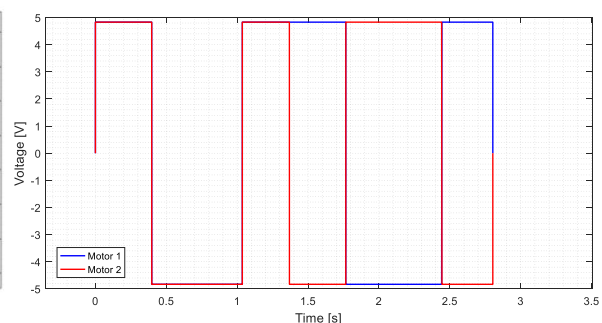


Figure 4.6.5 – Input motor voltages.

Using the voltage sequence in Figure 4.6.5, the system models of different order are simulated and compared to the experimental data, hereafter shown in black. The variables that are measured and compared are: the motor positions and speeds; the cart XY positions and speeds; the pendulum

angle. The comparison for the motor is critical for determining whether the parameter approximation of the motors is accurate, and the comparison of cart and pendulum position is critical because these are the system states. It is interesting to examine the responses of either motor because they have very different time constants (by an order of magnitude), and to examine the cart position in X and Y because the dynamics along the X-axis are affected by the pendulum inertia.

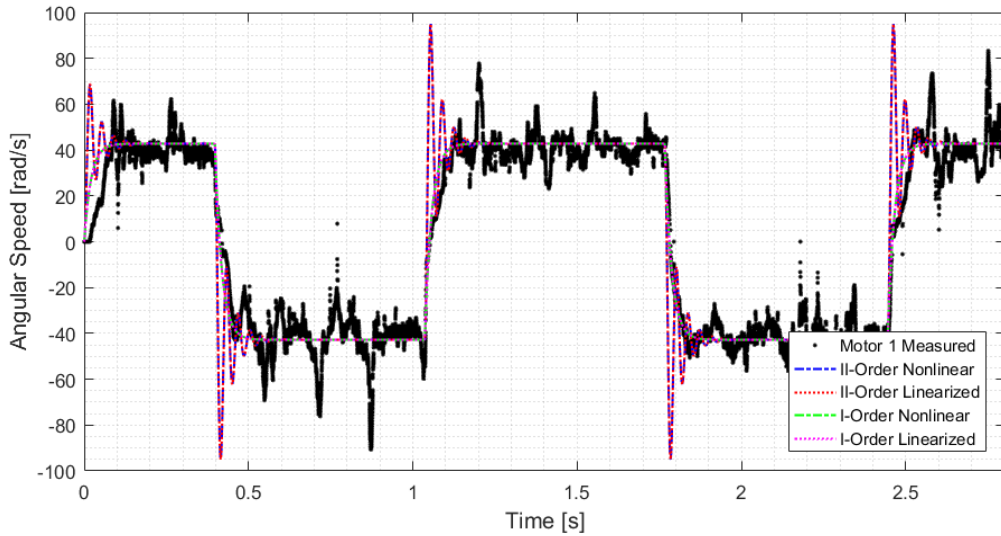


Figure 4.6.6 – Motor 1 speed compared to experimental.

Figure 4.6.6 shows the speed response of the first motor. The experimental motor appears to have an overdamped response, contrary to the response of the unloaded motor obtained during parameter estimation, which is underdamped, represented here by the second-order motor simulation. The loaded motor acts instead as an overdamped system; this behaviour is consistent with the assumption of eq. (4.15) which uses not just the motor rotor inertia but an effective inertia reflecting the loading on the motor. To this point, the first-order motor model (built from the estimated motor parameters), so long as it has the correct time constant for each motor, actually represents the motor dynamics better than the second-order. This is also seen in Figure 4.6.7 and Figure 4.6.8, where the motor positions are better tracked, though with some offset error from the transient regions, which indicates the trade-off of the order reduction.

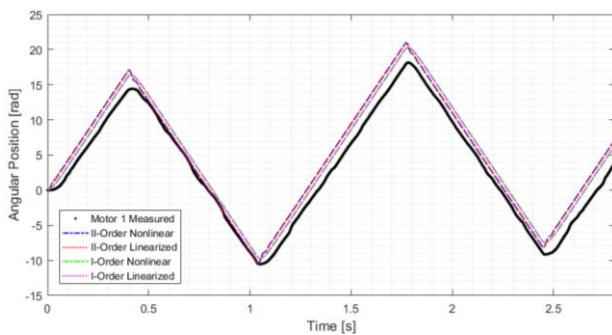


Figure 4.6.7 – Motor 1 experimental position.

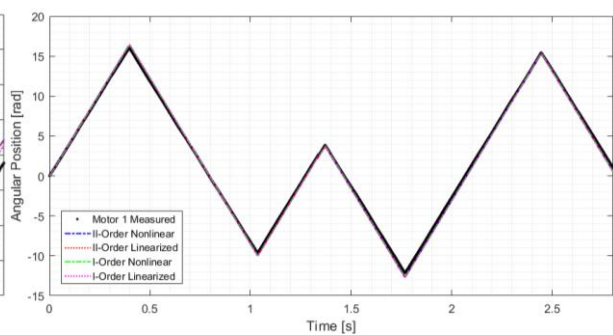


Figure 4.6.8 – Motor 2 experimental position.

The cart speed, shown in Figure 4.6.9 along the Y-axis, is reconstructed from the motor speeds, so exhibits the same dependence on the motor model order as the motors do: It is, however, still well estimated by either model.

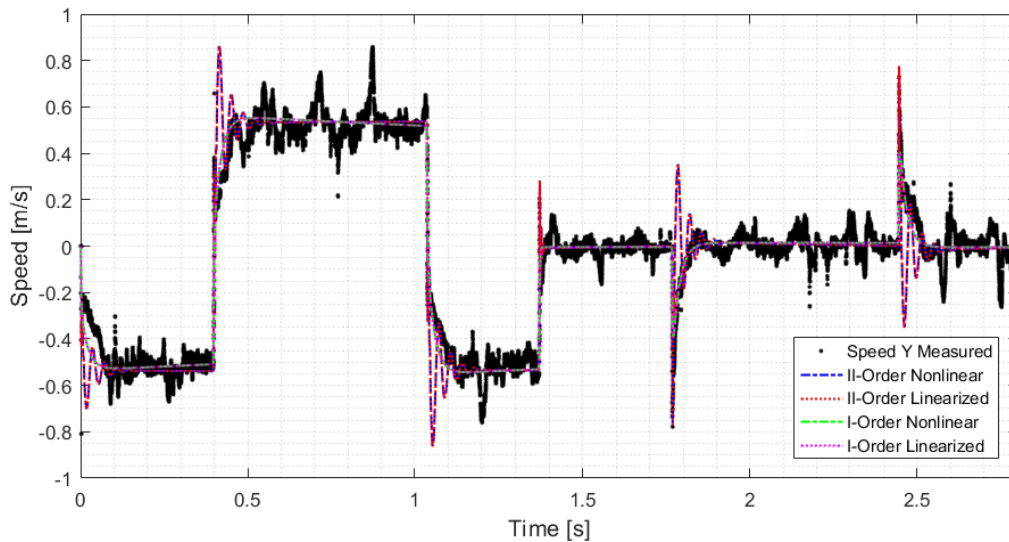


Figure 4.6.9 – Cart Y speed compared to experimental.

One of the principal motivations for the reformulation of the system model is that motion purely along the X-axis (a true planar pendulum) is infeasible because the motors have different time constants and by the single-belt H-bridge transmission, any single-axis movement is produced by the combination of motors. This means that the time constants of each motor are critical because whenever a change in direction is produced, there is a second, transient effect in the other direction. This can be seen in the positions in Figure 4.6.4, where a change in X-direction causes a jump along the Y-axis, and it can be seen in Figure 4.6.10. The zeroing procedure zeros first along the Y-axis, which is the first region of the figure, then along the X-axis, which in theory should be a null period, but the jumps in the position can be observed relating to changes in X direction.

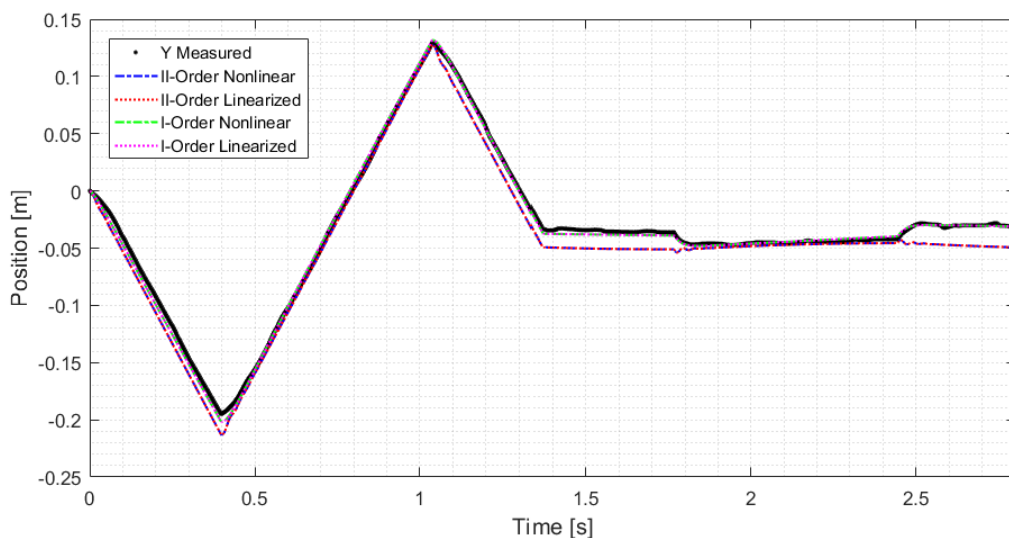


Figure 4.6.10 – Cart Y position compared to experimental.

Because the first-order motor model captures better the damping of the loaded motors, it is able to model this transience better than the second-order motor model. At this point the reduction of the motor order seems an acceptable assumption.

Second, the estimate of the pendulum position is addressed in Figure 4.6.11. The notable difference is that there is noise in the pendulum position unaccounted for by either the nonlinear or linearized model; this is likely due to system frictions or unmodelled carriage vibrations discussed in the

encoder estimation. It is important to capture the shape of the pendulum response with a reasonable estimate for the magnitude, as this is what the controller will need to predict. Though both models appear to give acceptable representations, it is clear that the nonlinear pendulum model better estimates the pendulum angle in both small-angle regions and at higher angles. However, the underestimation of the pendulum damping at lower angles by the linearized model is consistent with the assumptions during the estimation of the pendulum damping, where the damping value was chosen to better estimate the mid-angle regions and overestimate small-angles. In this way, the linearized behaviour is consistent with the compromise made during the parameter estimation, with a small but uncritical consequence.

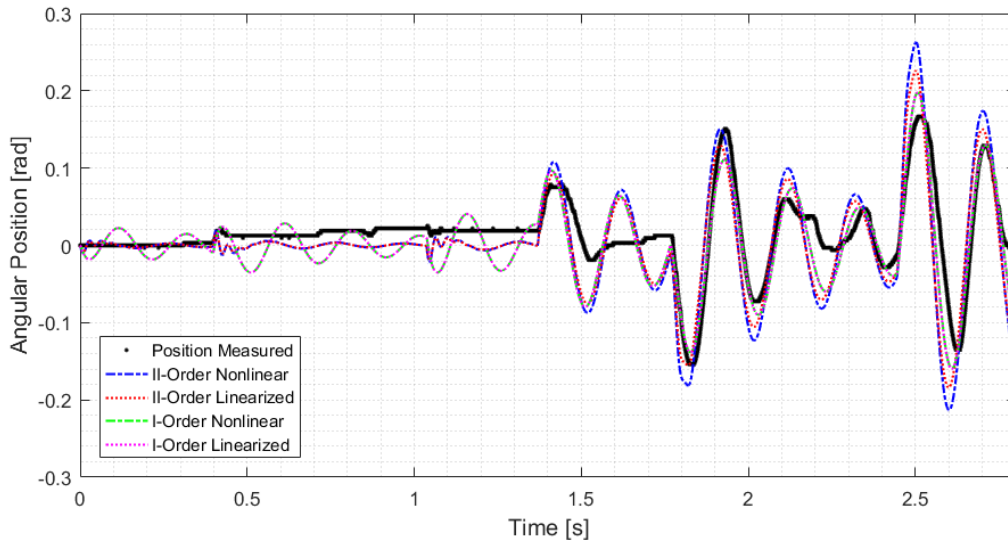


Figure 4.6.11 – Pendulum angle compared to experimental.

After determining that a first-order motor model and a linearized pendulum is an acceptable representation of the test rig, it is also necessary to verify that the equivalent state-space equations match the simulated block diagrams. This is not a guaranteed point because the motor model in Figure 4.6.1 has an internal speed feedback, which is eliminated the state space equations and replaced by a transformed feedback of the cart speeds; this can be seen in the transformation between eq. (4.18) and eq. (4.19). While the cart speeds are determined from the motor speeds, they are also affected by their own dynamics and the dynamics of the pendulum, which may lead to lost information or unexpected dynamical links.

This is the case, seen in Figure 4.6.12, where the simulated block diagram and simulated equations of the same system yield a slightly different motor position estimate.

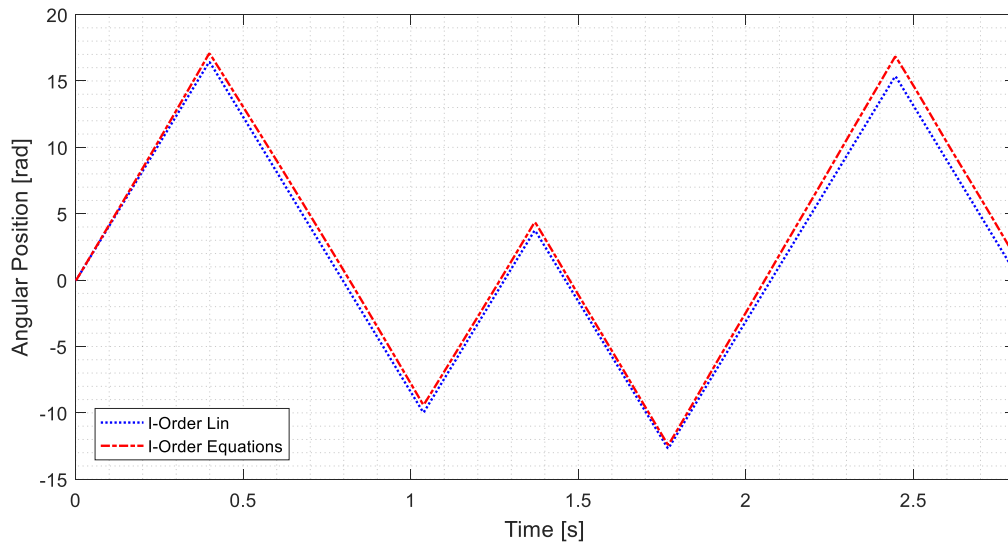


Figure 4.6.12 – Motor 1 position, comparison of linearized models.

While it is clear that there is some difference between the motor position estimates, the important determination is whether it changes the estimate of the states. In Figure 4.6.13, the cart X position, there is no significant affect of the estimate; the important transient and steady-state information is nearly the same.

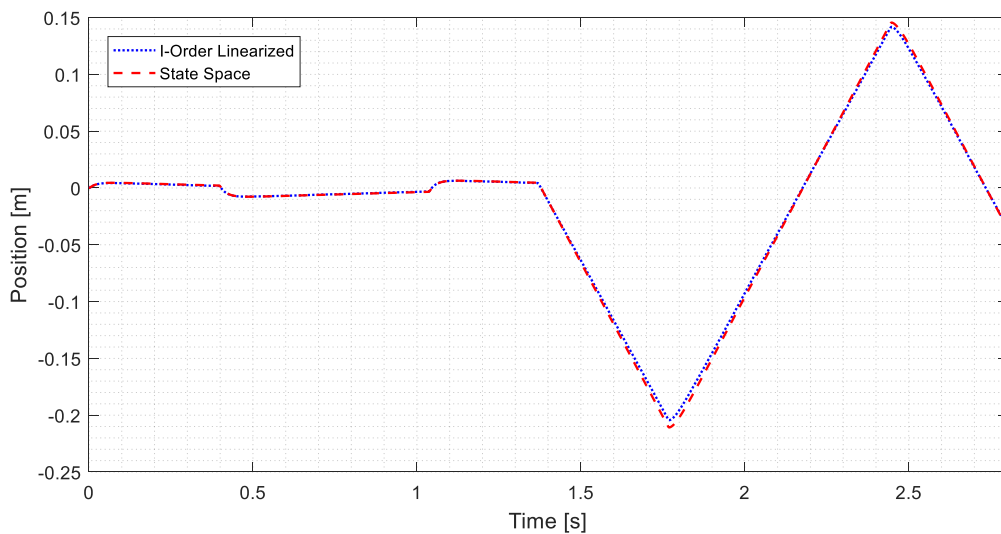


Figure 4.6.13 – Cart X position, comparison of linearized models.

In Figure 4.6.14, the cart speed in X, it can be better seen that some of the vibrations on the cart at steady-state are more damped in the state-space simulation. This is because the internal speed feedback of the motors, discussed above, effectively becomes a damping on the cart in X and Y, seen in eq. (4.19). This additional damping is also why the estimated coefficients of damping, c_x and c_y , can be approximated roughly based on the nominal bearing damping, since there are higher-magnitude damping terms at work in the equations.

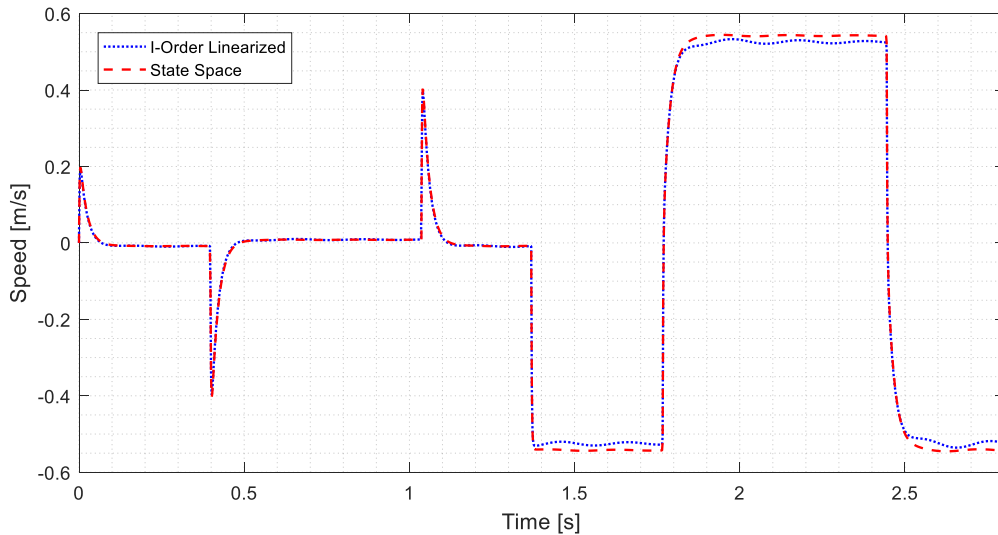


Figure 4.6.14 – Cart X speed, comparison of linearized models.

The modelling of the inverse pendulum is also validated by comparing to the open-loop behaviour. Because the open-loop system is unstable for the inverse case, only the initial unstable response of the system is measured; the pendulum is set at equilibrium about π , and then the cart is actuated in either the positive or negative X direction. The pendulum diverges from equilibrium until it contacts the carriage at the rotation limits and then rebounds with unmodelled dynamics. Since the dynamics of the motor-cart-transmission have been verified and are the same for both pendulum configurations, the aim of this comparison is to validate the modelled inverse pendulum response to powered motion of the cart. The experimental system is compared to the linearized pendulum as well as the nonlinearized plant to suggest the cost of approximation from linearization.

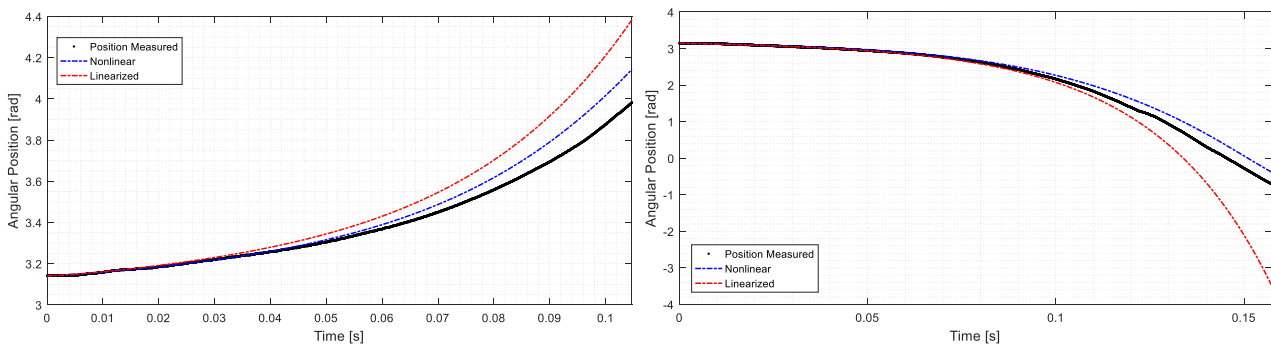


Figure 4.6.15 – Driven pendulum angle until contact at 225° (left) and driven pendulum angle until contact at -45° (right).

For carriage motion towards +X, the pendulum is thrust towards the top rotation limit, at 225° ; this can be seen in Figure 4.6.15 (left). For Figure 4.6.15 (right) the carriage is driven towards -X and the pendulum moves through the 0 equilibrium point until it contacts the bottom rotation limit at -45° . As expected, there is an angle-dependent error in the approximation, larger for the linearized model than for the nonlinear. However, as projected by the previous thesis work and the small angle approximation used when linearizing, the model is very close for angular deviations of less than 10° ($\Delta 0.175$ rad) and acceptably accurate under 25° ($\Delta 0.436$ rad). For the small-angle control actions of the LQR control, the accurate modelled range is sufficient.

4.7 Conclusions

The model for the pendulum test bank has been reformulated to reflect XY motion, the consequent change in model to MIMO, and experimentally tuned parameters. The most significant of these is the coefficient accounting for unmodelled losses of the carriage forces in X and Y due to mechanical construction sources discussed in Chapter 1; it is estimated that 15% of the action in X is lost and 50% in Y. This limitation on the yield is a significant consideration when designing control actions. The developed model has been compared to the experimental behaviour of the system to confirm that the assumptions of a first-order motor model and linearized pendulum give acceptable representations of the system in simple and inverted cases, as does the resulting state-space model.

5. Controller

Changing from a SIMO system to a MIMO system defined by two motors of different parameters and a cart with two position states, x and y , the chosen control method is linear quadratic regulation because of its tunability and accessibility of the control algorithm.

5.1 LQR controller

A linear quadratic regulator is a state feedback controller that minimizes a cost function in terms of states and inputs. The control law, here shown in its digital form, is the linear gain matrix of eq. (5.1) applied to the system states in negative feedback.

$$u_d = -\mathbf{K}_d z_d \quad (5.1)$$

The controller is optimal in that it minimizes the cost function with tuneable weights Q and R . For the pendulum test bank implemented in real time, digital infinite horizon LQR is used [10]. The digital cost function is given in eq. (5.2).

$$J = \sum_{k=0}^{\infty} (z_k^T Q z_k + u_k^T R u_k) \quad (5.2)$$

The feedback scheme is shown in Figure 5.1.1, where the digital controller is used because the real-time control is implemented via PXI (modular measurement and control platform) at a set loop rate of 40 kHz. A separate controller is created for either case, simple and inverse pendulum, using differently tuned state and direct input matrices. The response characteristics can be tuned by changing the square diagonal Q and R matrices, which are effectively weights on the individual states and inputs. A drawback of LQR is that constraints on states, such as physical limits, or input power saturation, cannot be directly accounted for by the algorithm and must instead be traced manually. Alternate control schemes like model predictive control allow for intrinsic constraint calculations but are computationally costly in real-time, contrasted to the simple control law of LQR.

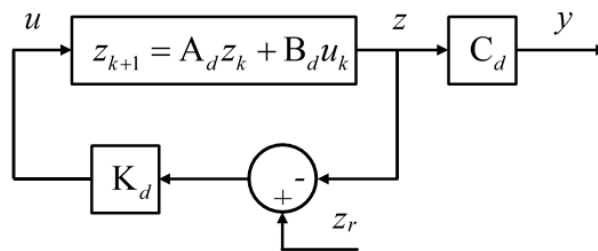


Figure 5.1.1 – Linear Quadratic Regulator in feedback with state reference.

5.2 Controller tuning and performance

The motivating factors for the controller design are pendulum angle regulation, stabilising the pendulum when inverted, and cart servo behaviour, all while not exceeding the input power limit and meeting performance targets set in the prior thesis work, listen in Table 5.2.1.

Table 5.2.1 – Control performance targets.

Property	Value
t_r , rise time [s]	≤ 0.5
t_s , settling time [s]	≤ 3.0
\hat{s} , overshoot [%]	≤ 30
e_{ss} , steady-state error [%]	≤ 5

Most of the indicators are relevant to the servo behaviour of the cart but can be estimated for the pendulum angle in regulation (null value steady-state). In the simple pendulum these parameters are not exceptionally demanding, but for the inverse pendulum much of the control action goes to stabilising the pendulum. There is a limit to the available input power; the maximum voltage suppliable is 24.4 V. These limits are not explicitly represented in the controller creation but are instead respected by post-tuning. They will be relevant when considering the experimentally observed limits on control action discussed in the previous chapter.

Beginning with the simple pendulum, a digital controller is generated using the command `lqr` in Matlab[®] and implemented with negative feedback and reference in simulation with the best model (nonlinear pendulum) of the total system to simulate the controlled performance. For the initial conditions, the only nonzero condition is an initial pendulum displacement of 25°, which is the limit of the desired controllable range. Tuning is performed through changing the diagonal values of the Q and R matrices. An increased weight depresses the value of the corresponding variable. The tuning targets are to meet the performance requirements and to keep the maximum input to either motor less than the maximum voltage suppliable. The system is not fully controllable, which is resolved by reducing the controlled states to four, weighting primarily the cart positions and pendulum angular position. The weights of the Q and R matrices are given in Table 5.2.2 with the reduction in control reflected in the null weight to the cart speeds.

Table 5.2.2 – Simple pendulum Q and R weighting.

Matrix	Coefficient	Value
Q	Q_{11} , speed x weight [-]	0
	Q_{22} , speed y weight [-]	0
	Q_{33} , pendulum angular speed weight [-]	1
	Q_{44} , position x weight [-]	2500
	Q_{55} , position y weight [-]	2500
	Q_{66} , pendulum angular position weight [-]	3000
R	R_{11} , motor 1 voltage weight [-]	1
	R_{22} , motor 2 voltage weight [-]	1

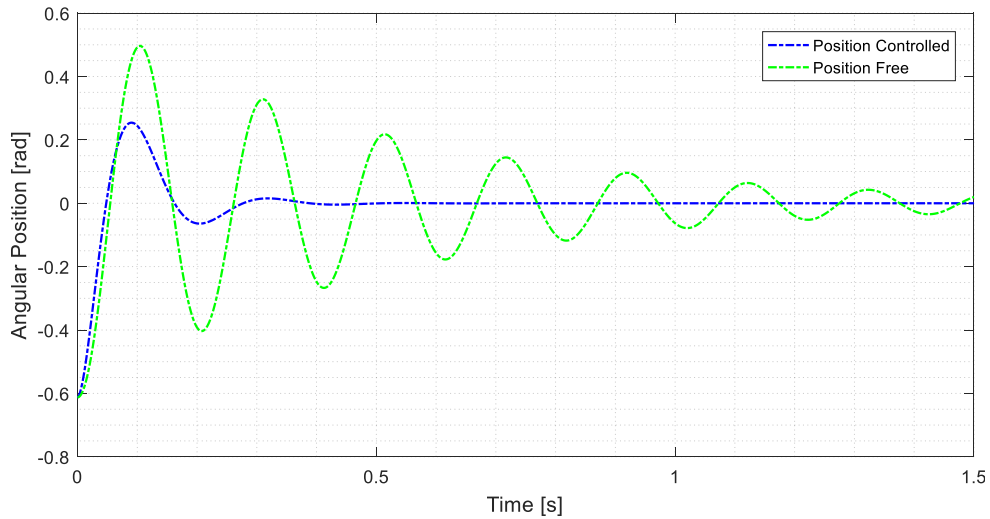


Figure 5.2.1 – Controlled pendulum regulation.

The effect of the LQR feedback control on the pendulum can be seen in Figure 5.2.1 compared to the free oscillations of the pendulum. It should be noted that the pendulum control is significantly faster than the performance requirements of Table 5.2.1; feedback makes the frequency of the pendulum angle naturally faster than the performance requirements, so tuning serves primarily to bring the response time of the cart position into target. Figure 5.2.2 shows the projected cart response, which is slower to reach steady-state. The primary movement is in the X direction, which is an intentional choice because carriage movement in the Y direction is notably more difficult due to the discussed greater resistance and vibrations, and reducing Y movement is a practical consideration to maximize control action and minimize loss of sensor fidelity from cumulative error in position sensing of the incremental encoders.

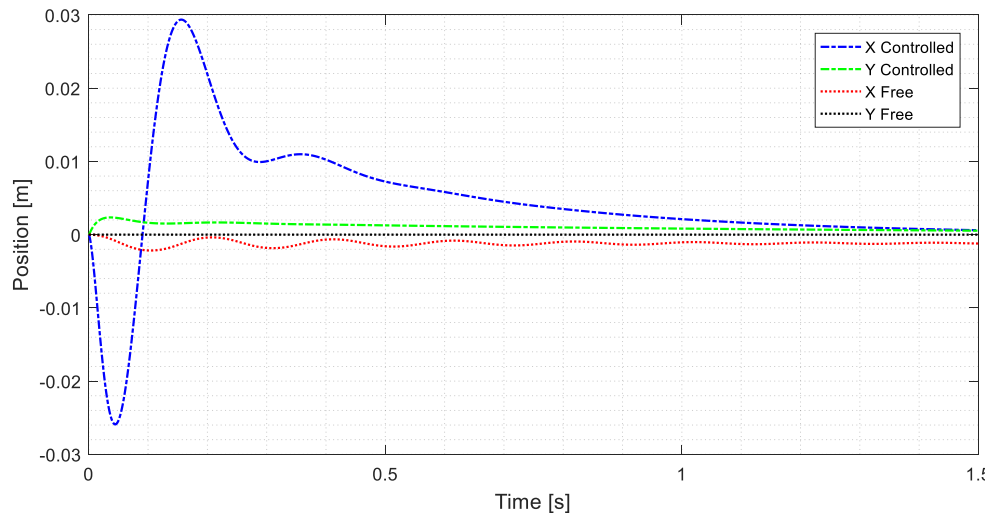


Figure 5.2.2 – Controlled cart regulation.

The effect of the feedback on the system stability is studied through the eigenvalues of both the open-loop and closed-loop plants, listed in Table 5.2.3. Stability is studied in open-loop through eq. (5.3), the eigenvalues of the matrix A (defined previously in eq. (4.37)).

$$\{\lambda\} = eig(A) \quad (5.3)$$

In feedback, the digital LQR controller K_d changes the closed-loop transfer function; stability is studied through the loop matrix of eq. (5.4).

$$\{\lambda\} = \text{eig}(A - BK_d) \quad (5.4)$$

Stability is determined by studying the real part of the eigenvalues. While the simple configuration is asymptotically stable, the inclusion of the cart dynamics makes the system marginally stable, seen in the repeated real roots of the cart speeds. This repeated null value indicates singularity in A , which corroborates the non-full controllability of the system. In feedback this singularity is resolved, and the system is fully stable, with all negative real parts of the eigenvalues.

Table 5.2.3 – Simple pendulum eigenvalue comparison.

Simple Pendulum		Value	
Eigenvalue	State	Open Loop	Closed-Loop
λ_1	dx/dt , speed x [m/s]	0	-621.9
λ_2	dy/dt , speed y [m/s]	0	-44.70
λ_3	$d\theta/dt$, pendulum angular speed [rad/s]	-622.2	$-13.45 + j28.77$
λ_4	x , position x [m]	$-2.05 + j30.92$	$-13.45 - j28.77$
λ_5	y , position y [m]	$-2.05 - j30.92$	-4.06
λ_6	θ , pendulum angular position [rad]	-47.42	-3.91

The controller is implemented in the test rig and its performance is addressed. In Figure 5.2.3 the controlled pendulum angle response to a disturbance is compared to the simulated controller. The excitations are not exactly equal, since the simulated control responds to an offset alone, and the real excitation is closer to an impulse with non-zero speed components.

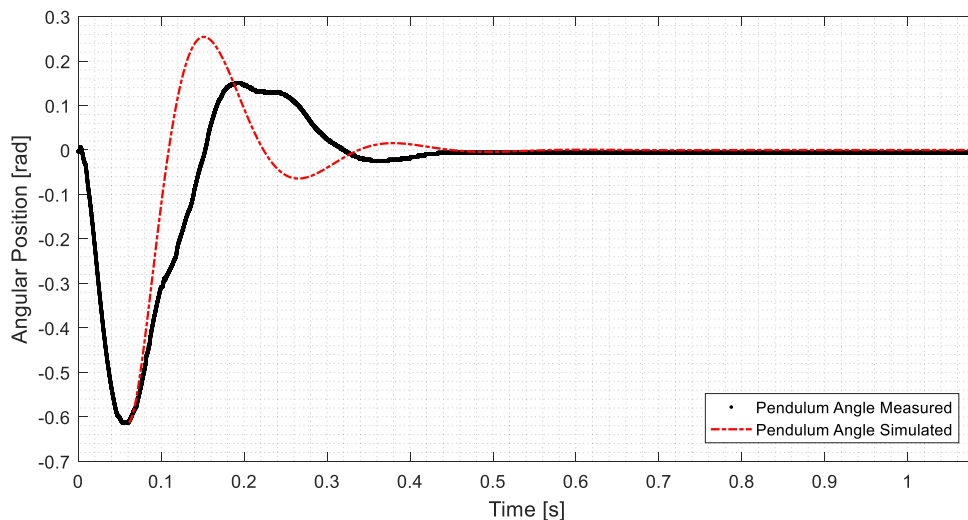


Figure 5.2.3 – Experimental simple pendulum regulation.

The controlled system regulates the pendulum angle as designed; the largest discrepancy is that the real system appears to have greater damping at decreasing displacement, which is consistent with the assumptions made when estimating the pendulum damping around small angles.

Figure 5.2.4 gives the X position of the cart in the control, which indicates that the magnitude of the cart displacement is greater experimentally than predicted by the simulated control. An obstacle to the cart regulation is that static attrition in the transmission system results in small, non-zero

voltages having null motion on the cart. Tapering voltages to the cart past these small voltage thresholds eventually lead to steady-state errors in cart position.

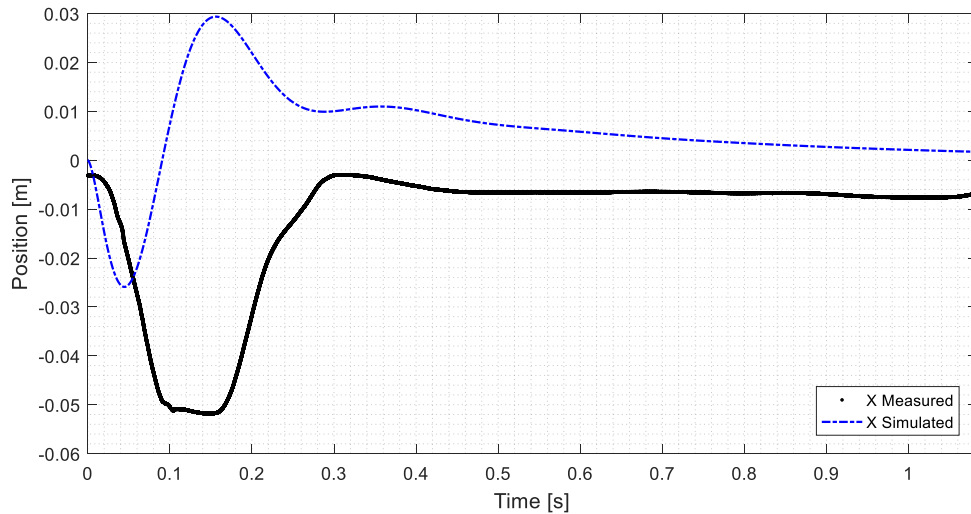


Figure 5.2.4 – Experimental cart regulation, simple pendulum.

Control of the inverse pendulum is affected by the discussed control action limitations, which are present but not insurmountable in the simple pendulum. A digital controller is created as before, with differently tuned Q and R matrices. While respecting the limits of controllability, a priority is on limiting control actions that displace in the Y direction to reduce vibrations.

Table 5.2.4 – Inverse pendulum Q and R weighting.

Matrix	Coefficient	Value
Q	Q_{11} , speed x weight [-]	0
	Q_{22} , speed y weight [-]	1250
	Q_{33} , pendulum angular speed weight [-]	0
	Q_{44} , position x weight [-]	2500
	Q_{55} , position y weight [-]	500
	Q_{66} , pendulum angular position weight [-]	2500
R	R_{11} , motor 1 voltage weight [-]	1
	R_{22} , motor 2 voltage weight [-]	1

The predicted control action stabilises the inverse pendulum, with the simulated control response shown in Figure 5.2.5 and in closer detail with Figure 5.2.6. The pendulum returns to the unstable equilibrium point instead of returning to ground as the free pendulum, in blue, does. The obstacle suggested above is the limited power supply to the motors. Much of the control action goes only to losses and stabilising the pendulum, leaving little for regulation or servo setting of the cart. Because of this the simulated control is for a very small initial offset angle; there is a small window of $\pm 5^\circ$ about the unstable equilibrium where the requested input voltage is feasible.

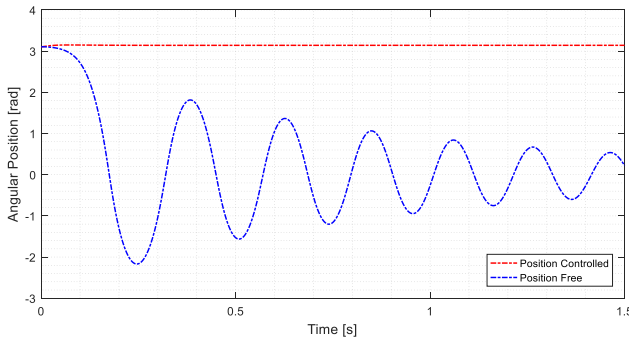


Figure 5.2.5 – Simulated inverse regulation.

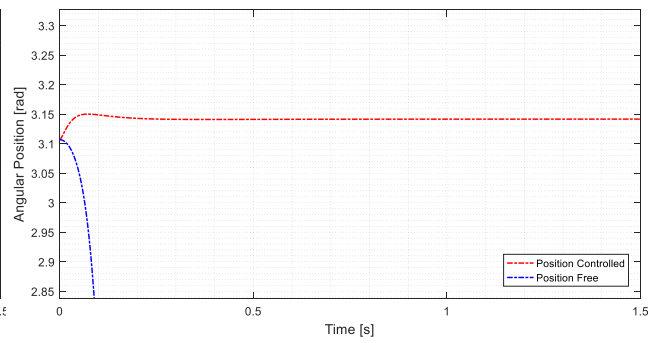


Figure 5.2.6 – Controlled stable response.

This significant limitation effectively means that despite the controller simulation, regulation of the cart position is challenged. An additional complication is that the vibrations inherent to cart position creep or erratic movements along Y can easily push the pendulum angle out of the narrow controllable window, so reducing Y movement in the control is a high priority; this is the motive for the high weights on the state y in Table 5.2.4. The compromise can be seen in the simulated cart position response of Figure 5.2.7, where the cart displacement in Y is minimized.

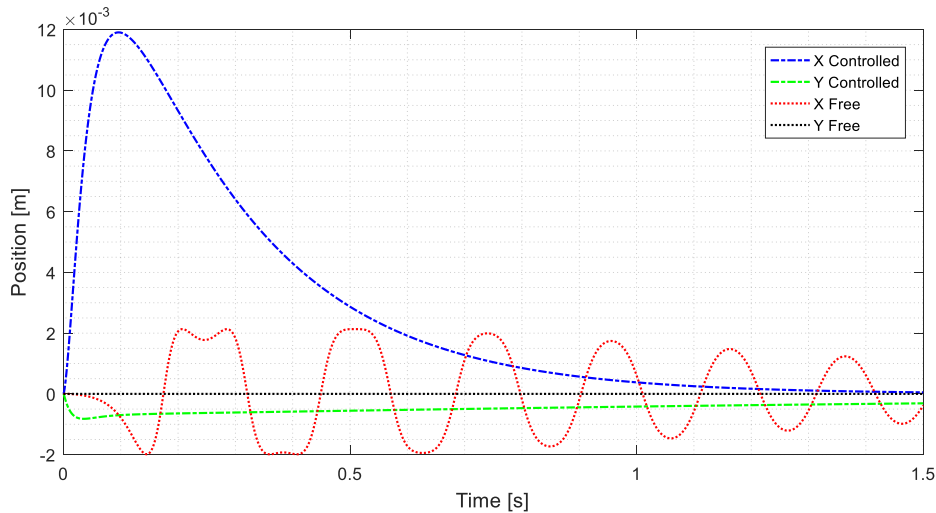


Figure 5.2.7 – Controlled cart regulation, inverse pendulum.

The effect of feedback on the inverse pendulum system is more important because the open-loop bank is initially unstable: see λ_3 in Table 5.2.5. After controller feedback, the eigenvalues are all stable, though the proximity λ_6 (the eigenvalue associated to the pendulum angle) to the origin indicates the small margin of stability.

Table 5.2.5 – Inverse pendulum eigenvalue comparison.

Inverted Pendulum		Value	
Eigenvalue	State	Open Loop	Closed-Loop
λ_1	dx/dt , speed x [m/s]	0	-1358
λ_2	dy/dt , speed y [m/s]	0	$-56.35 + j12.34$
λ_3	$d\theta/dt$, pendulum angular speed [rad/s]	31.96	$-56.35 - j12.34$
λ_4	x , position x [m]	-34.51	-21.34
λ_5	y , position y [m]	-47.63	-3.99
λ_6	θ , pendulum angular position [rad]	-628.0	-0.60

In practice, this small control margin means that the pendulum angle never fully stabilises and dances about equilibrium, shown in Figure 5.2.8. There is no definable stabilising response, but rather a bounded stability at the cusp of becoming unstable. The reason for this is likely because in addition to centring the pendulum about the unstable equilibrium, the control is also trying to centre the cart about the origin, dynamically linked actions that the system does not have enough input power supply to resolve. This is evidenced with the cart position response in Figure 5.2.9, where the prioritised Y-centring occurs with some bounded error, but there is no discernible regulation in X. It can be concluded that the lack of power supply coupled with the null-transmission at small input voltages leads to an extremely limited range of stabilising control actions near equilibrium, explaining the marginal stability of the pendulum angle and default in cart regulation behaviour.

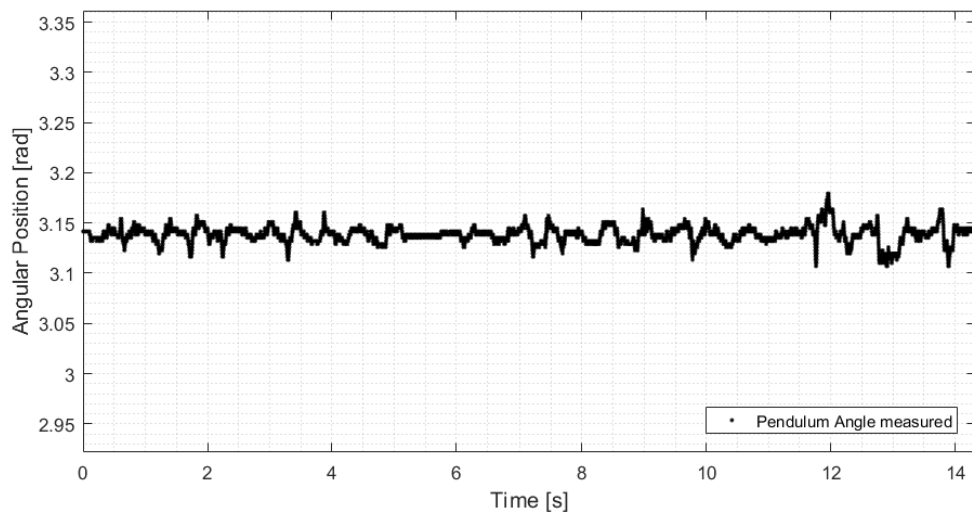


Figure 5.2.8 – Experimental inverse pendulum controller performance.

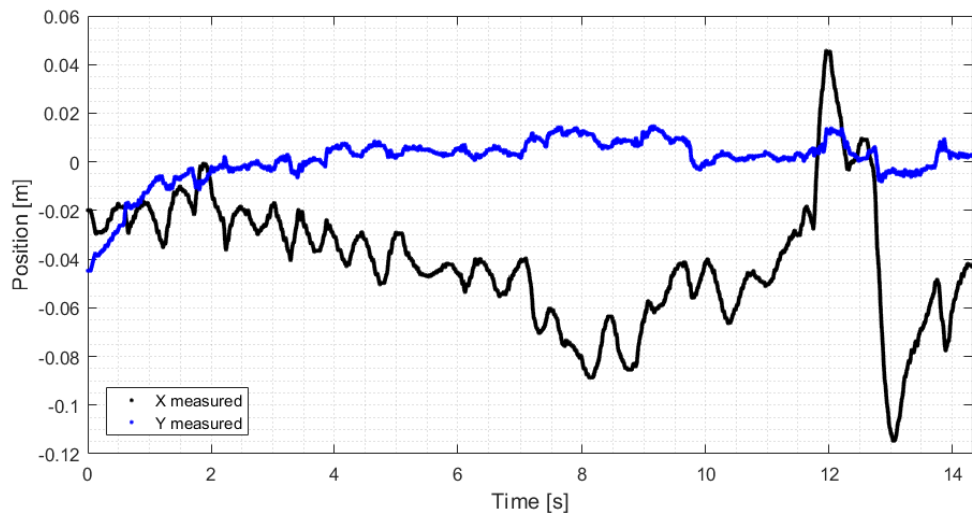


Figure 5.2.9 – Controlled cart response, inverse pendulum.

5.3 Conclusions

When fabricating the pendulum, the first flexural mode was modelled to avoid resonance with the controlled frequency of the pendulum. The natural frequency of the simple controlled pendulum

angle is near 4 rad/s and the controlled inverse pendulum has a natural frequency below 1 rad/s. The first flexural frequency to avoid is 917.5 rad/s, so there is no risk of resonance due to flexing. Through digital LQR control regulation of the simple pendulum and limited servo behaviour of the cart is achievable. Zero steady-state error in cart position is infeasible due to null cart responses from small non-zero voltage inputs, primarily from cumulative static frictions. Stabilisation of the inverse pendulum is achieved with narrow margins. The compromises to achieve stability result in feasible regulation in Y and none in X, with no outcome for inverted pendulum servo behaviour. A primary obstacle is limited control potential from pairing the motors, which are rated for 50 V and 8 A, with an undersized power supply, which can provide at maximum 24 V and 4 A to either motor.

6. Real-time control

System sensing and control is implemented through a real-time measurement and control platform National Instruments® PXI 6229 and NI VeriStand® software environment. There are additional systems effected beyond control: background logic in the real-time model is programmed for cart position reconstruction, zeroing, locating the carriage within its inherent mechanical limits and preventing any actions which overstep those bounds, damaging the system or interrupting control. To this end, the real-time model is equipped with a togglable zeroing procedure for defining limits and limit detection on the carriage position.

6.1 Systems hierarchy map

The real-time model takes sensor information as input and has as output the voltage sent to the motors. The sensor information is primarily angular positions read by the system encoders, which are turned into the system states: cart linear position and speed, and pendulum angular position and speed. Figure 6.1.1 maps the system functions and the information they share with each other. The speed estimator has been discussed in Chapter 3, and the controller in Chapter 5.

A critical detail of the hierarchy is that both the limits and saturation block and the zeroing block can send voltage to the motors (instead of the controller). The limits and saturation block has an override on the motor voltage, so it can halt any control actions that risk exceeding the system limits; this block is constantly active in the background during control activity. The zeroing block has motor voltage override to set a prescribed carriage movement during zeroing. This function is only active when zeroing is toggled from the real-time GUI.

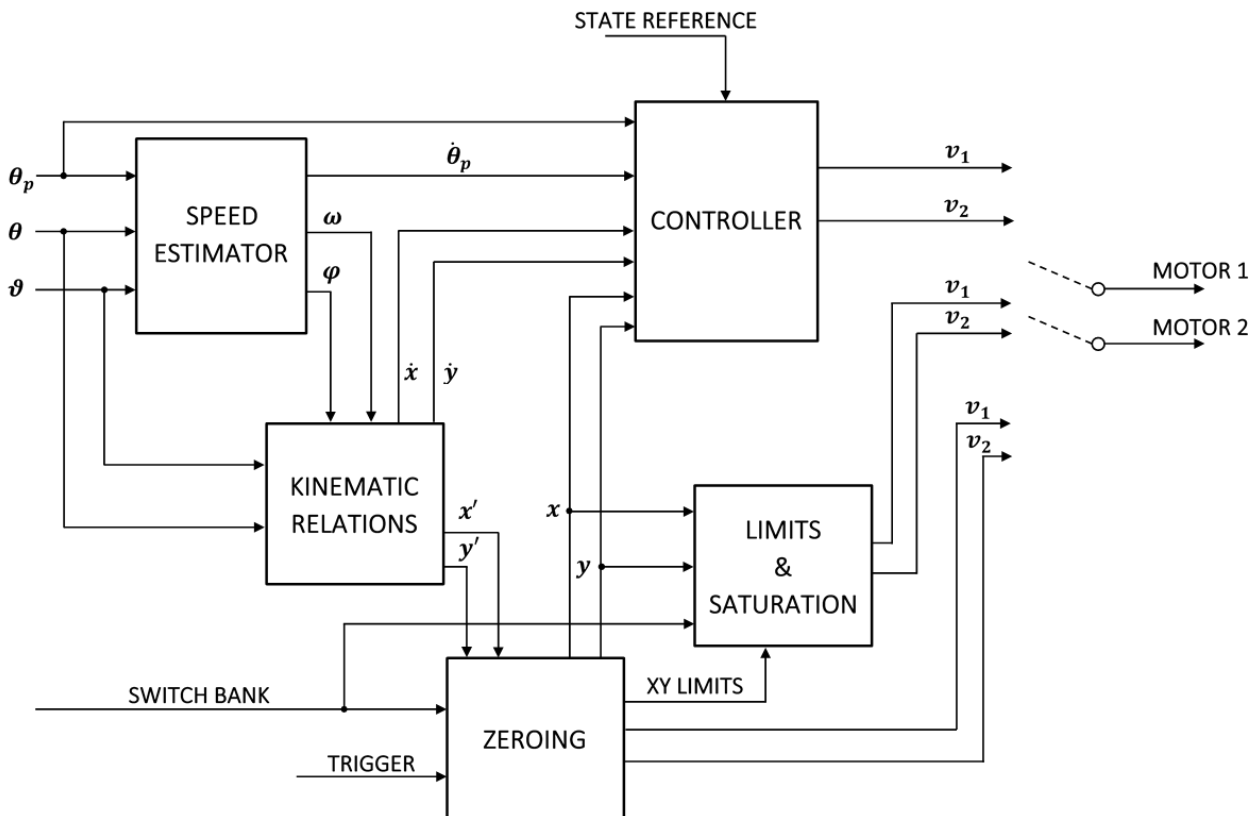


Figure 6.1.1 –Background systems map.

6.2 Kinematic relations and position reconstruction

The state of the system depends on knowing the carriage position and speed along both X-and-Y-axes. Since these states are not directly measured, it is necessary to estimate them from the angular position and speed of the motors. The kinematic relation between the cart and motor positions is defined in a translated coordinate system by assuming direct transmission by the belt.

$$\begin{aligned}\theta &= \frac{-y' - x'}{r_{wl}} \\ \vartheta &= \frac{-y' + x'}{r_{wl}}\end{aligned}\tag{6.1}$$

With the following representations:

- θ, ϑ : angular position of motors 1 and 2;
- x', y' : absolute (non-zeroed) coordinates of the carriage;
- r_{wl} : radius of the belt pulleys.

The relation can be rearranged to find x and y from the motor angular positions and derived with respect to time to find the carriage speeds:

$$\begin{aligned}x' &= +\frac{1}{2}r_{wl}(\theta - \vartheta) \\ y' &= -\frac{1}{2}r_{wl}(\theta + \vartheta)\end{aligned}\tag{6.2}$$

6.3 Zeroing

When the test rig is active, it has no initial indication of where in the XY plane the carriage is located; furthermore, the calculated x-and-y positions are not given in the reference frame centred on the test rig. It is necessary to translate the cartesian coordinates to the correct reference frame and to locate the physical limits of the system. For this, limit switches are placed at the extremes of each X-and-Y-axis. An initial zeroing procedure is carried out, which drives the motors to identify the position of the axis limits and then calculate the length of each axis. This length can also be found *a priori* since the mechanical structure is well-defined.

The zeroing and centring procedure follows the logic:

- turn motors for -Y until finding Y_{\min} (limit switch is triggered);
- turn motors for +Y until finding Y_{\max} (limit switch is triggered);
- centre carriage on Y;
- zero the Y-axis at centre Y;
- turn motors for -Y until finding Y_{\min} (limit switch is triggered);
- turn motors for +Y until finding Y_{\max} (limit switch is triggered);
- centre carriage on Y;
- zero the Y-axis at centre Y.

After zeroing, the XY origin is at the centre of the test rig, and the physical limits are stored in the model. The real-time model in NI VeriStand® stores the limit information until the test rig is re-centred from a command button in the GUI. Additionally, the GUI constantly displays the XY carriage position on a 2D display to simplify and visualize the carriage trajectory.

While x' and y' are the carriage positions derived from the motor angular positions, x and y are the transformed (zeroed) positions in the test bank reference frame: these are the positions used for the system states.

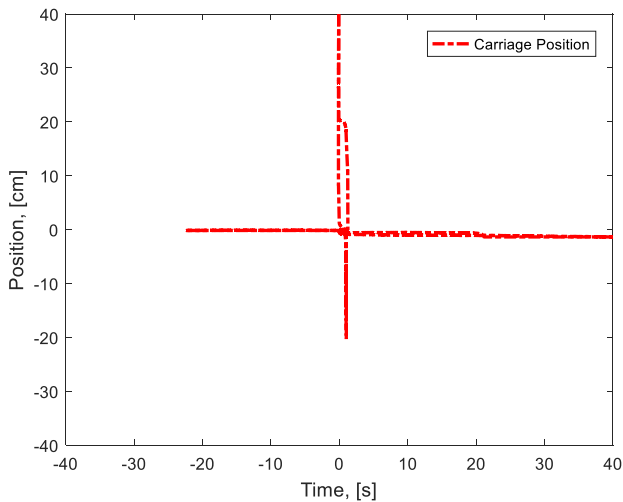


Figure 6.3.1 – Zeroing trajectory, XY plane.

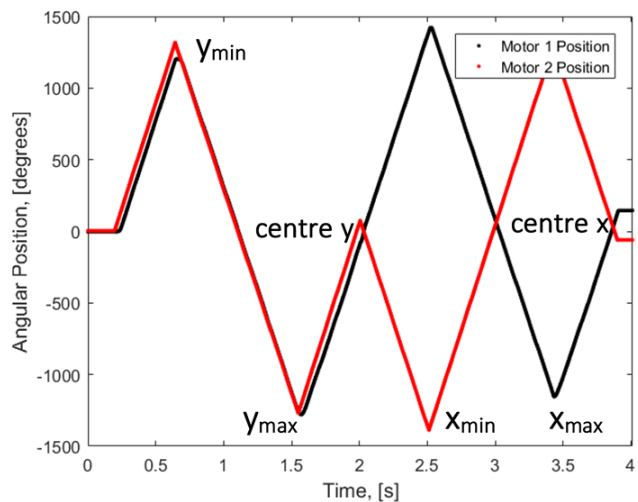


Figure 6.3.2 – Motor positions during zeroing.

The zeroing procedure is shown in Figure 6.3.1, where the cart tracks the X-and-Y-axes to find the limits. There are two features of note: the first is that the track length on the positive axes is twice the length on the negative axes. This is because the negative axis limit is found first, and then the positive axis limit. Once the positive axis limit is found, the length of the axis is calculated and the zero for that axis is recalculated at the centre of the rig. Because of this change of reference frame, there is an apparent jump in the carriage position. The second detail is that the motor actions, despite being sent input voltages of equal magnitude, are not exactly equal. In practice this means that the carriage drifts laterally when travelling along a single axis, which can also be seen in Figure 6.3.1. This repercussion of this two-axis dependency is precisely the reason for XY control of the cart and the consequent MIMO system.

Due to the unknown starting angle of the pendulum, an additional zeroing is performed on the pendulum to define the angle and equilibrium points of the pendulum. Vibrations during operation can also cause positional drift in the incremental encoder. With the narrow operating window of the inverse control, this can be a severe obstacle, so there should be a way to actively tare the pendulum angle. The pendulum has a range of motion of 270° on the cart, with a high and low stop point. Since the angles for these stop points are known and the distances from these to the simple and inverted equilibrium points are also defined, a simple zeroing finds these limits and sets the equilibrium positions.

The pendulum zeroing procedure follows:

- turn pendulum until it contacts the lower angle limit (-45°);
- after two seconds mark the angle;
- turn pendulum until it contacts the upper angle limit ($+225^\circ$);
- after two seconds mark the angle;
- calculate the stable and unstable equilibrium points from known geometry.

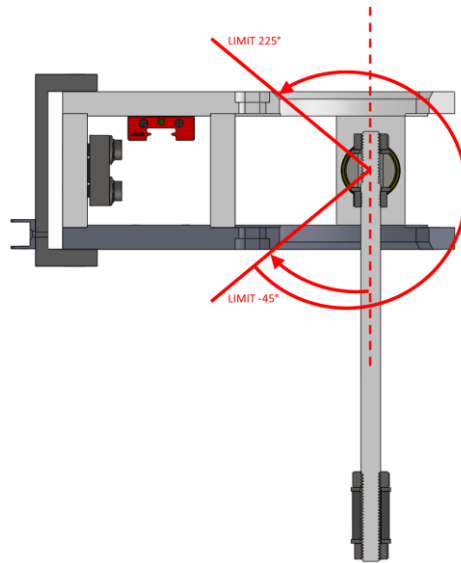


Figure 6.3.3 – Pendulum angular limits and zeroing.

6.4 Soft limits and saturation

Once the mechanical limits have been found, there should be a margin of safety to prevent the carriage from exceeding them. These margins are set based on the limits found in the zeroing procedure and the known contact points of the system. The limits on the X-axis and Y-axis (Figure 6.4.1 and Figure 6.4.2) can be combined to form an envelope that the carriage cannot physically exceed (Figure 6.4.3). Further, a soft limit envelope can be imposed: a region approaching the hard limit where the carriage should be halted before it risks contacting the test bank frame. If the carriage comes within a set percentage of the axis length (set to 5%) of any X-or-Y limit, this triggers a saturation that allows no further actions that cause a displacement in that axis direction.

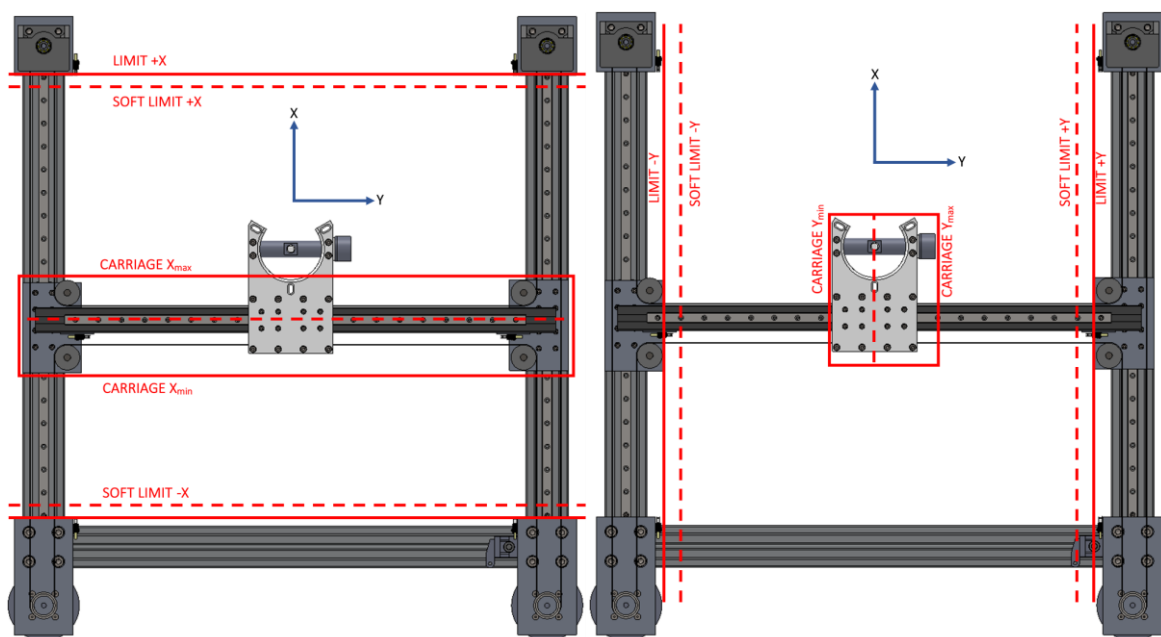


Figure 6.4.1 – X-axis limits.

Figure 6.4.2 – Y-axis limits.

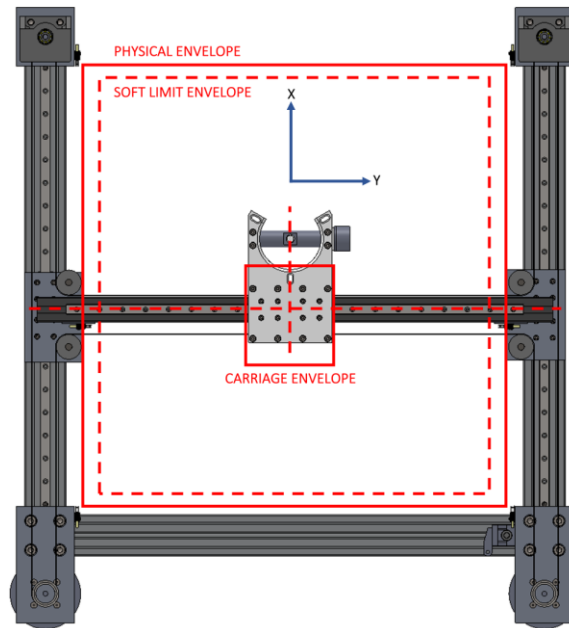


Figure 6.4.3 – Operation and soft limit envelopes.

Critically, the limit saturation only prevents carriage actions which will violate the axis constraint but allows movements of the carriage that return it to the operation envelope. This is possible because the test bank kinematics define which motor direction combinations produce specific movements in the axis directions (Table 6.4.1). Since these are known, if an axis condition is violated (such as the soft limit of +Y), logic conditions in the saturation block can still pass allowed movements (those that do not produce +Y) based on the input motor directions.

Table 6.4.1 – Motor-driven displacement map.

Motor Rotation		Carriage Displacement	
Motor 1	Motor 2	X	Y
Clockwise	Clockwise	0	-
Clockwise	-	-	-
Clockwise	Counterclockwise	-	0
-	Clockwise	+	-
-	Counterclockwise	-	+
Counterclockwise	Clockwise	+	0
Counterclockwise	-	+	+
Counterclockwise	Counterclockwise	0	+

Table 6.4.2 – Cartesian XY-driven displacement map.

Direction	Motor Rotation Combination	
	Motor 1	Motor 2
-y	Clockwise 0	Clockwise 0
+y	Counterclockwise 0	Counterclockwise 0
-x	Clockwise 0	Counterclockwise 0
+x	Counterclockwise 0	Clockwise 0

When the soft limit condition is met for a specific limit, the logic prohibits the combination of motor rotations which violate the limit, but still permits all other motor rotations so that the carriage can exit the limit.

These limits and saturations operate as background to the control scheme, providing important information, such as X and Y location in the zeroed reference frame, and preventing the system from running into limit conditions and being damaged or causing unsafe conditions.

6.5 VeriStand® environment and user GUI

The controller and background systems are first defined as a Simulink® model and then executed through NI VeriStand®, a real-time input/output stimulus program operating on the PXI platform. This model directs all sensing inputs, actuator outputs, and other user-initiated triggers. The user interacts with the program through a GUI which allows the selection of control behaviours, data logging, and display of the states. The GUI is programmable to give the user control over the type of control of the pendulum, to visualize the behaviour of the states, and to allow them to change some system parameters. The test bank configuration is shown in Figure 6.5.1.

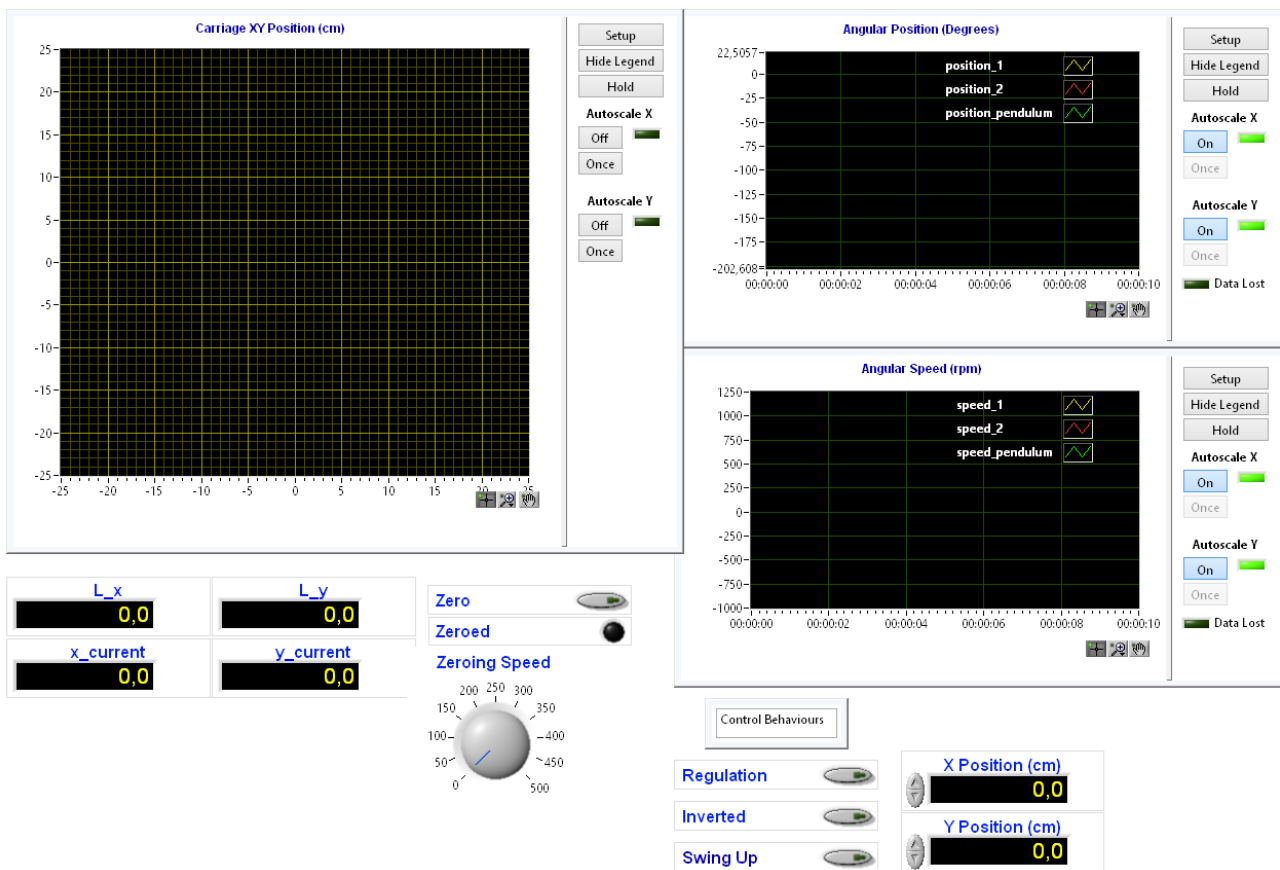


Figure 6.5.1 – NI VeriStand® GUI.

The user can select the type of control behaviour (currently these are placeholders, not connected to anything) or signal the system to zero the carriage. They also have control over the speed at which the carriage zeros, though it is not recommended to zero at a speed above 150 rpm as the accuracy of the axis lengths decreases at higher speeds. This is because the limit switches have a small delay in detection, and some movement is lost before the switch flips. With a faster carriage speed, more movement is lost.

The GUI has several displays to visualize the system activity. Once zeroed, it displays the calculated length of each axis, as well as the current X-and-Y position. In addition, the position is plotted on an XY graph resembling the carriage plane, which allows the user to visualize the carriage trajectory. The pendulum and motor positions and speeds are also graphed.

The input/output characteristics of the real-time program follow the map in Figure 6.1.1. NI VeriStand® takes sensor inputs, transforms them according to the Simulink® model, and sends output signals to the target and user interface. The inputs and outputs are routed to and from the PXI via a DAQ board, which routes the wiring pins for all system hardware.

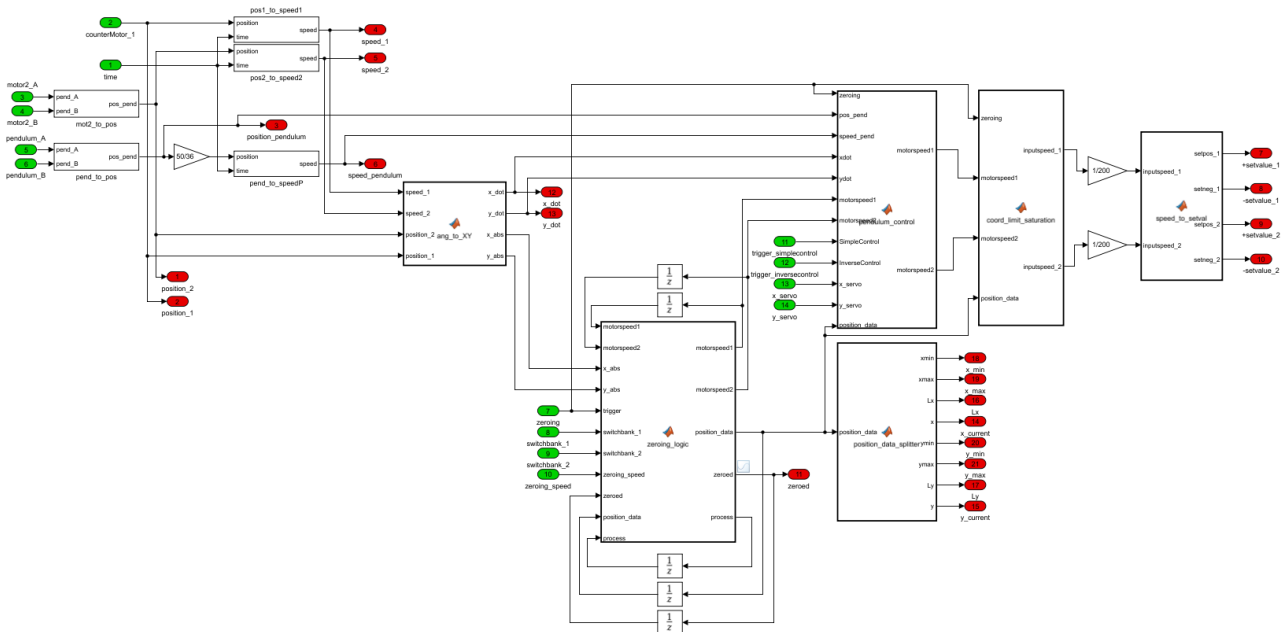


Figure 6.6.1 – Simulink® model used for real-time control.

The operations described are presented in Figure 6.6.1, which shows the current Simulink® model [11] used by VeriStand®. In layout and content it corresponds to the systems schematic laid out in Figure 6.1.1.

The inputs to the real-time model implemented in NI VeriStand® are the following:

- encoder A and B signals for both motors;
- encoder A and B signals for the pendulum;
- digital signals for two banks of limit switches (used in zeroing);
- user buttons and toggles directing control type from the GUI.

The operations which NI VeriStand® performs with these inputs are:

- calculate angular positions from given encoder A and B signals;
- estimate angular velocities from angular positions;
- calculate the states x , y , and their derivatives from motor angular position and velocities;
- perform zeroing procedure when prompted;
- store operating information like current position, limit positions, and axes lengths;
- monitor for violations of carriage in the soft limit envelope;
- calculate control actions given the states.

The outputs from NI VeriStand® after these operations are the following:

- \pm set values of voltage for both motors, to be determined by the controller;
- real-time angular position and speed data to the GUI;
- real-time carriage position in the XY plane;
- the completion of zeroing procedure to the GUI in the case it is toggled.

6.6 Conclusions

Zeroing should be carried out upon starting the pendulum test bank or after extended operation when position drift in the encoders has reduced the accuracy of the carriage position estimate of the pendulum position. Error on the pendulum angle has a clear impact on regulation of the pendulum about equilibrium, but cart drift can also be critical because the tared boundaries may cease to be valid. Zeroing also allows the carriage to locate itself as well as generating important limit and state information which other functions make use of. Carriage saturation in a soft limit envelope is a safety feature which should be constantly active in the background of control activities.

7. Conclusions

The objective of this thesis was to realise pendulum test bank for the planar pendulum and verify control of the stable and unstable planar cases, working within the framework set by previous thesis work towards a versatile didactic rig. The four projected domains of work on the system: mechanical-electrical, sensing and signal processing, model and controller development, and real-time logistics, have comprised this thesis work. The real-time framework and the first two adjustments serve the general functionality of the test bank and are applicable beyond the planar pendulum; the system is configured for two-axis actuation of the H-bridge transmission and sensing and estimating state positions and speeds with a reliable algorithm. The NI VeriStand[®] software has been proven as an operable control environment and the mappings and GUI it offers can be extended easily to new functionalities. Digital LQR control is promising as a simple control law for the MIMO system, validating the assumption that strictly planar motion cannot be assumed and XY transmission must be treated regardless. A framework now exists for parameter estimation with system identification and assimilating the motor models into the pendulum-cart plant model, applied in this case to the planar pendulum, but which could feasibly be ambiguated to a more complicated pendulum configuration.

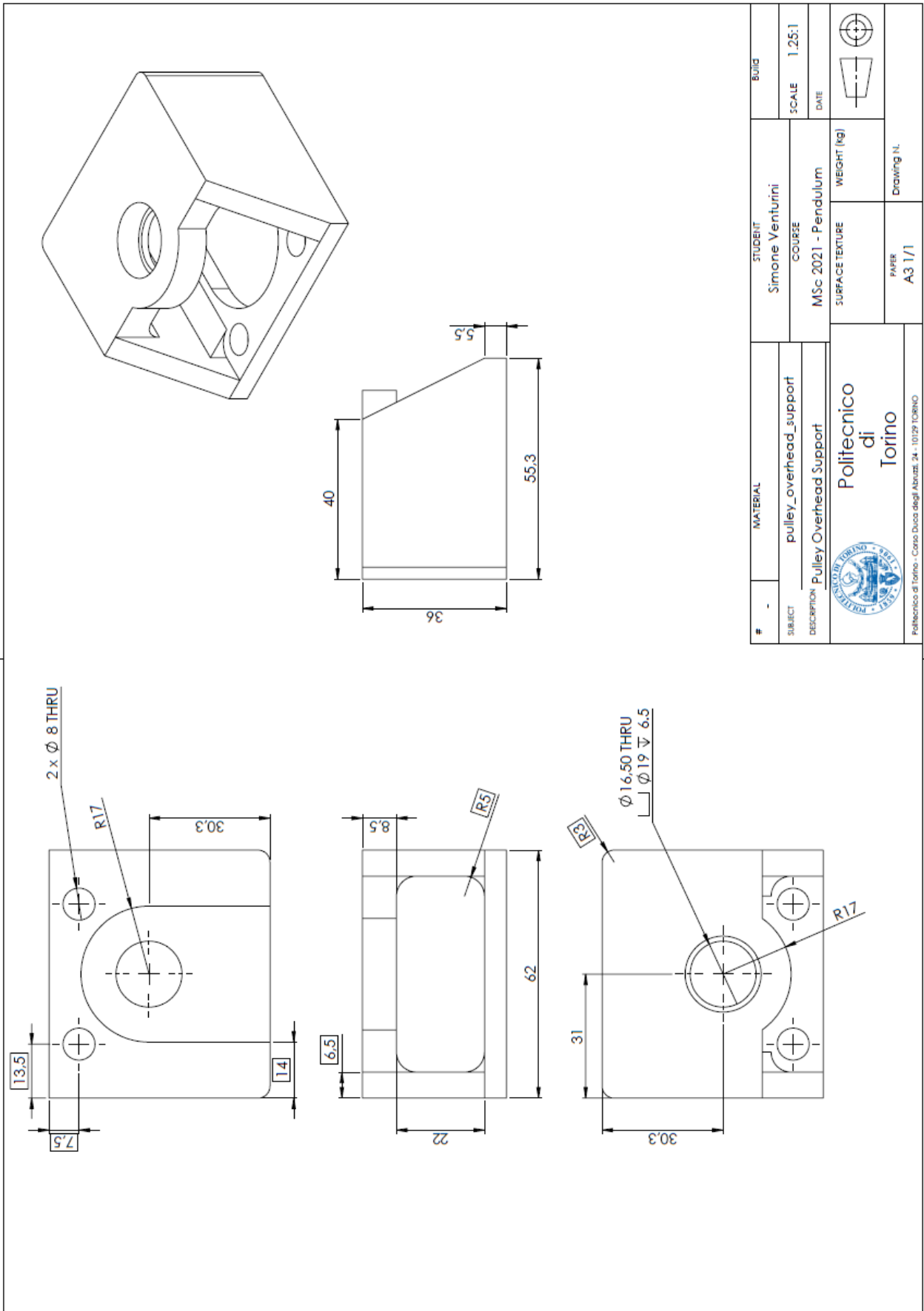
The first future modification to the system should be the substitution of the more capable power supply. The BLDC motors used in actuation are undersupplied and are capable of more powerful moment. Given that the peak motor (and therefore cart) moment is often the most crucial when stabilising or controlling a pendulum affected by an initial disturbance, the peak motor capacity is a crucial design attribute. While verified, currently the regulation of the inverted pendulum is marginally stable due to the narrow control window; with increased motor capacity this window enlarges, and it opens the possibility of simultaneous servo behaviour of the cart.

Swing-up procedures moving between stable and unstable pendulum configurations, which are inherently more demanding than either regulation [2], will require this more adequate power supply but also a further reduction of the transmission losses. In this thesis work it has been estimated that these losses may be up to 15% for X-axis translation and 50% for Y-axis translation, which is a significant limitation, especially if the system is to later be adapted to a spherical pendulum for which smooth two-axis actuation is critical.

Appendix A - Drawings

This appendix provides the assembly and part drawings for the pulley support, the electrical box, and the fabricated pendulum reported in Chapter 2.

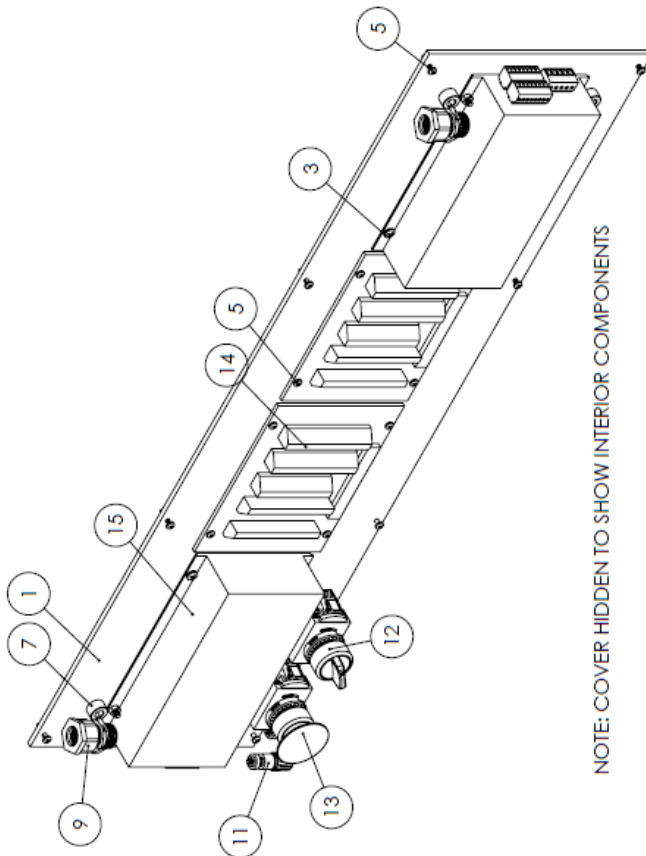
A.1 – Pulley column stabiliser



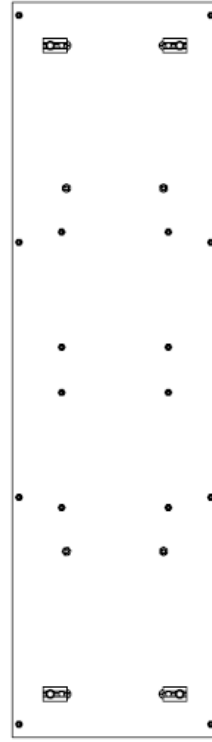
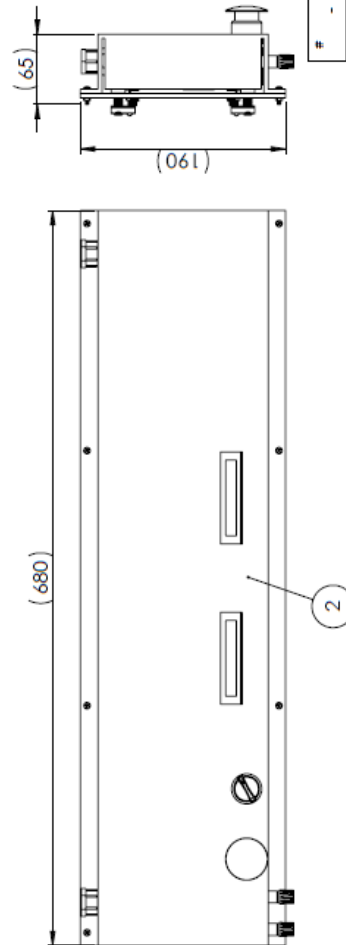
#	MATERIAL	STUDENT	BUILD
SUBJECT	pulley_overhead_support	Simone Venturini	SCALE 1,25:1
DESCRIPTION	Pulley Overhead Support	COURSE	DATE
		MSc 2021 - Pendulum	
		SURFACE TEXTURE	WEIGHT (kg)
		PAPER	Drawing N.
		A3 1/1	
 Politecnico di Torino			
Politecnico di Torino - Corso Duca degli Abruzzi, 24 - 10129 TORINO			

A.2 - Assembly-level for the electrical box

NUMBER	PART NUMBER	DESCRIPTION	QUANTITY
1	Electric_Board	Baseboard for rig electrical components	1
2	Electric_Cover	Cover for rig electrical components	1
3	92000A224	M4 x 0.7 x 14 PAN HEAD	8
4	98676A200	M4 x 0.7 HEX NUT	8
5	92000A124	M3 x 0.5 x 14 PAN HEAD	16
6	98676A100	M3 x 0.5 HEX NUT	16
7	91290A426	M8 x 1.25 x 20 SOCKET HEAD	4
8	5537T42	DROP-IN FASTENER	4
9	4880K823	Wiring Fitting Cap 1.3 thread/mm	2
10	4880K62	Wiring Fitting Connector 1.3 thread/mm	2
11	Banana_Terminal	Power/ground connector terminal	2
12	Power_Supply_Switch	Emergency/power shut-off	1
13	Power_Supply_Switch	Emergency/power shut-off	1
14	NI-CB-68LP	REFERENCE	2
15	SCA-B4-70-10-Driver	REFERENCE	2

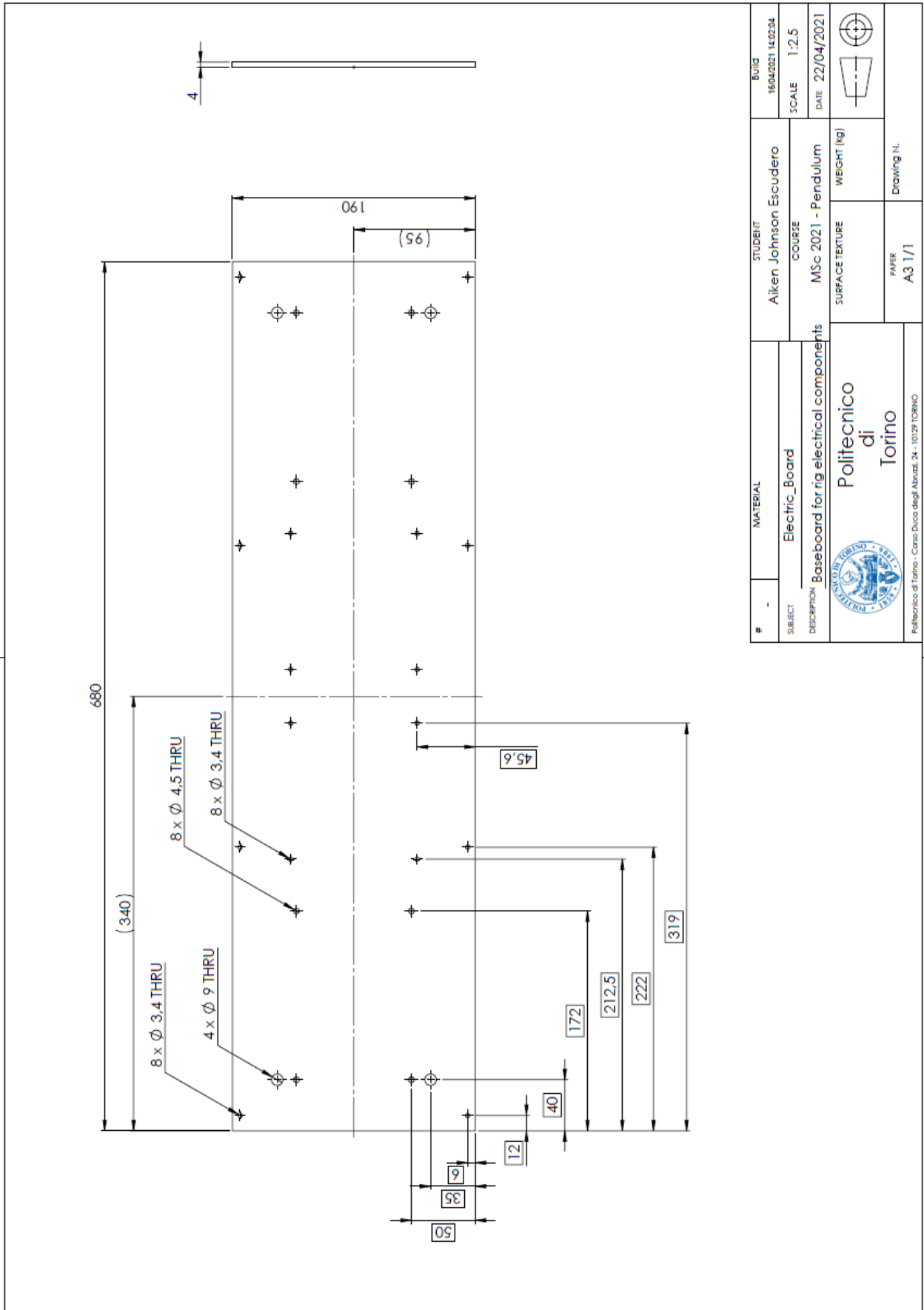


NOTE: COVER HIDDEN TO SHOW INTERIOR COMPONENTS



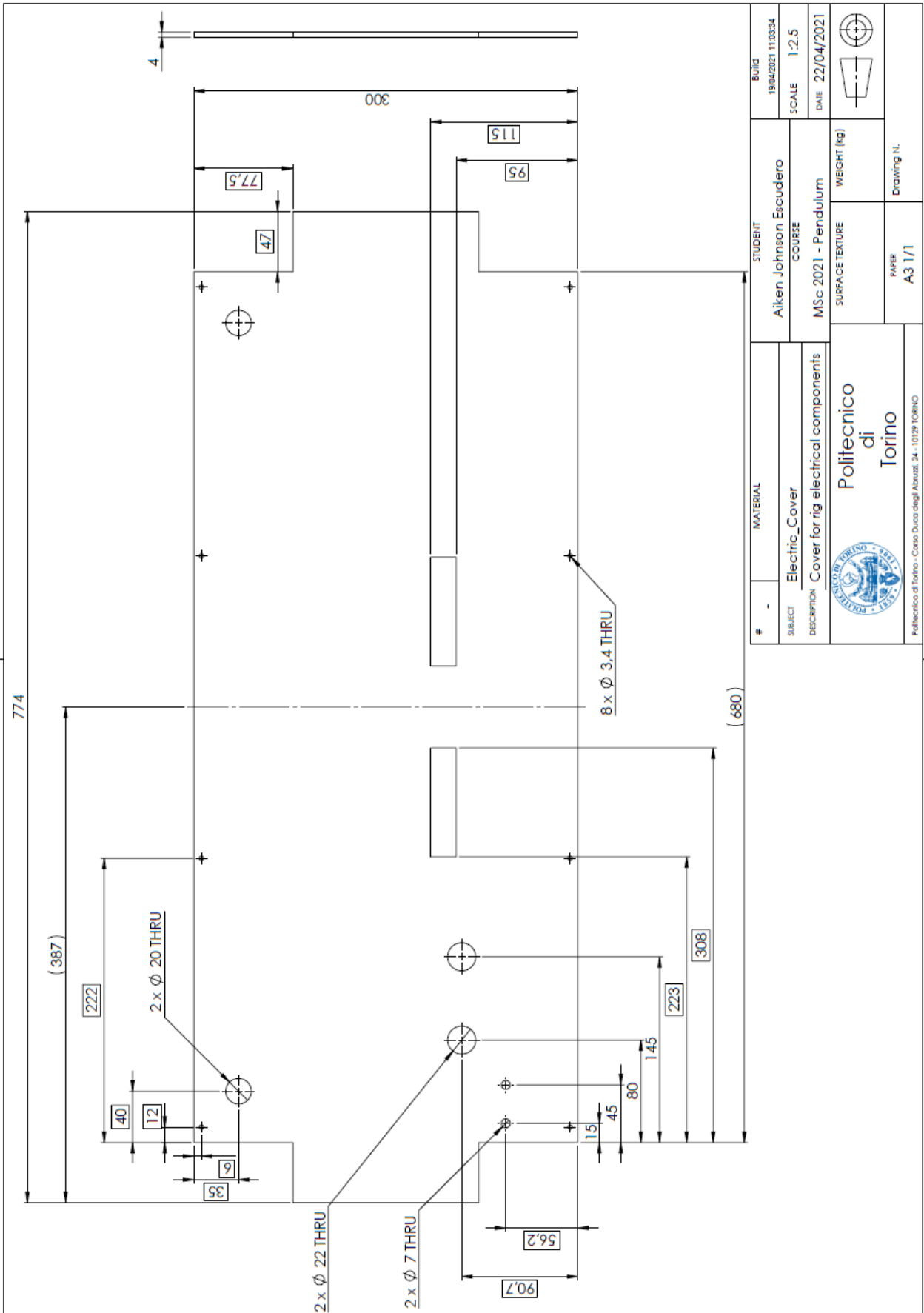
#	MATERIAL	STUDENT	20/04/2021 11:19:47
SUBJECT	Electric_Box	Aiken Johnson Escudero	SCALE 1:4
DESCRIPTION	Electrical box assembly	MSC 2021 - Pendulum	DATE 22/04/2021
 Politecnico di Torino - Corso Duca degli Abruzzi, 24 - 10129 TORINO		SURFACE TEXTURE	WEIGHT (kg)
		PAPER	Drawing N.
		A3 1/1	

A.3 - Baseboard for mounting components

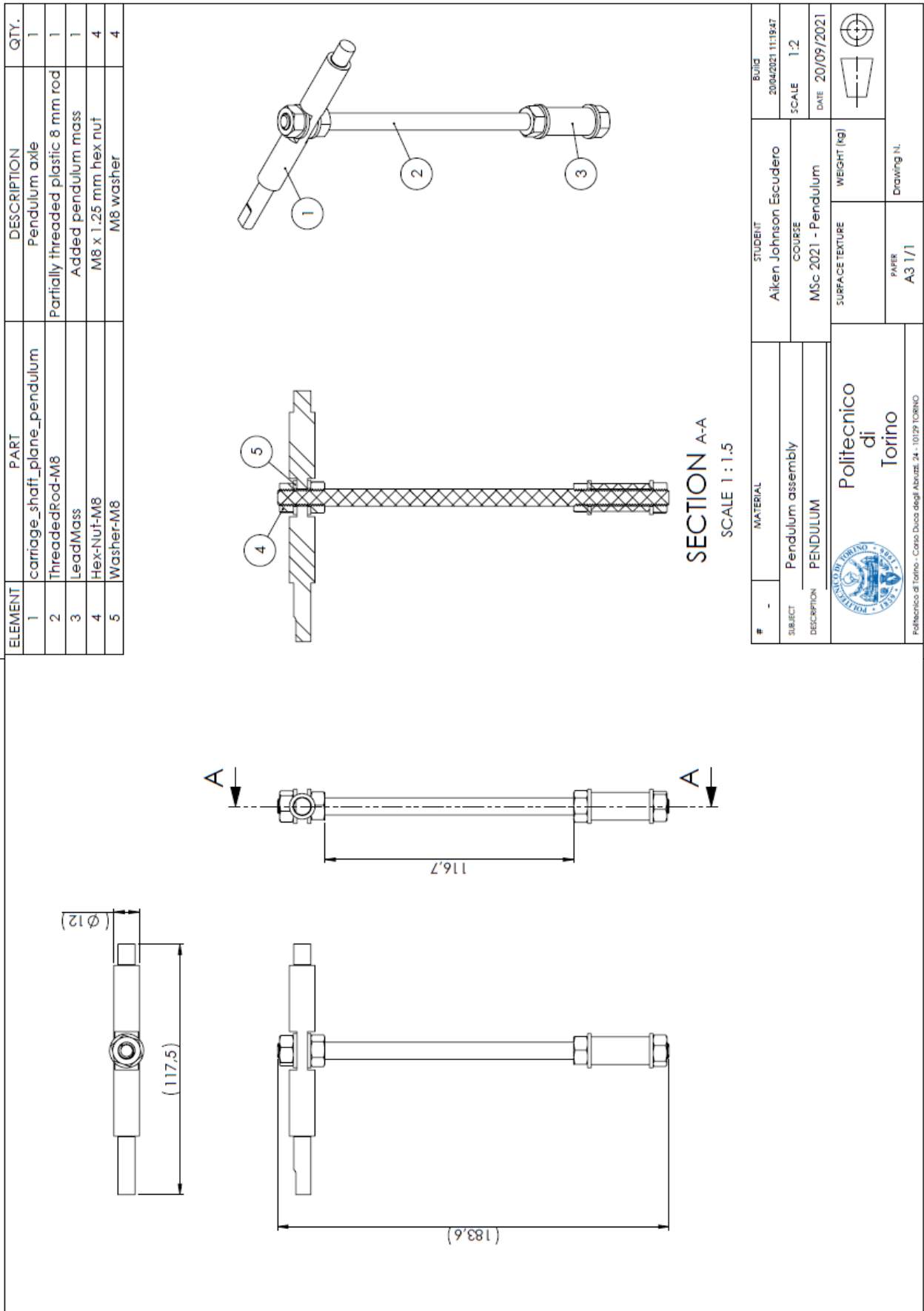


#	MATERIAL	STUDENT	BUILD
	Electric_Board	Aiken Johnson Escudero	16/04/2021 14:02:04
DESCRIPTION	Baseboard for rig electrical components	COURSE	SCALE
		MSc 2021 - Pendulum	1:2.5
		SURFACE TEXTURE	DATE
		WEIGHT (kg)	22/04/2021
 Politecnico di Torino		PAPER	
<small>Politecnico di Torino - Corso Duca degli Abruzzi, 24 - 10129 TORINO</small>		A3 1/1	Drawing N.

A.4 – Cover for electrical box

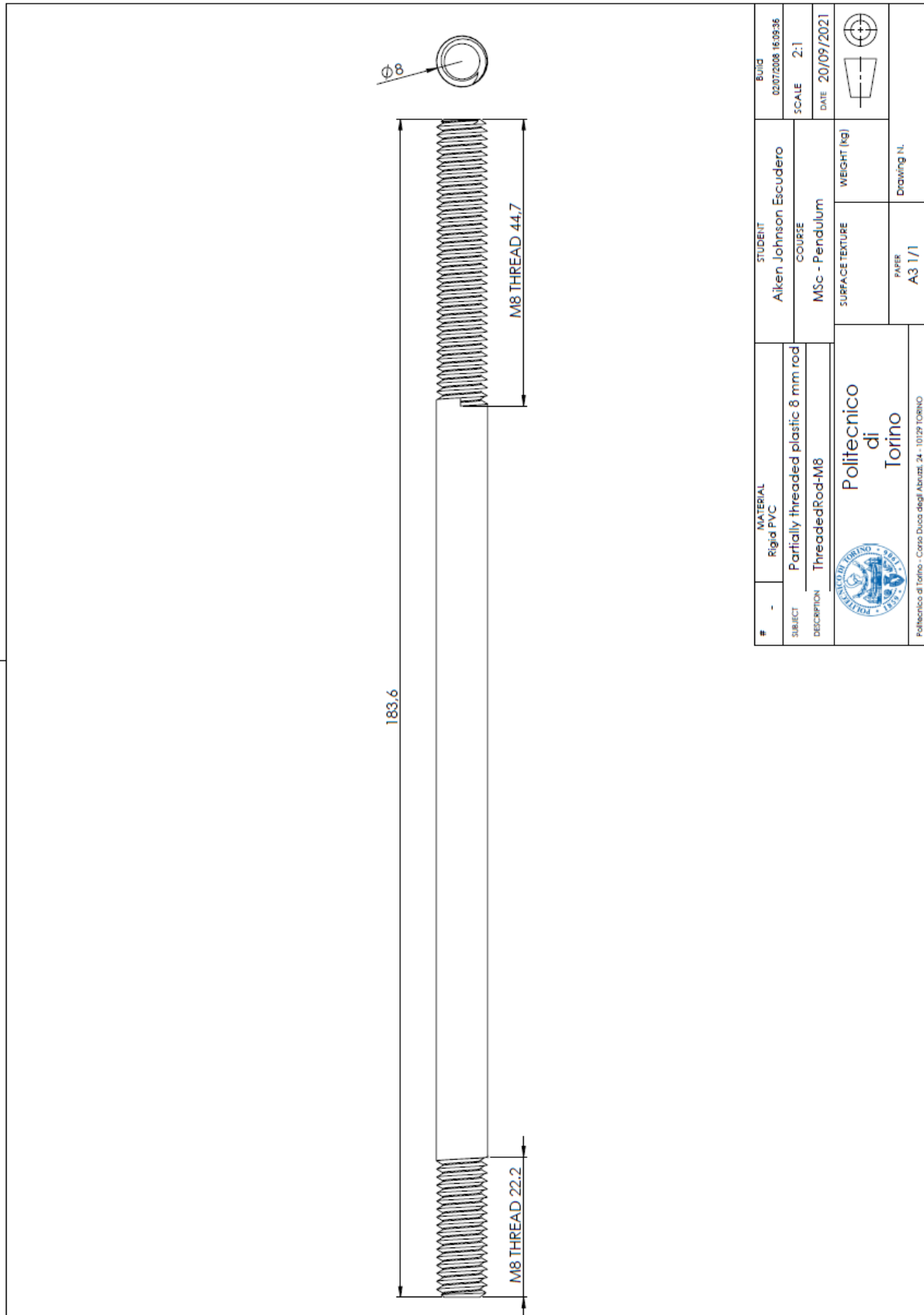


A.5 – Plane pendulum assembly drawing



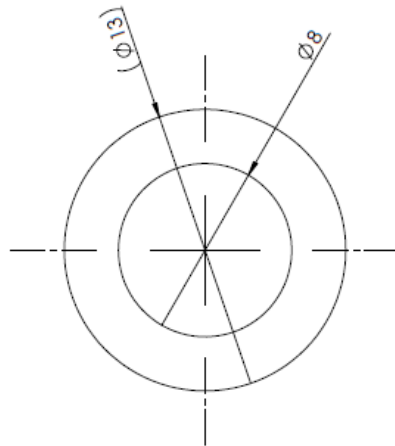
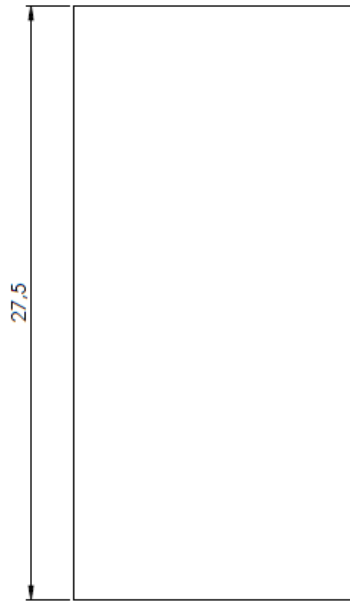
#	MATERIAL	STUDENT	BUILD
	Pendulum assembly	Aiken Johnson Escudero	2004/2021 111947
DESCRIPTION	PENDULUM	COURSE	SCALE 1:2
		MSc 2021 - Pendulum	DATE 20/09/2021
		SURFACE TEXTURE	WEIGHT (kg)
		PAPER	Drawing N.
		A3 1/1	
 Politecnico di Torino - Corso Duca degli Abruzzi, 24 - 10129 TORINO			

A.6 – Pendulum rod drawing



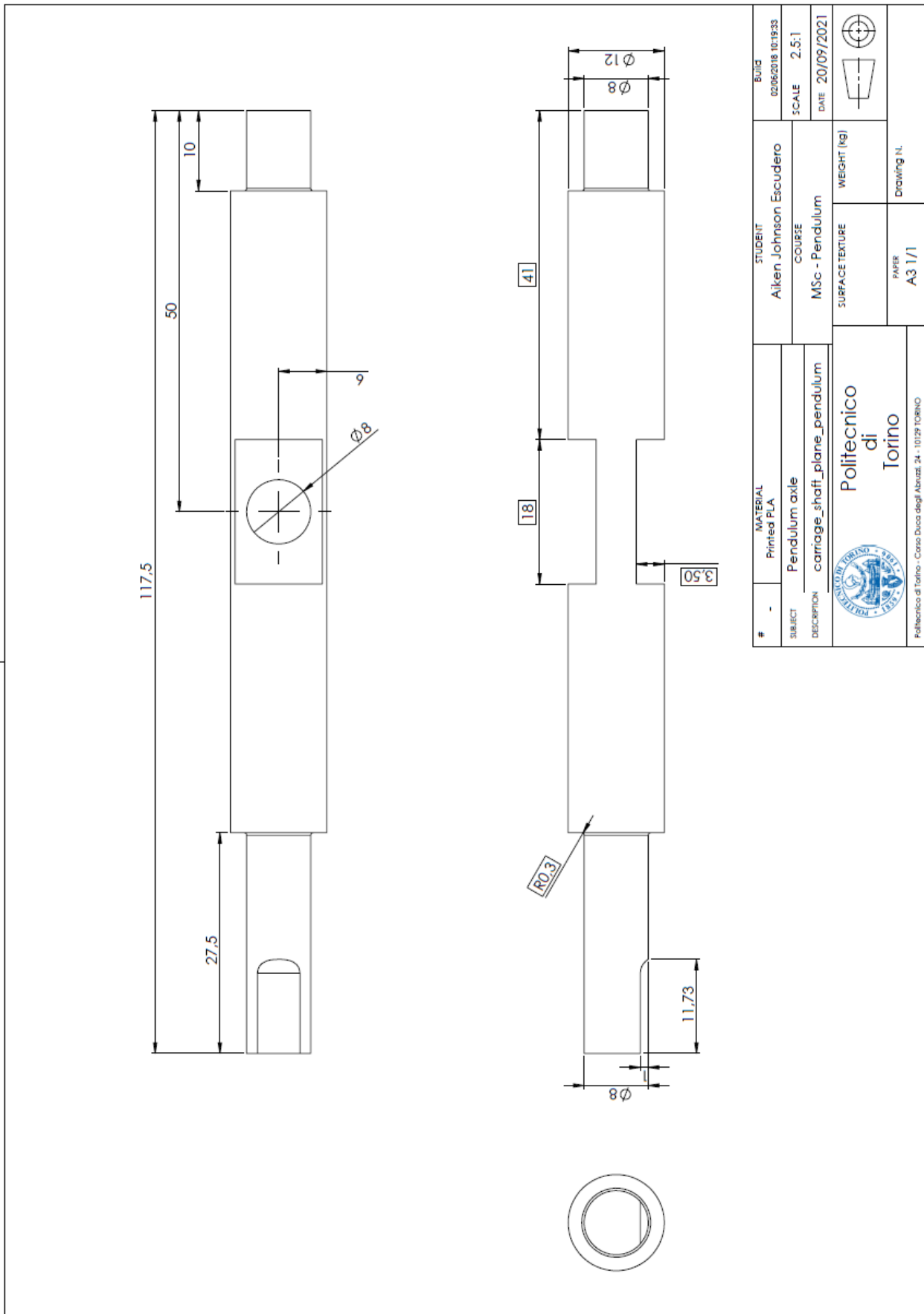
#	-	MATERIAL	Rigid PVC	STUDENT	Aiken Johnson Escudero	BUILD	02/07/2008 16:09:36
SUBJECT	Partially threaded plastic 8 mm rod	DESCRIPTION	ThreadedRod-M8	COURSE	MSc - Pendulum	SCALE	2:1
				SURFACE TEXTURE		DATE	20/09/2021
				WEIGHT (kg)			
				PAPER	A3 1/1	Drawing N.	
		Politecnico di Torino - Corso Duca degli Abruzzi, 24 - 10129 TORINO					

A.7 – Lead mass drawing



#	-	MATERIAL	STUDENT	BUIA
SUBJECT	Lead	Added pendulum mass	Aiken Johnson Escudero	19/04/2021 14:02:04
DESCRIPTION	LeadMass	LeadMass	COURSE	SCALE 5:1
			MSc 2021 - Pendulum	DATE 20/09/2021
			SURFACE TEXTURE	WEIGHT (kg)
			PAPER	Drawing N.
			A3 1/1	
 Politecnico di Torino				
Politecnico di Torino - Corso Duca degli Abruzzi, 24 - 10129 TORINO				

A.8 – Pendulum axle drawing



Reference

- [1] Barale P., *Progettazione e realizzazione di un banco prova per il controllo del pendolo piano*, MSc Thesis, Politecnico di Torino, Torino, Italy, 2019.
Barale_Progettazione e realizzazione di un banco prova per il controllo del pendolo piano_MSc2019.pdf
- [2] Venturini S., *Modelling and design of a spherical pendulum test rig*, MSc Thesis, Politecnico di Torino, Torino, Italy, 2017.
Venturini_Modelling and design of a spherical pendulum test rig_MSc2017.pdf
- [3] Incze I.I., Negrea A., Imecs M., Szabó C., *Incremental Encoder Based Position and Speed Identification: Modeling and Simulation*, Electrical and Mechanical Engineering 2(27-39), 2010.
Incze,Negrea,Imecs,Szabó_Incremental Encoder Based Position and Speed Identification Modeling and Simulation_AUS.pdf
- [4] Aguado-Rojas M., Pasillas-Lépine W., Loria A., de Bernardinis A., *Estimation Using Imperfect Incremental Encoders in Automotive Applications*, HAL, 2020.
Aguado-Rojas,Pasilla-Lepine,Loria,Bernardinis_Estimation using imperfect incremental encoders in automotive applications_HAL2020.pdf
- [5] Merry R.J.E., van de Molengraft M., Steinbuch M., *Velocity and acceleration estimation for optical incremental encoders*, Mechatronics: The Science of Intelligent Machines, 20(26), 2010.
Merry,Molengraft,Steinbuch_Velocity and acceleration estimation for optical incremental encoders_MSIM2010.pdf
- [6] Craig K., “DC Motor / Tachometer Closed-Loop Speed Control System”, 2013, pp. 1-28.
Craig_DC Motor Case Study-2013.pdf
- [7] Jiménez-González J., González-Montañez F., Jiménez-Mondragon V.M., Linceaga-Castro J.U., Escarela-Pérez R., Olivares-Galván J.C., *Parameter Identification of BLDC Motor Using Electromechanical Tests and Recursive Least-Squares Algorithm: Experimental Validation*, Actuators 10, 143, 2021.
Jiménez-González,González-Montañez,Jiménez-Mondragon,Linceaga-Castro,Escarela-Pérez,Olivares-Galvan_Parameter identification of BLDC motor_MDPI2021.pdf
- [8] Peet M.M., “System Analysis and Control: Linearization”, Arizona State University, 1-22, 2021.
Peet-System analysis and control Linearization-2021.pdf
- [9] Nayak B., Sahu S., *Parameter estimation of DC motor through whale optimization algorithm*, International Journal of Power Electronics and Drive Systems 10, 83-92, 2019.
Nayak,Sahn_Parameter estimation of DC motor through whale optimization algorithm_IJPEDS2019.pdf
- [10] Rodrigues C.R., Kuiava R., Ramos R.A., *Design of a linear quadratic regulator for nonlinear systems modeled via norm-bounded linear differential inclusions*, International Federation of Automatic Control 6, 7253-7257, 2011.
Rodrigues,Kuiava,Ramos_Design of a linear quadratic regulator for nonlinear systems modeled via norm-bounded linear differential inclusions_IFAC2011.pdf
- [11] Han G., Di Natale M., Zeng H., Liu X., Dou W., *Optimizing the Implementation of Real-Time Simulink Models onto Distributed Automotive Architectures*, Journal of Systems Architecture 59 (10), 1115-1127, 2013.
Han,diNatale,Zeng,Liu,Dou_Optimizing the Implementation of Real Time Simulink Models onto Distributed Automotive Architectures_JSA.pdf